Methods for morphological longitudinal brain modeling through atlasing and registration

Antoine Legouhy

DOCTORAT BRETAGNE LOIRE / MATHSTIC

UNIVERSITÉ DE RENNES 1

THÈSE DE DOCTORAT DE

L'UNIVERSITÉ DE RENNES 1
COMUE UNIVERSITÉ BRETAGNE LOIRE

ÉCOLE DOCTORALE N° 601
Mathématiques et Sciences et Technologies de l'Information et de la Communication
Spécialité : *Signal / Image / Vision*

Par

Antoine LEGOUHY

Methods for morphological longitudinal brain modeling through atlasing and registration

Thèse présentée et soutenue à Rennes, le 23 juin 2020
Unité de recherche : Empenn

Direction de la thèse :

Co-dir. de thèse :	Christian Barillot †	Directeur de recherche	CNRS, Empenn team
	François Rousseau	Professeur	IMT Atlantique
Encadrant :	Olivier Commowick	Chargé de recherche	INRIA, Empenn team

Rapporteurs avant soutenance :

Stanley Durrelman	Directeur de recherche	INRIA/ICM, Aramis team
Grégoire Malandain	Directeur de recherche	INRIA, Morpheme team

Composition du Jury :

Président :	Éric Marchand	Professeur	Université de Rennes 1
Examinateurs :	Olivier Commowick	Chargé de recherche	INRIA, Empenn team
	Jessica Dubois	Chargée de recherche	CEA, Neurospin / INSERM, NeuroDiderot
	Stanley Durrelman	Directeur de recherche	INRIA/ICM, Aramis team
	Grégoire Malandain	Directeur de recherche	INRIA, Morpheme team
	François Rousseau	Professeur	IMT Atlantique
	Julia Schnabel	Professor	King's College London

Methods for morphological longitudinal brain modeling through atlasing and registration

Abstract: Understanding brain development involves studying the relationship between age as one of the explanatory variables and explained variables, observations of this organ, which can take many forms. Magnetic Resonance Imaging (MRI) gives the opportunity to extract such observations in a non-invasive and non-irradiating way. This powerful technique allows notably to gain insights about the functional activity of the brain or its internal diffusivity characteristics. Yet, it is rather on the purely morphological aspects that this thesis is focused on. The approach followed the study of the brain as a mathematical object, thus enabling the analysis of its shape and growth by the means of the geometric transformations connecting those objects. In the finding of those transformations, across structures of topological interest, lies the concept of **registration**. This opens the door to the statistical analysis of shapes and the creation of average anatomical models called **atlases**.

Keywords: Atlasing, Registration, Brain development, Morphometry, MRI

Funding

The research leading to these results has been supported by the ANR MAIA project, grant ANR-15-CE23-0009 of the French National Research Agency and La Région Bretagne.

MAIA: Multiphysics image-based AnalysIs for premature brAin development understanding

Coordinator: François Rousseau

The MAIA project focuses on multiphysical imaging analysis for the study of brain development in premature babies. Long-term studies have shown that the majority of prematurely born infants may have significant motor, cognitive and behavioural deficits. This project aims to improve our knowledge on the brain development of premature babies by developing new methods for analysing brain data.

Acknowledgments

Many thanks to **Olivier Commowick** who perfectly shared his knowledge in this field. He always knew how to be available despite life's trials and tribulations. It was a great pleasure to work and hang out with him.

Many thanks also to **Christian Barillot** who was able to bring a more global vision. His long experience in the field was very valuable as well as his constant good mood.

Another big thank you to **François Rousseau** who, in spite of his more distant geographical location, was always available and able to bring very relevant knowledge.

And finally, thanks to **Empenn** (former Visages) as a whole (and the rest of the corridor) for the excellent atmosphere and spirit of cooperation shown by this team. A special thought for the Synthi quiz crew and the darts players!

Antoine Legouhy

An emotional thought for the late Christian Barillot...

Contents

Résumé en français

Comprendre le développement du cerveau implique d'étudier la relation entre l'âge comme l'une des variables explicatives et des variables expliquées, les observations de cet organe, qui peuvent prendre de nombreuses formes. L'imagerie par résonance magnétique (IRM) permet d'extraire ces observations de manière non invasive et non irradiante. Cette technique puissante permet notamment d'obtenir des informations sur l'activité fonctionnelle du cerveau ou sur ses caractéristiques de diffusivité interne. Pourtant, c'est plutôt sur les aspects purement morphologiques que porte cette thèse. L'approche suivie est celle de l'étude du cerveau en tant qu'objet mathématique, permettant ainsi l'analyse de sa forme et de sa croissance au moyen des transformations géométriques reliant ces objets. Dans la découverte de ces transformations, à travers des structures topologiquement intéressantes, repose le concept de recalage. Cela ouvre la porte à l'analyse statistique des formes et à la création de modèles anatomiques moyens appelés atlas.

Contexte

Images anatomicales IRM pour la modélisation du cerveau

Être capable de modéliser le développement du cerveau présente divers intérêts cliniques. Cela permet de mieux comprendre les mécanismes impliqués dans la maturation cérébrale. Ce peut également être un moyen de prédire l'évolution d'une maladie. De nombreux bouleversements ont lieu dans les premiers stades de la vie (en incluant la période prénatale) sur l'aspect structurel. En effet, la croissance cérébrale obéit à un changement d'échelle allométrique : l'expansion n'est pas homogène dans les différentes zones. De plus, des plis apparaissent et s'approfondissent au cours d'un processus appelé gyrification, déformant une forme quelque peu arrondie, assez lisse (le cerveau fœtal précoce) en une forme complexe et convolutée (le cerveau adulte). Parallèlement à cela, une maturation des tissus se produit via le phénomène de myélinisation donnant à la substance blanche sa couleur caractéristique et renforçant la conductivité biologique de l'information. Ces différents aspects du développement précoce du cerveau sont illustrés dans la Figure 1.

L'IRM (imagerie par résonance magnétique) offre un moyen non-invasif et non-irradiant de suivre l'évolution du cerveau. Il existe de multiples modalités IRM qui servent des objectifs différents. L'IRM de diffusion [Johansen-Berg 2013] vise à caractériser le processus de diffusion des molécules d'eau dans les tissus, donnant ainsi des indications sur l'organisation des voies neurales. L'IRM fonctionnelle [Huettel 2004], quant à elle, mesure l'activité cérébrale en utilisant l'effet BOLD (le sang dans les régions activées est plus oxygéné, ce qui entraîne une modification du signal RM). La modalité qui nous intéresse ici concerne les acquisitions anatomiques telles que les images pondérées en T1 et en T2 qui sont bien adaptées pour extraire des caractéristiques morphologiques. En effet, elles sont de bonne résolution (taille de voxel autour de $1 \times 1 \times 1$ mm) et ne sont presque pas sujettes à la distorsion spatiale. De plus, elles permettent de bien distinguer les compositions tissulaires : matière grise (MB), matière blanche (MG) et liquide céphalorachidien (LCR). Ce sont donc celles qui sont utilisées pour la segmentation et le recalage inter-sujets. Lorsqu'il est appliqué à l'échelle d'une population de sujets d'une tranche d'âge donnée, le recalage offre une pléthore de mesures morphométriques possibles (volume cérébral, surface corticale...) qui peuvent être régressées selon l'âge pour fournir des modèles de développement. On peut même créer des modèles moyens du cerveau

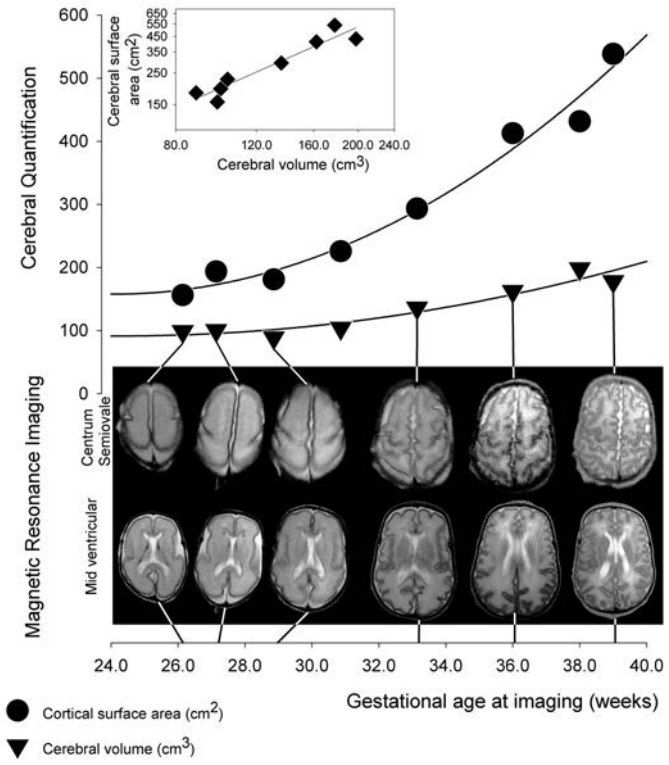

Figure 1: Images pondérées en T2, volume cerebral et aire de la surface corticale d'un sujet féminin *normal* entre 26 et 39 semaine de gestation.[a]

[a]Image issue de [Kapellou 2006] - https://doi.org/10.1371/journal.pmed.0030265.g002

en utilisant l'ensemble des informations de l'image : les atlas.

Les atlas sont utilisés de façon intensive notamment pour la normalisation spatiale [Gholipour 2007], la propagation de labels de zones segmentées [Cabezas 2011] ou pour calculer des statistiques à l'échelle d'une population [Whitcher 2007]. Ces processus sont plus efficaces lorsque les modèles moyens sont adaptés à l'âge des sujets, afin de tenir compte des spécificités liées à la maturation cérébrale mentionnées ci-dessus. Lorsqu'il est réalisé dans un contexte spatio-temporel, un atlas donne un aperçu des tendances de l'évolution du cerveau. Les bases de données d'IRM s'élargissant, incluant toujours plus de sujets et couvrant de multiples tranches d'âge, de nouveaux défis apparaissent dans la création d'atlas.

Motivations

Dans ce contexte, cette thèse est motivée par le désir de contribuer à répondre aux interrogations suivantes :

- Comment extraire des informations sur la croissance anisotrope des différentes régions du cerveau ?

De nombreuses mesures morphologiques ont été explorées pour caractériser la croissance du cerveau. La volumétrie est l'approche la plus courante, que ce soit à l'échelle du cerveau entier ou d'un point de vue plus régional. Elle donne une idée de la croissance globale, mais ne fournit aucune information sur les directions d'expansion ou la forme des régions. En revanche,

les mesures basées sur la surface sont souvent plus susceptibles de quantifier les processus de circonvolution du cerveau et l'expansion de sa surface corticale.

- Comment produire des atlas spatio-temporels qui soient non-biaisés au sein d'une population tout en étant bien représentatifs des âges qu'ils sont censés représenter ?

Les atlas spatio-temporels sont des modèles moyens du cerveau pour différents points temporels. Les différences de maturité, entre les sujets concernés, nécessitent l'utilisation d'outils robustes. Ces atlas doivent être représentatifs à la fois de la population et des points temporels considérés et ne doivent donc pas être biaisés en faveur d'un sujet donné ou décalés dans le temps.

- Comment mettre à jour les atlas existants de manière pertinente sans avoir à recommencer tout le processus à zéro ?

La création d'un atlas est un processus qui consomme beaucoup de temps car il implique une quantité élevé de recalages, de compositions de transformations... qui augmente avec le nombre d'images. Dans les méthodes de création d'atlas habituelles, tout le processus doit être recommencé à partir de zéro lorsqu'une nouvelle image arrive, ce qui est une lourde charge compte tenu de la tendance actuelle pour les bases de données massives qui s'agrandissent progressivement.

Organisation du manuscrit

Partie I: Cette partie fournit en premier lieu les bases théoriques sur les transformations géométriques qui permettent ensuite d'exposer les généralités et l'état de l'art concernant le recalage et la création d'atlas.

Le chapitre 2 présente quelques transformations géométriques couramment utilisées en anatomie computationnelle. En détail, ce chapitre inclut la façon dont celles-ci peuvent être paramétrées et décomposées en commençant par les plus basiques, les transformations affines qui opèrent globalement, aux difféomorphismes qui agissent localement tout en assurant des propriétés d'inversibilité et de différentiabilité. Le calcul de statistiques sur ces transformations tout en préservant la topologie via leur structure de groupe de Lie (à dimension infinie) est ensuite détaillé.

Cela ouvre la voie à la description du processus de recalage dans le chapitre 3. Cet outil élémentaire en traitement d'images consiste à trouver la transformation, parmi un ensemble de transformations acceptables, qui fait correspondre au mieux une image à une autre. Certaines des méthodes de recalage les plus courantes qui reposent sur l'optimisation d'une mesure de similarité entre les deux images sont décrites, qu'elles concernent la recherche de transformations linéaires ou non-linéaires.

Le chapitre 4 aborde le sujet de la création d'atlas. Un atlas consiste en un modèle moyen du cerveau, tant en termes de forme que d'intensité. Cela implique notamment des recalages et des manipulations de transformations telles que la composition et l'inversion, mais aussi des moyennages qui doivent être bien définis. Les atlas longitudinaux constituent une extension tenant également compte de la dimension temporelle, fournissant ainsi des informations sur le développement du cerveau.

Partie II: Cette partie décrit mes contributions sur le thème de l'analyse d'images pédiatriques. Cela comprend une méthode d'extraction de facteurs de changement d'échelle pour la modélisation de la croissance anisotrope du cerveau anisotrope et un travail applicatif sur les nouveau-nés impliquant l'adaptation d'outils de traitement conçus à l'origine pour les adultes.

Dans le chapitre 5, une transformation affine contrainte est introduite, offrant un moyen d'extraire des facteurs de changement d'échelle dans trois directions orthogonales via recalage. Appliqué à une base de données longitudinale, ce recalage spécial permet de modéliser, à une échelle régionale, la croissance anisotrope du cerveau.

Le chapitre 6 est consacré à l'étude de la perfusion cérébrale chez les nouveau-nés atteints d'encéphalopathie hypoxique et ischémique. Mon rôle, dans ce travail commun avec les cliniciens du CHU de Rennes, a été d'adapter et de développer de nouvelles chaîne de traitement afin de pouvoir prendre en charge de manière adaptée ce type de population très différente des populations adultes classiques.

Partie III: Cette partie est consacrée à mes contributions aux méthodes de création d'atlas, à commencer par une technique permettant d'améliorer le recalage rigide en cas de cerveaux de tailles différentes dans le chapitre 7.

Une méthode de création d'atlas spatio-temporel est ensuite détaillée dans le chapitre 8 qui tire parti d'un cadre mathématique propice pour traiter les transformations difféomorphiques. Cette méthode permet également de créer des atlas non-biaisés à une transformation rigide près, tenant compte à la fois de la croissance globale et des déformations locales. Enfin, cette méthode veille à la précision temporelle grâce à une fonction poids flexible qui module la contribution des sujets.

Une approche de création d'atlas de type centroïde itératif est ensuite présentée dans le chapitre 9, qui permet de mettre à jour un atlas au fur et à mesure que de nouvelles images arrivent sans avoir à recommencer tout le processus depuis le début. Cet aspect sera très bénéfique à l'avenir, car des bases de données de plus en plus importantes sont en cours de constitution, notamment sur plusieurs années d'acquisition.

Enfin, **Partie IV** conclut ce manuscrit en deux chapitres résumant les contributions de cette thèse (Chapitre 10) et les perspectives de ce travail (Chapitre 11).

Chapter 1

Introduction

Contents

1.1 Context

1.1.1 Anatomical MR images for brain modeling

Being able to model the brain development has various clinical interests. It allows to better understand the mechanisms involved in the cerebral maturation. It can also be a way to predict the evolution of a disease. Quite a lot is happening in the early stages of life (including the prenatal period) on the structural aspect. Indeed, the brain growth obeys an allometric scaling: the expansion is not homogeneous throughout the different areas. In addition, folds form and deepen as it undergoes a process known as gyrification distorting a somewhat smooth rounded shape (the early fetal brain) toward a complex, convoluted one (the adult brain). In parallel to that, a maturation of the tissues occurs through the myelination phenomenon giving the white matter its characteristic color and enhancing the biological conductivity of information. Those different aspects of the early brain development are exhibited in Figure 1.1.

MRI (magnetic resonance imaging) provides a non-invasive and non-irradiating way of monitoring the cerebral evolution. Multiple MR modalities exist serving different purposes. Diffusion MRI [Johansen-Berg 2013] aims at characterizing the diffusion process of water molecules in tissues, thus giving insights on the neural tracts organization. Functional MRI [Huettel 2004], on its part, measures brain activity using the BOLD effect (blood in activated regions is more oxygenated thus leading to a change of MR signal). The modality of interest here will concern anatomical acquisitions such as T1 and T2-weighted images that are well suited to extract morphological characteristics. Indeed they are of good resolution (voxel size around $1 \times 1 \times 1$ mm) and are almost not subject to spatial distortion. Also, they allow to distinguish well between tissue compositions: gray matter (GM), white matter (WM) and cerebrospinal fluid (CSF). They are therefore the ones that are used for segmentation and inter-subject registration. When gathered for a population of subjects on a given age range, registration offers plethora of possible morphometric measurements (brain volume, cortical surface area...) that can be regressed over age to provide developmental models. One can even create average models of the brain using the whole image information: atlases.

Atlases are intensively used notably for spatial normalization [Gholipour 2007], label propagation of segmented areas [Cabezas 2011] or to compute statistics on a population [Whitcher 2007]. These processes show greater efficiency when the average models are age-adapted to the subjects, in order to account for the above-mentioned brain maturation specificities. When per-

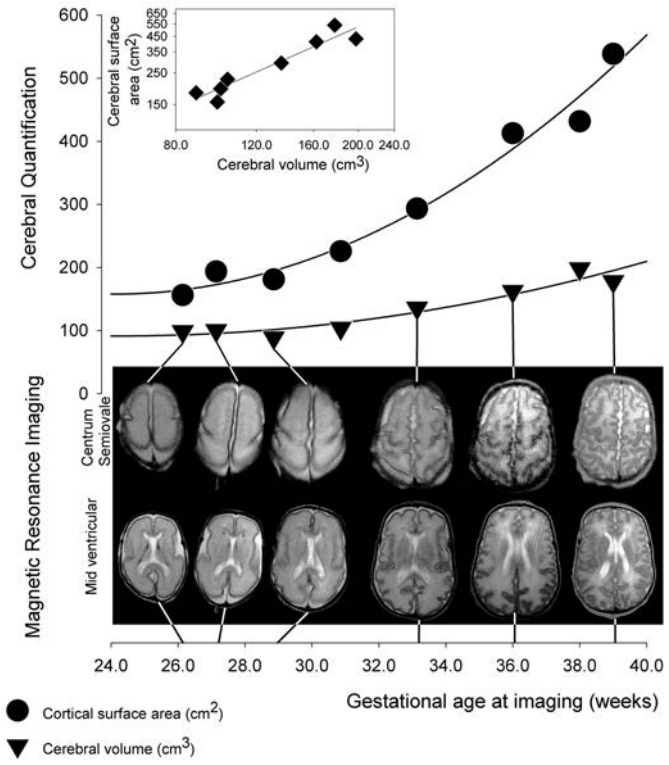

Figure 1.1: T2-weighted images, cerebral volumes and cortical surface areas of a *normal* female subject between 26 and 39 gestational weeks.[a]

[a]Image courtesy from [Kapellou 2006] - https://doi.org/10.1371/journal.pmed.0030265.g002

formed in a spatio-temporal context, an atlas gives an overview of the trends in brain evolution. As MR databases are getting larger, including subjects across a variety of age ranges, new challenges appear in atlasing.

1.1.2 Motivations

With this context in mind, this thesis is motivated by the desire to contribute in answering of the following interrogations:

- How to extract information about the anisotropic growth of the different regions of the brain ?

Many morphological measurement have been explored to characterize brain growth. Volumetry is the most common approach, either at whole brain scale or regionally. It gives an idea of the overall growth, but does not provide any information about the directions of expansion or the shape of the regions. On the other hand, surface based measurements are often more prone to quantify the folding of the brain and its cortical surface expansion.

- How to produce spatio-temporal atlases that are unbiased with respect to a population while being well-representative of the ages it is supposed to portray ?

Spatio-temporal atlases are average models of the brain for different timepoints. The maturity differences, between the subjects involved, requires the use of robust tools. Those atlases have

to be representative both of the population and the considered timepoints thus not biased toward a given subject or temporally shifted.

- How to update existing atlases in a pertinent fashion without having to restart the whole process from scratch ?

Atlas creation is a time consuming process as it involves a high number of registrations, transformation compositions... which increases with the number of images. In usual atlasing methods, the whole process has to be restarted from scratch as a new image arrives which is quite a burden considering the actual trend in massive databases that are enlarged gradually.

1.2 Organization of the manuscript

Part I: This part first provides theoretical foundations about geometric transformations that enable next to expose generalities and state-of-the-art methods for registration and atlasing.

Chapter 2 introduces some geometric transformations commonly used in computational anatomy. In details, this chapter includes the way they can be parametrized and decomposed starting with the most basic ones, affine transformations that operate globally, to diffeomorphisms that act locally while ensuring smoothness and invertibility properties. The computation of statistics on those transformations while preserving topology through their (infinite dimensional) Lie group structure is then detailed.

This paves the way for the depiction of the registration process in Chapter 3. This elementary tool of image processing consists in finding the transformation, among a set of acceptable ones, that best maps an image onto another. Some of the most common registration methods that rely on the optimization of a similarity between the two images are depicted whether they are seeking linear or non-linear transformations.

Chapter 4 addresses the topic of atlasing. An atlas consists in an average model of the brain both in terms of shape and intensity. This notably involves registrations and transformation manipulations such as composition and inversion but also averages that need to be well defined. A extension is longitudinal atlases that also account for the temporal dimension thus providing information on brain development.

Part II: This part describes my contributions on the topic of pediatric image analysis. It includes a method for scaling factors extraction for anisotropic brain growth modeling and an applicative work on newborns involving the adaptation of processing tools originally designed for adults.

In Chapter 5, a constrained affine transformation is introduced providing a way to extract scaling factors in three orthogonal directions through registration. Applied to a longitudinal database, this allows to model, at a regional scale, the anisotropic brain growth.

Chapter 6 is devoted to a study of brain perfusion on neonates suffering from hypoxic-ischemic encephalopathy. My role was, in this joint work with clinicians at the university hospital of Rennes, was to adapt and develop new processing pipelines such that they handle this kind of population that greatly differs from the classical adult populations.

Part III: This part is dedicated to my contributions in atlas creation methods, starting with a method to improve rigid registration in case of brains of different sizes in Chapter 7.

A spatio-temporal atlas creation method is then detailed in Chapter 8 that takes advantage of a convenient mathematical framework to deal with diffeomorphic transformations. Also this method creates atlases that are unbiased up to a rigid transformation both accounting for global growth and local deformations. Finally it takes care of a the temporal accuracy through a flexible weight function modulating the contribution of the subjects.

An iterative centroid atlasing approach is then presented in Chapter 9 that allows to update an atlas as new images gradually arrive without having to restart the whole process from scratch. This theme will be very beneficial in the future as larger and larger databases are being constituted, especially over several years of acquisitions.

Finally, **Part IV** concludes this manuscript over two chapters summarizing the contributions of this thesis (Chapter 10) and the perspectives of this work (Chapter 11).

Part I

Background

Chapter 2

Geometric transformations

Contents

The approach followed is this thesis is the study of brain anatomies by the prism of the transformations that matches them. Before we get into the subject of how the matching is performed, it is necessary to first recall some generalities on the geometric transformations involved.

2.1 Generalities

A **geometric transformation** is a map usually from $\mathbb{R}^2$ or $\mathbb{R}^3$ to itself that affects the spatial position of the points of those sets. It is often constrained to be bijective and can be classified according to its degrees of freedom (several to an infinite number) or the geometric properties that it preserves (distance between points, parallel lines...). This is a crucial tool for images registration, a task which consists in finding the geometric transformation, among a set of acceptable ones, that best matches two images.

We will cover in this chapter the two main classes of transformations. First, the linear and affine transformations which are of finite low dimension. They are globals in the sense that each point is transformed the same way through a single matrix operating on coordinates. We will next focus on diffeomorphisms which are capable of handling local changes without limits in terms of degrees of freedom, however with constraints on smoothness and invertibility. Finally we will show how the Lie group structures of some transformations sets can be used to compute Euclidean statistics on them.

2.2 Linear and affine transformations

We start by presenting the general linear and affine maps and their relations to geometric transformations.

2.2.1 Overview

Linear map: Let V and W be two vector spaces over a field $\mathbb{K}$. The function $f : V \to W$ is a linear map if $\forall\ u, v \in V$ and $c \in \mathbb{K}$:

$$\begin{array}{rcll} f(u+v) & = & f(u)+f(v) & \textit{additivity} \\ f(cu) & = & cf(u) & \textit{homogeneity} \end{array} \tag{2.1}$$

If V and W are finite dimensional vector spaces of dimensions n and m respectively, then every linear map from V to W can be represented by a matrix $A \in \mathbb{K}^{m\times n}$ such that $\forall x \in V$, $f(x) = Ax$.

Affine map: The function $f : V \to W$ is an affine map if it is a composition of a linear map $A \in \mathbb{K}^{m\times n}$ and a translation $t \in \mathbb{K}^n$ following: $f(x) = Ax + t$. In the context of geometric transformations, x represents a vector of coordinates: $x \in \mathbb{R}^n$ with typically $n = 2$ or 3, which is mapped into the same space so that the linear map is a square real matrix: $A \in \mathbb{R}^{n\times n}$ that operates those coordinates through matrix multiplication and the translation t is also a vector of $\mathbb{R}^n$.

This Cartesian formulation does not allow the representation of an affine transformation using only a simple matrix multiplication. However, using an homogeneous coordinates system which is a tool from projective geometry, one can overcome that burden. Those homogeneous coordinates are constructed by adding 1 as the $(n+1)^{th}$ element of the Cartesian coordinates of x while the matrix that embeds the whole affine transformation is built by concatenating the vector of translation on the right of the linear map and by adding a new line that contains only zeros except at the last column where it is a 1:

$$\begin{array}{ccc} \text{Cartesian coordinates} & \longleftrightarrow & \text{Homogeneous coordinates} \\ y = Ax + t & \longleftrightarrow & \begin{pmatrix} y \\ 1 \end{pmatrix} = \begin{pmatrix} & A & & t \\ 0 & \cdots & 0 & 1 \end{pmatrix} \begin{pmatrix} x \\ 1 \end{pmatrix} \end{array} \tag{2.2}$$

One can reformulate this as:

$$\tilde{y} = T\tilde{x} \tag{2.3}$$

where $\tilde{x}$ and $\tilde{y}$ are the homogeneous counterparts of the Cartesian coordinates x and y respectively and T encapsulates both the linear part A and the translational part t into a single matrix. This compact representation makes it computationally powerful and therefore very popular in image processing.

Affine transformations are considered as global in the sense that all the coordinates are multiplied by the same matrix.

Orthogonal group: Let R be a $n \times n$ real matrix that represents a linear map. R belongs to the orthogonal group denoted $\mathrm{O}(n)$ if:

$$RR^T = R^T R = \mathrm{Id} \tag{2.4}$$

It corresponds to the transformations that preserve distances while preserving one point fixed (the origin). Given this constraint, such matrices have $\dfrac{n(n-1)}{2}$ degrees of freedom.

Special orthogonal group: If $R \in \mathrm{O}(n)$ and $\det(R) = 1$, R also belongs to a subgroup of $\mathrm{O}(n)$ called the special orthogonal group denoted $\mathrm{SO}(n)$. In dimension 2 or 3, R is designated as a **rotation matrix** since it acts as such when applied to Cartesian coordinates. On the other hand, if $\det(R) = -1$, the matrix is considered as improper and the associated transformation contains reflections.

2.2.2 Quaternions and spatial rotations

2.2.2.1 Quaternions

Quaternions, introduced by William Rowan Hamilton in 1843 and formalized in [Hamilton 1843], are an extension of complex numbers. The set of quaternions denoted $\mathbb{H}$ is a noncommutative division algebra over real numbers, generated by the canonical basis of four elements $\{1, \mathrm{i}, \mathrm{j}, \mathrm{k}\}$ and such that the Hamilton's rule is satisfied:

$$\mathrm{i}^2 = \mathrm{j}^2 = \mathrm{k}^2 = \mathrm{i} * \mathrm{j} * \mathrm{k} = -1 \tag{2.5}$$

where $*$ is the quaternion multiplication. Any quaternion q can therefore be written:

$$q = a + b\,\mathrm{i} + c\,\mathrm{j} + d\,\mathrm{k} \tag{2.6}$$

where $a, b, c, d \in \mathbb{R}$. $\mathbb{H}$ is therefore isomorph to $\mathbb{R}^4$ leading to the representation $q = a + b\,\mathrm{i} + c\,\mathrm{j} + d\,\mathrm{k} \in \mathbb{H} \equiv q = (a \;\; b \;\; c \;\; d)^T \in \mathbb{R}^4$ which can be reformulated $(a, \;\; v)$ where a is called the scalar part and $v \in \mathbb{R}^3$ the vector part. If $a = 0$ the quaternion is considered as **pure** while it is referred as **scalar** if $v = (0 \;\; 0 \;\; 0)^T$. The following operations rule the algebra of quaternions:

- **addition:** $q_1 + q_2 = (a_1 + a_2, \;\; v_1 + v_2)$
- **internal multiplication:** $q_1 * q_2 = (a_1 a_2 - v_1 \cdot v_2, \;\; v_1 \times v_2 + a_1 v_2 + a_2 v_1)$
  where $\cdot$ and $\times$ are the dot and cross product in $\mathbb{R}^3$. ⚠ $q_1 * q_2 \neq q_2 * q_1$
- **external multiplication:** let $\lambda \in \mathbb{R}$, $\lambda q = (\lambda a, \;\; \lambda v)$
- **conjugate:** $\bar{q} = (a, \;\; -v)$
- **dot product:** $q_1 \cdot q_2 = \frac{1}{2}(\bar{q}_1 * q_2 + \bar{q}_2 * q_1) = a_1 a_2 + v_1 \cdot v_2$
- **norm:** $\|q\|^2_{\mathbb{H}} = q \cdot q = q * \bar{q} = \bar{q} * q = \|q\|^2_{\mathbb{R}^4} = a^2 + \|v\|^2_{\mathbb{R}^3}$
  If $\|q\| = 1$, it is called a **unit quaternion**.
- **inverse:** $q^{-1} = \dfrac{\bar{q}}{\|q\|^2}$ for $q \neq 0$

2.2.2.2 Matrix representations of quaternion products

There exists a representation allowing to express a quaternion product as a matrix product. We will call these 4×4 matrices L and R for respectively left and right quaternion multiplication. Let's consider $p * q$ the product of two quaternions. L_p associated to p and R_q associated to q are defined such that:

$$L_p q = R_q p = p * q \tag{2.7}$$

For any quaternion $q = \big(q_0, \;\; (q_1 \;\; q_2 \;\; q_3)^T\big)$, its associated left and right multiplication matrices L_q and R_q can be constructed following:

$$L_q = \begin{pmatrix} q_0 & -q_1 & -q_2 & -q_3 \\ q_1 & q_0 & -q_3 & q_2 \\ q_2 & q_3 & q_0 & -q_1 \\ q_3 & -q_2 & q_1 & q_0 \end{pmatrix} \quad \text{and} \quad R_q = \begin{pmatrix} q_0 & -q_1 & -q_2 & -q_3 \\ q_1 & q_0 & q_3 & -q_2 \\ q_2 & -q_3 & q_0 & q_1 \\ q_3 & q_2 & -q_1 & q_0 \end{pmatrix} \tag{2.8}$$

Those matrices also have some interesting properties such as:

- $L_{\bar{q}} = L_q^T \quad \text{and} \quad R_{\bar{q}} = R_q^T$ (2.9)
- $L_q L_q^T = L_q^T L_q = R_q R_q^T = R_q^T R_q = \|q\|^2 \,\mathrm{Id}$ (2.10)
- $L_q + L_q^T = R_q + R_q^T = 2q_0 \,\mathrm{Id}$ (2.11)
- $\det(L_q) = \det(R_q) = \|q\|^4$ (2.12)

If q is a pure quaternion: $q_0 = 0$, then (2.11) implies that L_q and R_q are skew-symmetric.
If q is a unit quaternion: $\|q\| = 1$, then (2.10) and (2.12) imply that $L_q, R_q \in \mathrm{SO}(4)$: they are rotation matrices.

2.2.2.3 Representation of rotations through unit quaternions

Any 3-dimensional vector can be rewritten as a pure quaternion: $v \in \mathbb{R}^3 \rightarrow (0, v) \in \mathbb{H}$. Thanks to Euler's theorem, the axis-angle representation allows the parametrization of any combination of spatial rotations only by a unit vector u indicating the direction of the rotation axis and an angle θ describing the magnitude of the rotation about this axis. The image v' of the vector v through this rotation can be expressed using the Rodrigues formula from [Rodrigues 1840]:

$$v' = cos(\theta)v + sin(\theta)(u \times v) + (1 - cos(\theta))(u \cdot v)u \tag{2.13}$$

Given that, lets consider the following unit quaternion:

$$q = \pm \left(\cos\left(\frac{\theta}{2}\right), \ \sin\left(\frac{\theta}{2}\right) u \right) \tag{2.14}$$

Then, v' can also be expressed by a quaternion representation of form:

$$(0, v') = q * (0, v) * q^{-1} = q * (0, v) * \bar{q} \tag{2.15}$$

Intermediate calculations are detailed in Appendix A.
Unit quaternions are widely used in computer graphics to represent spatial rotations for the following reasons:

- They are compact and more numerically stable than rotation matrices reducing round-off errors.
- They vary continuously over the unit sphere in $\mathbb{R}^4$ avoiding discontinuous jumps.
- It is easy to compose rotations through quaternion products.
- It is easy to interpolate between quaternions.

Unit quaternion to rotation matrix
Let $q = a + b\,\mathrm{i} + c\,\mathrm{j} + d\,\mathrm{k}$ be a unit quaternion i.e. $a^2 + b^2 + c^2 + d^2 = 1$ and a vector $v \in \mathbb{R}^3$ $(\rightarrow (0, v) \in \mathbb{H})$. An associated rotation matrix $A \in \mathrm{SO}(3)$ such that Av and $q * (0, v) * \bar{q}$ represent the same rotation can be constructed following:

$$q * (0, v) * \bar{q} = L_q R_{\bar{q}} (0, v) = L_q R_q^T (0, v) = \begin{pmatrix} 1 & 0 \\ 0 & A \end{pmatrix} (0, v) \tag{2.16}$$

Leading to:

$$A = \begin{pmatrix} a^2 + b^2 - c^2 - d^2 & 2bc - 2ad & 2ac + 2bd \\ 2ad + 2bc & a^2 - b^2 + c^2 - d^2 & 2cd - 2ab \\ 2bd - 2ac & 2ab + 2cd & a^2 - b^2 - c^2 + d^2 \end{pmatrix} \tag{2.17}$$

Rotation matrix to unit quaternion
Let A be a rotation matrix and a vector $v \in \mathbb{R}^3$ $(\rightarrow (0, v) \in \mathbb{H})$. An associated unit quaternion

$q = a + b\,\mathrm{i} + c\,\mathrm{j} + d\,\mathrm{k}$ such that $q * (0, v) * \bar{q}$ and Av represent the same rotation can be constructed following:

$$\begin{cases} \text{if } \mathrm{Tr}(A) \neq -1 & & \text{if } \mathrm{Tr}(A) = -1 \\ a = \frac{1}{2}\sqrt{1 + \mathrm{Tr}(A)} & & a = 0 \\ b = \frac{1}{4a}(A_{32} - A_{23}) & & b = \sqrt{-\frac{1}{2}(A_{22} + A_{33})} \\ c = \frac{1}{4a}(A_{13} - A_{31}) & & c = \sqrt{-\frac{1}{2}(A_{11} + A_{33})} \\ d = \frac{1}{4a}(A_{21} - A_{12}) & & d = \sqrt{-\frac{1}{2}(A_{11} + A_{22})} \end{cases} \tag{2.18}$$

Another obvious possibility is the quaternion $-q$.

2.2.3 Matrix decomposition

The linear part of an affine transformation is a matrix that can be decomposed into more elementary elements such as rotations and scalings.

2.2.3.1 Using singular value decomposition

Let T be an affine transformation matrix with linear part A and translational part t. Using singular value decomposition (SVD) on A, we obtain:

$$A = VDW^T \tag{2.19}$$

Where W and V are orthogonal matrices and D is a positive diagonal matrix. In this configuration, V and W are not guaranteed to be proper i.e. $\det(V)$ and/or $\det(W)$ may be equal to -1, therefore containing reflexions. Yet, we would like them to be rotation matrices to take advantage of the quaternion formulation. To this end, one can consider another akin decomposition by multiplying the first columns of V, W and D by their determinants:

- $P = V \begin{pmatrix} \det(V) & 0 \\ 0 & I_{n-1} \end{pmatrix}$ $\longrightarrow$ P is a rotation matrix
- $U = W \begin{pmatrix} \det(W) & 0 \\ 0 & I_{n-1} \end{pmatrix}$ $\longrightarrow$ U is a rotation matrix defining the directions of scaling
- $S = D \begin{pmatrix} \det(V).\det(W) & 0 \\ 0 & I_{n-1} \end{pmatrix}$ $\longrightarrow$ S is a diagonal scaling matrix

leading to what we will refer as the rotations and scaling decomposition (RSD):

$$A = PSU^T \tag{2.20}$$

Unlike in the SVD case, it is the diagonal matrix that bears the responsibility of possible reflections while the left and right matrices are guaranteed to be proper. Given that, the rotation induced by the matrices P and U can be represented using unit quaternions.

2.2.3.2 Using polar decomposition

Let T be an affine transformation matrix with linear part A and translational part t. Using polar decomposition (PD) on A, we obtain:

$$A = QH \tag{2.21}$$

where Q is an orthogonal matrix and H is a positive-semidefinite symmetric matrix. One can easily retrieve PD from SVD. Let $A = VDW^T$ through SVD, we can reformulate the expression

to get Q and H:

$$\begin{aligned} A &= VDW^T \\ &= \underbrace{VW^T}_{Q}\underbrace{WDW^T}_{H} \end{aligned} \tag{2.22}$$

2.2.4 Subsets of affine transformations

By imposing additional constraints, one can define subsets of affine transformations:

- A **rigid transformation** preserves Euclidean distance between any pair of points leading to a transformed object that has the same shape and size as the original one. This type of transformation is only composed of a rotation R i.e. putting S to identity in Equation 2.20: $R = PU^T$ and a translation.
- A **similarity** is a transformation that preserves the shape of an object but scales it uniformly. This is done by imposing the scaling matrix in Equation 2.20 to be composed of equal elements in the diagonal: $S = s\,\mathrm{Id}$ where $s \in \mathbb{R}$. This type of transformation is composed of a rotation $R = PU^T$, an isotropic scaling s and a translation leading to a linear part of form: $A = sR$.
- An **affine transformation** preserves points, lines and planes while ensuring parallel lines to remain that way. It is composed of a non-constrained linear part $A = PSU^T$ and a translation.

A summary of those subsets of affine transformations together with their respective degrees of freedom in 3 dimensions is available in Table 2.1. An overview of those transformations applied to a 2D grid is shown in Figure 2.1

Transformation	Degrees of freedom	
Rigid	6	▷ a rotation (3 dof): $R = PU^T$ ▷ a translation (3 dof): t
Similarity	7	▷ a rotation (3 dof): $R = PU^T$ ▷ an isotropic scaling (1 dof): s ▷ a translation (3 dof): t
Affine	12	▷ a rotation (3 dof) that settles scaling directions: U ▷ an anisotropic scaling (3 dof): S ▷ a rotation (3 dof): P ▷ a translation (3 dof): t

Table 2.1: Subsets of affine transformations and their respective degrees of freedom

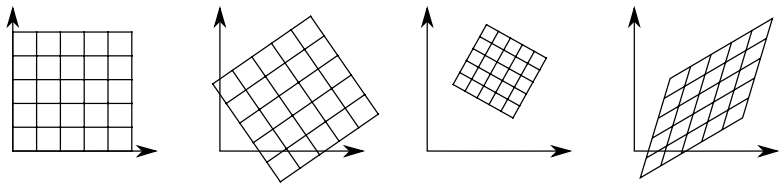

identity rigid similarity affine

Figure 2.1: Linear transformations applied to a 2D regular grid.

2.3 Diffeomorphisms

The global aspect of the above-mentioned transformations forbids the characterization of local changes between two objects. We will describe in this section a transformation of infinite dimension with interesting topology-preservation properties.

2.3.1 Presentation

Let M and N be two differentiable manifolds. A map $f : M \to N$ is a **diffeomorphism** if:

- f is bijective.
- f is differentiable
- f^{-1} is differentiable.

It is a smooth one-to-one mapping which preserves topology thus not generating foldings or holes. A diffeomorphism is characterized at each point by a non-zero determinant of the jacobian matrix.

Let M be a differentiable manifold, we denote by $\mathrm{Diff}(M)$ the set of all diffeomorphisms of M onto itself. The set $\mathrm{Diff}(M)$ together with the composition law $\circ$: $(\mathrm{Diff}(M), \circ)$ is given a group structure of infinite dimension.

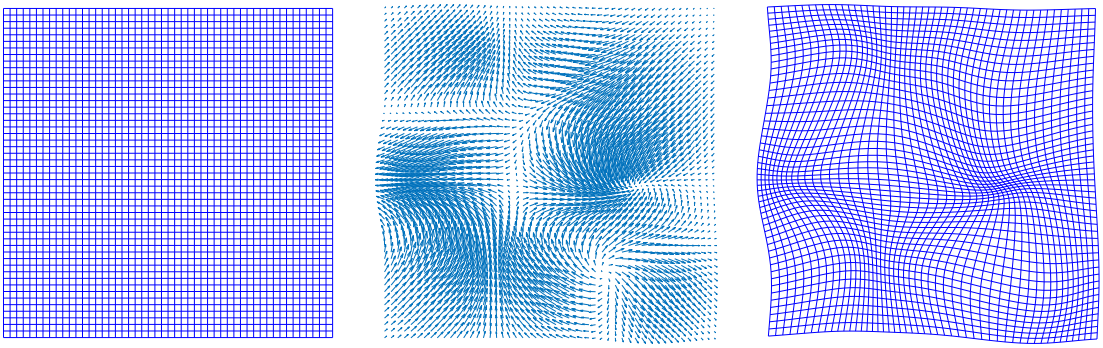

Figure 2.2: Regular grid before (left) and after (right) diffeomorphic transformation together with the associated deformation field (center).

In this work, we focus a lot on these transformations and their processing. We present in the remaining part of this section two usual parameterizations of diffeomorphisms: LDDMM and SVF.

2.3.2 LDDMM parametrization

Following the **Large Deformation Diffeomorphic Metric Mapping** (LDDMM) framework, formalized in [Christensen 1996] and taken up notably in [Beg 2005], a diffeomorphism $\phi \in \mathrm{Diff}(M)$ (with M being typically $\mathbb{R}^2$ or $\mathbb{R}^3$ in our case) can be parametrized by a **time-varying velocity field** $v(t)$. In this context, diffeomorphisms are seen as the flow of vector fields $\gamma(t)$ initiated at the identity given by the following ordinary differential equation (ODE):

$$\frac{\partial \gamma(x,t)}{\partial t} = v(t, \gamma(x,t)) \ , \text{ with initial condition: } \gamma(x,0) = x \tag{2.23}$$

The applied transformation ϕ is then generated through the integration of this ODE during one unit of time:

$$\phi(x) \triangleq \gamma(x,1) = x + \int_0^1 v(t, \gamma(t))dt \tag{2.24}$$

It has been proved in [Dupuis 1998] that if the field v is smooth enough, the associated ϕ is indeed a diffeomorphism.

2.3.3 SVF parametrization

In a more restricted parametrization, diffeomorphisms are obtained through the integration of stationary ordinary differential equations (ODEs), i.e the ones whose velocity vector field do not depend on time [Arsigny 2006a]:

$$\frac{\partial \gamma(x,t)}{\partial t} = v(\gamma(x,t)) \ , \text{ with initial condition: } \gamma(x,0) = x \tag{2.25}$$

Here v is called a **stationary velocity field** (SVF). This stationary aspect of the velocity field is the key difference with the above mentioned LDDMM framework. Contrary to the latter, this approach using SVF does not allow the parametrization of the whole group of diffeomorphisms $\mathrm{Diff}(M)$ (see [Grabowski 1988]). Despite this fact (and some other Riemannian aspects), we will see in the following its convenience notably for calculation through its infinite-dimensional Lie group structure.

2.4 On computing statistics on transformations

Whether transformations take the form of a matrix or a deformation field, the natural operation i.e. the one that preserves topology, is the composition. On the other hand, since they generally do not form a vector space, the addition often appear geometrically meaningless. Indeed the addition and therefore the Euclidean average of multiple transformations of a given type with given properties is not ensured to keep those attributes.

This is quite critical for atlas creation that we will review in Chapter 4. Since an atlas corresponds to an average model both in terms of shape and intensity, it is not surprising that some averages of images and transformations between individuals will be required in the creation process. This burden is shared with interpolation where e.g. one wants to compute a transformation at a given point by interpolating through averages from known transformations at control points. Also, in registration which is commonly an iterative process, one generally cannot simply update a transformation by adding a new displacement.

The need is therefore felt for a theoretical framework allowing to compute statistics on those transformations while preserving nice properties such as smoothness and invertibility.

The goal of this chapter is to expose some fundamentals and properties about Lie groups and show how this structure will allow us to compute statistics on geometric transformations. A main source of inspiration comes from [Bossa 2007, Vercauteren 2008, Arsigny 2006a] and the recently published [Pennec 2020].

2.4.1 Theoretical background on Lie groups

We will introduce the notion of Lie group and overview some of its properties, especially the relations with its tangent space at identity through logarithm and exponential maps.

2.4.1.1 Basics

Group: Let G be a set and $\cdot$ a binary operation on G (group law), namely that applies on two elements to form a new element. Together they form a group denoted $(G, \cdot)$ if the following four group axioms are satisfied:

- Closure: $\forall a, b \in G,\ a \cdot b \in G$
- Associativity: $\forall a, b, c \in G,\ (a \cdot b) \cdot c = a \cdot (b \cdot c)$

- Identity element: $\exists e \in G$ called the identity element such that $\forall a \in G$, $e \cdot a = a \cdot e = a$
- Inverse: $\forall a \in G\ \exists a^{-1}$ called the inverse of a such that $a \cdot a^{-1} = a^{-1} \cdot a = e$ where e is the identity element.

Lie group: Let $(G, \cdot)$ be a group. G is a Lie group if:

- G is a finite-dimensional smooth manifold.
- $f\colon G \times G \to G$ is smooth. $(a, b) \mapsto a \cdot b$
- $g\colon G \to G$ is smooth. $a \mapsto a^{-1}$

Lie algebra: A Lie algebra denoted $\mathfrak{g}$ is a vector space over a field $\mathbb{K}$ together with a binary operation $[\cdot, \cdot] : \mathfrak{g} \times \mathfrak{g} \to \mathfrak{g}$ called the **Lie bracket** satisfying the following axioms: $\forall a, b \in \mathbb{K}$, $x, y, z \in \mathfrak{g}$

- Bilinearity: $[ax + by, z] = a[x, z] + b[y, z]$ and $[z, ax + by] = a[z, x] + b[z, y]$
- Alternativity: $[x, x] = 0$
- Jacobi identity: $[x, [y, z]] + [z, [x, y]] + [y, [z, x]] = 0$

To every Lie group G can be associated a Lie algebra $\mathfrak{g}$ of the same dimension, whose underlying vector space is the tangent space of G at the identity element. The Lie algebra completely captures the local structure of its associated Lie group. This correspondence is not one-to-one as a given Lie algebra can be associated to several Lie groups.

One-parameter subgroup: Let $(G, \cdot)$ be a group with identity element e. A family of element $\{\gamma(s) \mid \gamma : \mathbb{R} \to G\}_{s \in \mathbb{R}}$ is a one-parameter subgroup of G if and only if: $\forall s, t \in \mathbb{R}$:

- $\gamma(0) = e$
- $\gamma(s) \cdot \gamma(t) = \gamma(s + t)$

The one-parameter subgroup forms a path over its associated Lie group, starting at the identity. If γ if differentiable, its derivative at 0: $X_\gamma = \left.\dfrac{\mathrm{d}\gamma(s)}{\mathrm{d}s}\right|_{s=0}$ is called the **infinitesimal generator** of the one-parameter subgroup. An illustration is shown in Figure 2.3.

Exponential map: Let G be a Lie group and $\mathfrak{g}$ be its associated Lie algebra. One can define the exponential map exp as:

$$\begin{aligned} \exp\colon \mathfrak{g} &\to G \\ X &\mapsto \gamma(1) \end{aligned} \tag{2.26}$$

Where γ is the unique one-parameter subgroup of G whose tangent vector at the identity is equal to X, X being therefore the infinitesimal generator of γ.
Now, the exponential map is a diffeomorphism from an open neighborhood of 0 in $\mathfrak{g}$ to an open neighborhood of Id in G. One can therefore define an inverse map called the **logarithm map** log from an open neighborhood of Id in G such that for every g in this neighborhood, there exists a unique x in the open neighborhood of 0 in $\mathfrak{g}$ such that $g = \exp(x)$ and thus $x = \log(g)$.

It is therefore possible to, locally around the identity, *unfold* a Lie group through the logarithm map onto its Lie algebra which is a vector space where it is easy to work with since linear algebra applies. After working on the Lie algebra, one can use the exponential map to *fold* it back onto its original structure.

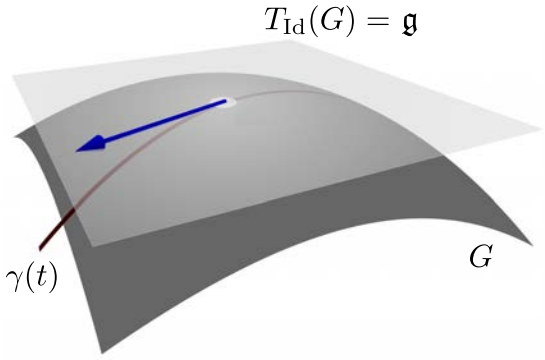

Figure 2.3: A Lie groupe: G, its tangent space at identity (associated Lie algebra): $\mathfrak{g}$, and a one-parameter subgroup on G: γ.

2.4.1.2 Baker-Campbell-Hausdorff formula

Since Lie algebras are vector spaces, the natural operations are additions and multiplications by a scalar while it is the internal composition law that prevails in the associated Lie group. One might want to compute what would be the representation in the Lie algebra of the composition of two elements of the Lie group without any logarithm computation. This is especially desirable since the logarithm is not always well-defined and can be computationally expensive. The Baker-Campbell-Hausdorff (BCH) formula allows an estimation of the logarithm of the composition of two elements of the Lie group only using corresponding elements of Lie algebra through a series of Lie bracket terms.

Baker-Campbell-Hausdorff formula: Let $v, w \in \mathfrak{g}$ close enough to 0. Then the following series converges:

$$\log(\exp(v) \cdot \exp(w)) \approx v + w + \frac{1}{2}[v, w] + \frac{1}{12}([v, [v, w]] + [[v, w], w]) + \dots \tag{2.27}$$

2.4.1.3 Fast computation of exponential and logarithm

Those techniques are not well suited for all couple of Lie algebras and groups but they will show themselves very efficient in our context of interest which is geometric transformations [Arsigny 2006b, Arsigny 2006a].

Scaling and squaring for exponential

The scaling and squaring method allows the fast computation of $\phi \in G$, the exponential of $v \in \mathfrak{g}$. The idea is to benefit from the fact that the exponential can often be easily approximated near the origin and that $\exp(v) = \exp\left(2^{-k}v\right)^{2^k}$.

1. Scaling: Choose k such that $2^{-k}v$ is small enough.
2. Approximation: $\exp\left(2^{-k}v\right) \underset{0}{\approx} \mathrm{Id} + 2^{-k}v$ (Padé approximant of order $[1, 0]$)
3. Squaring: let $\alpha_0 = \mathrm{Id} + 2^{-k}v$. k recursive squarings: $\underbrace{\alpha_i = \alpha_{i-1} \circ \alpha_{i-1}}_{\text{for } i=1 \text{ to } k}$

   leading to $\exp(v) \approx \alpha_k$

Inverse scaling and squaring for logarithm

The inverse scaling and squaring method allows the fast computation of $v \in \mathfrak{g}$ the logarithm of $\phi \in G$. The idea is to benefit from the fact that the logarithm can be easily approximated near the identity and that $\log(\phi) = 2^k \log\left(\phi^{2^{-k}}\right)$.

1. Scaling: Choose k big enough.
2. Rooting: Compute $\phi^{2^{-k}}$ through k recursive square rootings.
3. Approximation: $\log\left(\phi^{2^{-k}}\right) \underset{\text{Id}}{\approx} \phi^{2^{-k}} - \text{Id}$, leading to: $\log(\phi) \approx 2^k \log\left(\phi^{2^{-k}}\right)$

It should be noted that the rooting process is not straightforward and can therefore show itself computationally expensive.

2.4.2 Lie group structure of linear transformations

As previously explained, a linear transformation T can be written as a $(n+1) \times (n+1)$ matrix of form:

$$T = \begin{pmatrix} & A & & t \\ 0 & \cdots & 0 & 1 \end{pmatrix} \tag{2.28}$$

Where A is the linear part and t the translational part of T. A defines the type of transformation: if $A \in GL_n(\mathbb{R})$, the transformation is affine; if $A \in SO(n)$, the transformation is rigid.

The group of $n \times n$ invertible matrices over the field of real numbers: $GL_n(\mathbb{R})$ together with the matrix multiplication forms a Lie group of dimension n^2.

The Lie algebra of $GL_n(\mathbb{R})$, denoted $\mathfrak{gl}_n$, consists of all $n \times n$ real matrices i.e. the whole $\mathcal{M}_n(\mathbb{R})$.

The group of $n \times n$ orthogonal matrices (orthogonal group): $O(n)$ and the group of $n \times n$ rotation matrices: $SO(n)$ are both Lie groups of dimension $\frac{n(n-1)}{2}$.

$O(n)$ and $SO(n)$ share the same Lie algebra, denoted $\mathfrak{o}_n$ that consists of all $n \times n$ real skew-symmetric matrices.

In all those cases, the group law is the matrix multiplication, the identity element is the identity matrix of dimension n and the Lie bracket associated to those Lie algebra is the commutator: $[X, Y] = XY - YX$. A recap is provided in Table 2.2.

Lie group		Lie algebra	
$GL_n(\mathbb{R})$	$\{A \in \mathcal{M}_n(\mathbb{R}) \mid \det(A) \neq 0\}$	$\mathcal{M}_n(\mathbb{R})$	all $n \times n$ matrices
$O(n)$	$\{A \in \mathcal{M}_n(\mathbb{R}) \mid AA^T = A^TA = \text{Id}\}$	$\mathfrak{o}_n$	$\{X \in \mathcal{M}_n(\mathbb{R}) \mid X^T = -X\}$
$SO(n)$	$\{A \in O(n) \mid \det(A) = 1\}$	$\mathfrak{o}_n$	$\{X \in \mathcal{M}_n(\mathbb{R}) \mid X^T = -X\}$

Table 2.2: Some common Lie groups of matrices and their respective Lie algebras

Let the matrix $X \in \mathcal{M}_n(\mathbb{R})$, the exponential map $A \in GL_n(\mathbb{R})$ is well-known and can be constructed following:

$$A = \exp(X) = \sum_{k=0}^{+\infty} \frac{1}{k!} X^k \tag{2.29}$$

Where X^0 is defined to be the identity matrix. This series converges for any X and can be computed quickly using Jordan-Chevalley decomposition or using the scaling and squaring method depicted previously.

In the special case of X being in the Lie algebra of spatial rotation matrices: $X \in \mathfrak{o}(3)$, an analytic expression derived from the Rodrigues formula exists for the associated exponential $R \in SO(3)$ [Davis 2010]:

$$R = \exp(X) = \begin{cases} \text{Id} & \text{, if } \theta = 0 \\ \text{Id} + \dfrac{\sin\theta}{\theta} X + \dfrac{1 - \cos\theta}{\theta^2} X^2 & \text{, if } \theta \neq 0 \text{ and } \theta \neq k\pi, k \in \mathbb{Z} \end{cases} \tag{2.30}$$

Where $\theta = \sqrt{\frac{1}{2}\operatorname{Tr}(X^T X)}$.

The formalization of the matrix logarithm is not as straightforward as the exponential. Because the exponential map is not one-to-one, a real matrix may not have any logarithm. The conditions for existence and uniqueness of logarithm for real and complex matrices are investigated in [Higham 2008, Gallier 2008, Arsigny 2009]. What matter for us here is the following: Let $A \in GL_n(\mathbb{R})$. If A has no negative eigenvalues, then A has a unique real logarithm $\log(A)$ whose imaginary parts of eigenvalues $\operatorname{Im}(\lambda)$ are such that: $-\pi < \operatorname{Im}(\lambda) < \pi$.

This logarithm is usually referred as the principal logarithm. Even though this constraint on eigenvalues does not have a straightforward translation in terms of transformation constraints, it appears that, in the absence of reflexions, only very large (thus non-realistic in practice) transformations would go beyond the frame. It can be notably computed using the inverse scaling and squaring method depicted previously.

In the special case of R being a spatial rotation matrices: $R \in SO(3)$, an analytic expression derived also exists for the associated logarithm $X \in \mathfrak{o}(3)$ [Davis 2010]:

$$X = \log(R) = \begin{cases} \mathrm{Id} & \text{, if } \theta = 0 \\ \mathrm{Id} + \dfrac{\theta}{2\sin\theta}(R - R^T) & \text{, if } \theta \neq 0 \text{ and } \theta \neq k\pi, k \in \mathbb{Z} \end{cases} \tag{2.31}$$

Where $\theta = \arccos\left(\dfrac{\operatorname{Tr}(R) - 1}{2}\right)$.

Now interestingly, given an affine transformation T of linear part A and transformation part t, its logarithm lies in the set of matrices that contain only zeros in last row and is closely linked to the one of its linear part:

$$\log(T) = \log \begin{pmatrix} A & t \\ 0 & 1 \end{pmatrix} = \begin{pmatrix} \log(A) & v \\ 0 & 0 \end{pmatrix} \tag{2.32}$$

Given that, since the type of an affine transform (rigid, affine...) is totally determined by the type of its linear part (rotation matrix, free matrix...), they directly inherit from their Lie group properties. Interestingly, in the specific case of A being the identity i.e the transformation is only a translation, we have $v = t$.

2.4.3 Infinite dimensional Lie group structure for diffeomorphisms

The group of diffeomorphisms parametrized by SVFs, together with the composition law $\circ$ shares all the prerequisites for being a Lie group except that it is not finite-dimensional. Despite that difference for which it is referred as an *infinite dimensional Lie group* and that causes some unsolved issues, a framework developed in [Arsigny 2006a] that applies some of the above-mentioned tools of Lie group theory to diffeomorphisms has proven its relevance.

By using the SVF parametrization of diffeomorphisms, their one-parameter subgroups are obtained through the integration of the associated stationary ordinary differential equation 2.25. A one-parameter subgroup of diffeomorphisms is given by the flow associated to this stationary ODE i.e. the family of elements: $\{\gamma(.,t) \in \operatorname{Diff}(M) \mid \gamma : \mathbb{R} \to \operatorname{Diff}(M)\}_{t\in\mathbb{R}}$ and v is the infinitesimal generator of this subgroup.

Given that, diffeomorphisms belonging to the above-mentioned one-parameter subgroup can be computed through an exponential map exp. The exponential of a SVF v can be defined as the flow at time 1 of the ODE expressed in Equation 2.25:

$$\exp(v) = \gamma(x, 1) \tag{2.33}$$

This leads to a definition of the logarithm log such that for a diffeomorphism ϕ close enough to the identity, $\log(\phi)$ is the only SVF v in the neighborhood of 0 such that $\exp(v) = \phi$. Exponentials and logarithms can be computed using the technique presented in Section 2.4.1.3. More

details about their implementations for diffeomorphisms parametrized by SVFs are available in [Arsigny 2006a]. SVF are therefore the Lie algebra of this subset of diffeomorphisms and the associated Lie bracket is given for u and v two SVF by:

$$[v, w](x) = \mathrm{Jac}(v)(x).w(x) - \mathrm{Jac}(w)(x).v(x) \tag{2.34}$$

Where $Jac(v)(x)$ is the Jacobian matrix of v at point x:

$$\mathrm{Jac}(v)(x) \triangleq \begin{pmatrix} \frac{\partial v_1}{\partial x_1}(x) & \dots & \frac{\partial v_1}{\partial x_n}(x) \\ \vdots & \ddots & \vdots \\ \frac{\partial v_n}{\partial x_1}(x) & \dots & \frac{\partial v_n}{\partial x_n}(x) \end{pmatrix} \tag{2.35}$$

The logarithm is not always well-defined and its computation is very costly. This statement is particularly true for diffeomorphisms as multiple SVF square roots are required, which have to be computed by gradient descent. Given that, it is preferable to limit its use as much as possible. Fortunately, the BCH formula allows the estimation of the composition of two diffeomorphisms only knowing their associated SVF thus not requiring logarithm computation. The theoretical justification underlying the use of the BCH for diffeomorphisms parametrized by SVF is a bit wobbly since diffeomorphisms are not a finite Lie group. Yet it as found its practical relevance in the context of image processing as in [Bossa 2007, Vercauteren 2008]. many registration algorithms such as in [Vercauteren 2008, Commowick 2012a] are nowadays implemented to directly estimate and update the transformation in the SVF domain thus only necessitating exponentiations to apply the transformation to the image.

To simplify notations, unless specified otherwise, the composition of two transformations associated to two SVFs v and w is performed via the BCH: $\exp(v) \circ \exp(w) = \exp(\mathrm{BCH}(v, w))$.

Taking advantage of the Lie group structure of diffeomorphisms parametrized by SVFs, one can express the power of a diffeomorphism defined as $T^\alpha = \gamma(\alpha) = \exp(\alpha \log(T))$. T^α is the flow at time α along the diffeomorphic path from the identity to T.

2.4.4 Log-Euclidean statistics on transformations

Let G be a Lie group and $\mathfrak{g}$ its associated Lie algebra. For example, in this work, G may be the set of affine transformations, rigid transformations or diffeomorphic transformations parameterized as SVF. $\mathfrak{g}$ being a vector space, if the field over which it lies is real, which is the case in the context of geometric transformations, one can define a norm. From this norm on $\mathfrak{g}$ emerge log-Euclidean statistics on G [Arsigny 2009, Arsigny 2006b] including:

A **log-Euclidean distance:** Given two transformations: ϕ_1, ϕ_2:

$$\mathrm{dist}(\phi_1, \phi_2) = \| \log(\phi_1) - \log(\phi_2) \| \tag{2.36}$$

Which happens to have a nice inversion-invariant property since $\log\left(\phi^{-1}\right) = -\log(\phi)$.

A **log-Euclidean Mean:** Given a collection of n transformations $\{\phi_i, \dots \phi_n\}$ and their associated weights $\{w_i, \dots, w_n\}$ such that $\sum_{i=1}^n w_i = 1$:

$$\bar{\phi} = \arg\min_{\phi \in G} \sum_i w_i \| \log(\phi) - \log(\phi_i) \|^2 \Rightarrow \bar{\phi} = \exp\left(\sum_i w_i \log(\phi_i) \right) \tag{2.37}$$

An scheme comparing the classical Euclidean mean and this topology preserving log-Euclidean mean is available in Figure 2.4.

This paves the way for averages on groups of geometric transformations while ensuring the result to that very same group. By operating on their Lie algebras, averages preserve their

properties such as invertibility, rigidity... This log-Euclidean framework is therefore a crucial tool in the context of registration and atlasing.

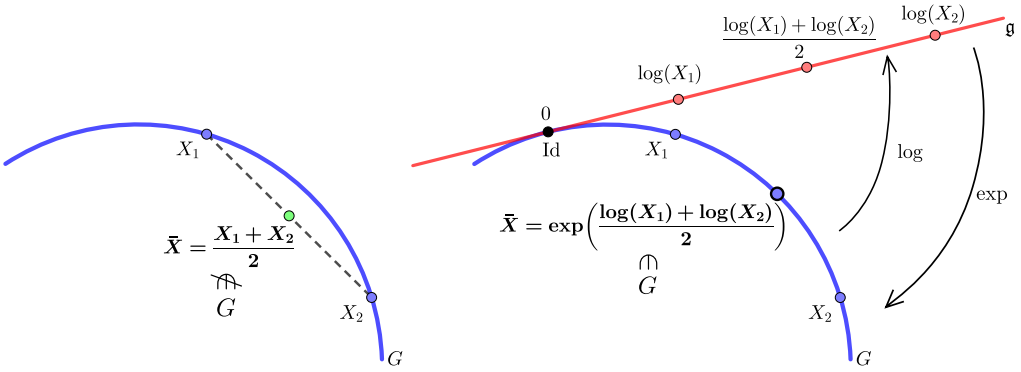

Figure 2.4: Average of two elements X_1 and X_2 of a group G through an Euclidean mean (left) and a log-Euclidean mean (right).

2.5 Conclusion

In this chapter we introduced two types of transformations. First the linear transformations that act globally on all coordinates though a single matrix multiplication. We saw notably how to decompose them and how to conveniently represent rotations using quaternions. We then evoked the infinite-dimensional diffeomorphic transformation and how to parametrize them into SVF and the LDDMM framework. We saw finally that, when equipped with a Lie group structure, one can perform statistics on those transformations.

Those are the geometric transformations that are commonly used in the mapping of two images namely the process of registration detailed in the next chapter. The quaternion representation of rotation will be a crucial tool for optimizing over the set of rigid transformations but also over a new type of linear transformations in Chapter 5. The SVF framework will be intensively used whether it is for transformation update in registration or averages in atlasing.

Chapter 3

Image registration

Contents

3.1 Generalities

Omnipresent in this thesis, whether in the context of atlas creation or brain growth modeling, registration deserves a dedicated part. While it is impossible to provide a complete review of the field, we will rather quickly present the generic concepts and a specific algorithm used in the rest of this thesis: block-matching. We will then focus in Chapters 3.2 and 3.3 more specifically on the geometric transformations involved, all already presented in the previous chapter.

3.1.1 Principle

Registration consists in the spatial matching of two images i.e. transforming one onto the other so that their anatomical structures match. In our case, we consider specifically 3D anatomical representations of brains acquired from a single or multiple MRI modalities (T1,T2-weigthed, proton density...), or even from other type of scanners (PET, CT...). This technique is widely used in clinical routine to reorient an image to make it more convenient for examination, to compare an individual with a reference or to monitor the evolution of a disease. It is also a crucial tool to produce atlases (i.e. average models of the brain), to propagate segmentations from a subject (or an atlas) onto another, to correct distortion or to extract developmental metrics when a longitudinal database of subjects is involved.

Usually one of the images is considered as the reference, and the other one is considered as the moving one. In this context, registration consists in finding the transformation T, among a set Ω of acceptable ones, that will *best* superimpose the transformed moving image $J \circ T$ onto the reference image I. Based on this definition, three main parts need to be defined for an algorithm: the set Ω, what *best* superimpose means, and how to optimize T [Brown 1992]. In the rest of the manuscript, the notation $J \circ T \sim I$ will be used to designate the transformed image J from the registration onto I.

Historically, methods are usually divided in two main categories which operate as follow:

The first one regroups **feature-based** approaches.

- It begins with a **feature extraction**: the identification of common geometric traits between the two images such as extremal points [Thirion 1996], crest lines [Declerck 1995], surfaces [Pelizzari 1989, Malandain 1993]....
- Then, an **optimization** is performed looking for the transformation that best matches analogous features between the two images, usually through least squares minimization of a given norm. Let $\{F_k \mid k = 1, \ldots, N\}$ be a collection of features such that $F_k(I)$ are selected on the reference image and $F_k(J)$ are the analogous ones in the moving image. The optimal transformation $\hat{T}$ can be computed by solving a problem of the form:

$$\hat{T} = \arg\min_{T \in \Omega} \sum_{k=1}^{N} \|F_k(I) - F_k(J \circ T)\|^2 \tag{3.1}$$

The features can be manually defined by an expert or automatically detected. Often performed through an iterative scheme, the feature matching aspect confers a certain tangibility and ensures a relative robustness. Based on purely geometric considerations, it may however sometimes be considered as too parsimonious as the extraction of sufficiently local features can be difficult to achieve.

The second category regroups **iconic** methods. Those are entirely based on the intensities of the voxels of the images and do not rely on pre-extracted features. Instead they work as follow:

- A **similarity measure** sim that quantifies the resemblance in terms of intensity between the voxels of the two images needs to be defined.
- The registration is then performed through an **iterative optimization procedure** seeking the transformation that maximizes this similarity criterion sim leading to a problem of form:

$$\hat{T} = \arg\max_{T \in \Omega} \; sim(I, J \circ T) \tag{3.2}$$

As detailed in [Roche 2000], the similarity measure must be chosen based on the assumed relationship (functional or not) between the images intensities once registered:

- Identity relationship: the sum of squared differences of the intensities can be considered, especially for mono-modal images of a single subject.
- Affine relationship: a good choice may be the correlation coefficient which quantifies how strong this linear relationship is. This measurement is especially well suited for mono-modal registration but also in the multi-modal case when used at a local scale.
- Functional relationship: in that case, no assumption is made regarding the function mapping the intensity of one image to the other, except that it is still a continuous function. This makes it therefore appropriate for multi-modal registration. Among these techniques, the correlation ratio developed in [Roche 1998] is quite popular.
- Statistical relationship: even less restrictive, it mainly contains the mutual information detailed in [Wells 1996, Maes 1997]. Based on information theory, this last measure is computed from joint histograms of the two images thus giving it a universal aspect.

In order to find the transformation that maximizes this similarity criterion, an optimization scheme must be put in place. Gradient descent or Powell's methods are commonly used. The similarity measures are however known to be non-convex with respect to the transformation

parameters resulting in potential swamp in local minima. Solving for this generally involves an iterative, multi-scale procedure requiring downsampling interpolations for the resampling of the transformed moving image at each step further worsening the non-convex aspect.

This separation in two categories can however be permeable, some approaches such as block-matching detailed in Section 3.1.2 having both iconic and feature-based aspects.

If we are dealing with two images of the same subject, it is referred as **intra-subject** registration. Unless there is a longitudinal aspect, we assume that the two representations of the brain are identical in terms of shape and we therefore only want to realign the two volumes without geometric warping or stretching. The set Ω is therefore restricted to **rigid** transformations that are only composed of rotations and translations. This occurs typically when dealing with two (undistorted) images of a subject coming from different modalities or acquired at different times (in the case of no major evolution between the two acquisitions) but also when several volumes are acquired sequentially (e.g. in functional MRI).

On the other hand, in the case of brains from different subjects being registered, because of the **inter-subject** variability, more degrees of freedom are needed. To compensate for global changes in terms of scale, one can open the field of acceptable transformations to **affine** ones that are composed of stretches in addition to rotations and translations. Doing so, the whole moving image is transformed the same way to globally match the size and orientation of the reference one.

However, those are not flexible enough to take into account local changes in the anatomies. This requires more subtle transformations that can handle specific displacements for each particle of the moving image. Those non-global transformations studied in depth in Chapter 3.3., usually referred as **non-linear**, however need some safeguard to prevent aberrations through the introduction of constraints and regularization terms to ensure a certain degree of smoothness, invertibility... This leads to energy maximization problems of form:

$$\hat{T} = \underset{T \in \Omega}{\arg\max} \;\; sim(I, J \circ T) + reg(T) \tag{3.3}$$

Several measures have been developed in order to evaluate the accuracy of registration algorithms. Among the most widely used are overlap score (Dice, Jaccard) of segmented regions and image similarity, even though their reliability has been questioned in [Rohlfing 2012].

The choice of the acceptable transformations (rigid, affine, non-linear...) for the registration is called the **transformation model**. The study of the transformations involved in registration and how to find the optimal one according to the transformation model will be the main focus in the following chapter neglecting somewhat the purely iconic aspects such as similarity measures. For a more exhaustive overview of registration see [Hajnal 2001], an excellent survey is also available in [Gholipour 2007] or more recently in [Oliveira 2014]. For a retrospective view of the field and questioning about the usual classifications of the registration methods, see [Viergever 2016]. For a global point of view of both feature-based and iconic registration techniques, see [Malandain 2006] (in french).

3.1.2 Generalities about block-matching registration

Before digging deeper into the depiction of global and non-global registrations specificities, some generalities about block-matching will be exposed. This approach is indeed the one of interest in this thesis. To go beyond the hereafter overview, see the appendix B of [Commowick 2019] where implementation details and variants are fully detailed.

At the beginning of the algorithm, the moving image is resampled into the grid of the reference one. A set of blocks is established in the reference image. A **block** is a subpart of an image, a set of voxels in a neighborhood defined around a given point of the space. They are

usually chosen of cuboid shape for simple implementation and should be large enough (several times a voxel size in every direction) to keep the similarity measure meaningful. The blocks must be numerous in order to overdetermine the system as much as possible for a good accuracy (the blocks may overlap). Then, the two following steps are iterated until convergence:

1. **Matching:** for a set of blocks established in the reference image, homologous blocks best satisfying a similarity criterion are searched in the moving image.

2. **Aggregation:** the local relations between the homologous blocks are combined to produce an overall transformation updating the current one.

Block-matching strategies present therefore some kind of a feature-based / iconic duality. Indeed, the features are defined on the reference image and their counterparts are searched in the moving image using multiple local iconic matchings.

3.1.2.1 Matching

This is a generic step, it is performed the same way whatever the transformation model (linear or not) of the registration. It can be viewed as a feature extraction that is performed by locally maximizing a similarity criterion therefore based on iconic considerations.

Homologous blocks to the ones in the reference image are searched in the (resampled) moving image. They are the ones that locally best satisfy the chosen similarity criterion with the ones in the reference image. For each defined block in the reference image, the search is, for computational reasons, only performed in a neighborhood (typically several block sizes) around its center.

- In [Ourselin 2000], an exhaustive search is performed over discrete, grid-based translations. This results in point-to-point correspondences between the center of the homologous blocks of the two images. This approach is computationally interesting but the restriction to translations for the relation between blocks may suffer scarcity in case of large rotations or subvoxel displacements.

- To address this concern, it was proposed in [Commowick 2012b] in the case of rigid registration and in [Commowick 2012a] for the case of diffeomorphic registration, to perform a search over local rigid transformations. Doing so, the candidate blocks are no longer constrained to the grid and resampling is therefore needed in order to compute a similarity measure. Exhaustive search is no longer possible and an optimization scheme has to be chosen. This results in a much more expensive process even though derivative-free algorithms in [Powell 2009] have shown good efficiency. We end up with more than simple point-to-point correspondences since we actually obtain a set of local rigid transformations, one for each block. The same approach is imaginable searching over the set of affine transformations but the computation cost may appear prohibitive.

Together with each relation between two homologous blocks, one can associate a weight that quantifies how strong this relationship is. It can typically be proportional to the similarity measure between the blocks.

3.1.2.2 Aggregation

This step is totally dependent upon the chosen transformation model. It consists in gathering all the local relations between the blocks extracted in the previous step and aggregate them into an overall update transformation. It therefore relies both on which kind of relations there is between the blocks and which kind of overall transformation is sought. Different configurations are exposed in the next chapters:

- The aggregation into a linear transformation in the case of a point-to-point correspondence between the blocks is detailed in Section 3.2.2.
- The aggregation into a non-linear transformation is detailed in Section 3.3.2.4.

3.2 Linear registration

3.2.1 Generalities

Preliminary disambiguation: The term linear registration is widely used to designate registrations where the set of acceptable transformations is restrained to rigid ones or any other type or affinity. However, theoretically, these do not generally belong to the set of linear transformations. Indeed, the introduction of a translational part causes a shift of the origin which is in contradiction with the properties of linear maps (see Equation 2.1). This ambiguity comes from the definition of a linear function in other fields than linear algebra and geometry such as calculus and statistics where any function whose graph is a straight line is considered as linear. That being said, we will comply with the standing practice in the rest of this manuscript.

In case of images from different modalities, registration methods using mutual information as similarity measure have been quite dominant for about twenty years already. This popularity is explained by the flexibility of that kind of similarity which does not require a well defined relationship between the intensities of the two images. It is especially powerful to align CT/PET/MR images of a single anatomy therefore only necessitating a rigid transformation but it is also widely used in the mono-modal case and for affine transformations. The maximization of the criterion is usually performed in a global fashion (at the scale of the whole image) such as in [Wells 1996] and [Maes 1997] where it showed nice results in the case of rigid registration. The correlation ratio depicted in [Roche 1998] is also a relevant choice in the multi-modal configuration.

Other methods rely on local similarities. Among this second category of approaches, block matching strategies exposed in [Ourselin 2000] and [Commowick 2012b] have gained in popularity especially in the linear case. The local similarity criterion to be maximized can typically be the correlation coefficient which quantifies how strong is the affine relationship between the intensities of two homologous blocks. The general concept of block-matching has been exposed in Section 3.1.2 and particularly the matching step in Section 3.1.2.1 which is independent upon the transformation model. In the following, the aggregation part consisting in the research of an acceptable (with respect to the transformation model) overall transformation from local relations between the blocks will be detailed for different types of linear transformations. This step also relies on the kind of relations coming from the matching step, whether it is a point-to-point correspondence or a linear transformation for each couple of homologous blocks. We consider here for the sake of conciseness that the relations between blocks are translations.

Not much revolutionary is happening nowadays in the field of linear registration methods, yet some ideas for robustness improvement have emerged for existing frameworks. In the case of rigid registration, [Prima 2013] proposed to take into account the bilateral symmetry of the brain through a constraint on the rigid transformation such that the mid-sagittal planes of the two brains are ensured to be superimposed. We also use while transformation decomposition in Chapter 7 for rigid registration of brains of different sizes.

3.2.2 Optimal transformations from two sets of paired points

The matching step outputs two sets of paired points: x and y that are in our case the centers of the homologous blocks. The second step (aggregation into a global transformation) however is dependent on the type of linear transformation we want to determine leading to an adapted

optimization in each case. The following is not restricted to block-matching algorithm but to any method that first established a correspondence between points of the two images.

This optimization step consists in finding, in the set of eligible transformations, the one that best maps x onto y. Let $x = \{x_1, \ldots, x_M\}$ and $y = \{y_1, \ldots, y_M\}$ be two sets of M paired points coming from the matching step. For a global transformation with linear part A and translational part t, the least squares problem associated to the matching of x and y consists in the minimization of the following criterion C:

$$C(A,t) = \sum_i \|y_i - (Ax_i + t)\|^2 \tag{3.4}$$

Remark. *For the sake of clarity we present a version with a non-weighted least squares problem but the reasoning is the same with a weighted one.*

3.2.2.1 Optimal translation

Computing the derivative of C with respect to the translation part, we get:

$$\frac{\partial C}{\partial t} = -2\sum_i (y_i - Ax_i - t) \tag{3.5}$$

Let $\bar{x} = \frac{1}{M}\sum_i^M x_i$ and $\bar{y} = \frac{1}{M}\sum_i^M y_i$. After some algebraic operations, we get:

$$\frac{\partial C}{\partial t} = 0 \text{ for } \boxed{\hat{t} = \bar{y} - \hat{A}\bar{x}} \tag{3.6}$$

The optimal translation $\hat{t}$ can then be directly obtained from the optimal linear part $\hat{A}$ (independently of the type of linear transformation) and the barycenters of the two sets of points as developed in [Pennec 1996].

3.2.2.2 Optimal linear part

Now, let $x'_i = x_i - \bar{x}$ and $y'_i = y_i - \bar{y}$ be the barycentric coordinates. Since $\hat{t}$ can be directly expressed from $\hat{A}$, the problem can be simplified as the minimization of:

$$C'(A) = \sum_i \|y'_i - Ax'_i\|^2 \tag{3.7}$$

Affine case

In the case of the linear part being affine, there is no constraint on A. We thus compute directly its derivative:

$$\frac{\partial C'}{\partial A} = \sum_i 2Ax'_i{x'_i}^T - 2\sum_i y'_i{x'_i}^T \tag{3.8}$$

A closed form solution $\hat{A}$ can therefore be easily found as shown in [Pennec 1996].

$$\frac{\partial C'}{\partial A} = 0 \text{ for } \boxed{\hat{A} = \sum_i y'_i{x'_i}^T \left(\sum_i x'_i{x'_i}^T\right)^{-1}} \tag{3.9}$$

Rigid case

In the case of a rigid transformation, the linear part A is constrained to be a rotation matrix:

$$\begin{cases} A^TA = AA^T &= \text{Id} \\ \det(A) &= 1 \end{cases} \tag{3.10}$$

Those constraints lead to more complicated lagrangians but a closed form solution can be found as well. There are mainly two methods to solve this problem. The first, which has the advantage of being valid in any dimension, uses singular value decomposition. It is depicted in [Pennec 1996], based on [Umeyama 1991]. The second one, developed in [Horn 1987], makes use of unit quaternions to parametrize spatial rotation. It is therefore quite elegant but only valid in 3D space. It is this approach that will be briefly depicted here because of its kinship with the work we developed in Section 5.3.

As seen in Section 2.2.2.3, the rotation induced by the matrix A can be expressed using unit quaternions. The problem then becomes (see Appendix B.1):

$$\tilde{C'}(q,S) = \sum_i ||(0,y'_i) * q - q * (0,x'_i)||^2 \tag{3.11}$$

Where q is a unit quaternion and $*$ is the quaternion multiplication. As explained in Section 2.2.2.2 and following the same notations, one can express this quaternion product as a matrix product using L and R matrices respectively associated to left and right multiplication.

Since $(0,y'_i)$ and $(0,x'_i)$ are pure quaternions, their associated multiplication matrices are skew-symmetric. It leads to:

$$\tilde{C'}(q,S) = q^T \left(-\sum_i \left(L_{y'_i} + R^T_{x'_i} \right)^2 \right) q \tag{3.12}$$

For further computation, we denote $B_i = -\left(L_{y'_i} + R^T_{x'_i} \right)^2$ and $B = \sum_i B_i$. A lagrangian with unit constraint $q^T q = 1$ has then to be added to ensure a unit quaternion:

$$\Lambda = q^T B q - \lambda (q^T q - 1) \tag{3.13}$$

Leading to:

$$\frac{\partial \Lambda}{\partial q} = (B - \lambda I_4) q \tag{3.14}$$

Solving $(B - \lambda I_4)q = 0$ amounts finding the eigen vectors of B. More precisely, the global minimum $\hat{q}$ is the eigen vector of B associated to the smallest eigen value as shown in [Horn 1987, Pennec 1996].

3.3 Non-linear registration

3.3.1 Generalities

The anatomic variability being very large and subtle, the use of global transformations that operate the same way on all voxel coordinates cannot be flexible enough when a refined matching is needed for different subjects or for a single person whose anatomy has undergone local changes. In that context, the transformation is no longer characterized by a matrix but rather by a deformation field $u : \mathbb{R}^N \to \mathbb{R}^N$ that associates to each voxel x a displacement vector that links x to its transformed-self $T(x)$ such that: $T(x) = x + u(x)$. The high number of degrees of freedom of those transformations implies a greater volatility compared to linear registration algorithm. Given that, it is usually preferable to first roughly align the two images through an affine registration. Also it is mainly used within a pyramidal scheme in order to iteratively refine the matching.

In addition to the similarity term, a **regularization** term is added that will penalize the cost function to ensure some topological properties such as smoothness and invertibility. The cost function becomes therefore a trade-off between the similarity of the images and the constraints imposed on the deformation field. Non-linear registration algorithms are usually divided in two

main categories. The ones known as **parametric** methods rely on a limited number (less than the number of voxels) of control points where the transformation is estimated. Then a dense field is interpolated for each voxel. On the other hand, in **non-parametric** methods, each voxel has some degrees of freedom. Extensive reviews about non-linear registration methods can be found in [Sotiras 2013] and [Oliveira 2014]. A review of the usual non-linear geometric transformations, in addition to the ones exposed in Chapter 2, is available in [Holden 2008]. An evaluation of some of the most commons algorithms has been conducted in [Klein 2009].

Many registration algorithms lie in what is called in [Ashburner 2007] the **small-deformation framework**. In that context, a transformation $T_k = \mathrm{Id} + u_k$ is updated by simply adding the new deformation field v_k following: $T_{k+1} = \mathrm{Id} + u_k + v_k$. The resulting transformation is not invertible in general unless the deformations are small enough. This leads to either theoretical weakness or a relatively slow convergence.

On the other hand, in the **large-deformation framework**, transformations are updated through the natural operation on the group of diffeomorphisms which is the composition: $T_{k+1} = (\mathrm{Id} + u_k) \circ (\mathrm{Id} + v_k)$. Thus, the resulting transformation is also ensured to be a diffeomorphism. This includes LDDMM algorithms which are very clean from a theoretical point of view but may appear computationally extensive. Using the SVF parametrization of diffeomorphisms efficiency is improved at the cost of theory. Using this approach, one can benefit from Lie group properties leading to an update transformation following: $T_{k+1} = \exp(u_k) \circ \exp(v_k)$.

Diffeomorphisms evoked in Section 2.3 is often the best choice as transformation model for non-linear image registration since similar structures are assumed to be present in both images and thus a smooth bijective mapping is expected. Though, it does not fit the case where the brains to be registered contains additional material (e.g. tumor) or, on the contrary, lacks some (e.g. degeneration).

3.3.2 Parametric methods

Those methods require the construction of a grid (regular or not depending on the case) of control points underlying the image structure. To each of these control points is associated a given number of parameters that will characterize a local transformation. Those parameters can typically be a vector of $\mathbb{R}^3$ which contains a displacement along each three directions of space. The control points are moved individually in the direction that optimizes a similarity measure, defining local deformations. The parameters for any point of space in-between the control points can then be interpolated or approximated. Let U be the sparse set of transformations parameters at each control points and u the dense field defined at each point of space influenced by U. If, by constraint, $u(p_i) = U(p_i)$, we are dealing with **interpolation**. On the other hand, if there is a certain degree of uncertainty concerning the evaluation at the control points, an **approximation** is preferable where the exact matching constraint is relaxed.

3.3.2.1 Radial basis functions

Once the transformation parameters have been estimated for all control points, the parameters for any point of space in-between the control points can then be approximated by a linear combinations of the ones associated to control points, the contribution of each being modulated by the basis function:

$$u(x) = \sum_i B(\|x - p_i\|)U(p_i) \tag{3.15}$$

A major advantage of this approach is that the control points can be placed arbitrarily, no regularity constraint is required. A plethora of basis functions have been experimented, a comparative study of some of the most commons is available in [Zagorchev 2006], a topology preservation evaluation is conducted in [Yang 2011]. Among them, some rely on **infinite supports**:

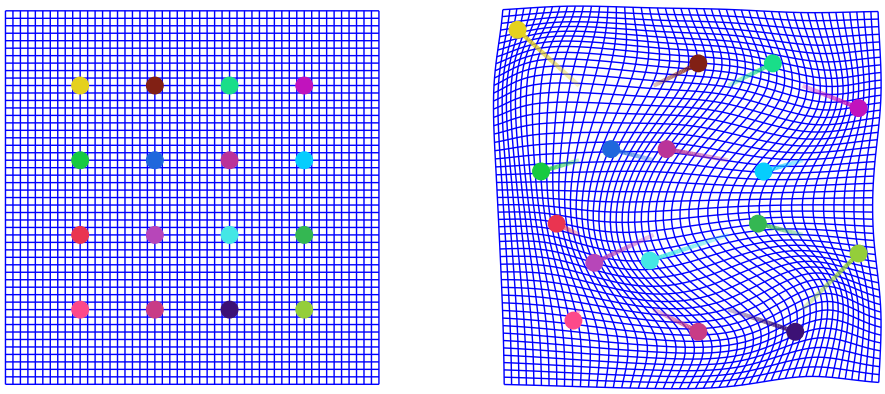

Figure 3.1: Regular grid before and after deformation parametrized by control points. Approximation using B-splines

- Thin-plate splines as in [Bookstein 1989, Bookstein 1991]
- Gaussian as in [Arad 1995]
- Hardy's multi-quadrics as in [Ruprecht 1995, Little 1997].

The infiniteness of the support implies that a control point influences the whole image. This may not be optimal in terms of computation cost. Also one might prefer a more localized area of influence leading to **compact supports**:

- Piecewise polynomial positive definite from [Wendland 1995] as in [Fornefett 2003].
- Truncated Gaussian
- Compact support thin-plate splines as in [Zhang 2008].

Those lists are far from exhaustive. We detail three of these algorithms to give an example.

3.3.2.2 Free-form deformation model

In [Rueckert 1999], then extended and generalized in [Schnabel 2001], it was proposed to approximate the displacement between the control points using **cubic B-splines**. This technique is very popular, so we are going to dwell on it a little bit.

Let a regular grid of control points that are denoted $p_{i,j,k}$. They are spaced by distances s_x, s_y, s_z such that $p_{i,j,k}$ is at position $(i.s_x \ j.s_y \ k.s_z)^T$ in the image voxel grid. Once a displacement $U(p_{i,j,k})$ at each control point has been estimated, one can approximate the displacement at any point x only using the 64 surrounding control points through tensor product of 1-Dimensional B-splines:

$$u(x) = \sum_{l=0}^{3}\sum_{m=0}^{3}\sum_{n=0}^{3} B_l(\delta_x)B_m(\delta_y)B_n(\delta_z)U(p_{i+l,j+m,k+n}) \tag{3.16}$$

Where:

$$B_0(x) = \frac{(1-x)^3}{6}$$
$$B_1(x) = \frac{3x^3 - 6x^2 + 4}{6}$$
$$B_2(x) = \frac{-3x^3 + 3x^2 + 3x + 1}{6}$$
$$B_3(x) = \frac{x^3}{6}$$

$$i = \left\lfloor \frac{x}{d_x} \right\rfloor - 1 \qquad j = \left\lfloor \frac{y}{d_y} \right\rfloor - 1 \qquad k = \left\lfloor \frac{z}{d_z} \right\rfloor - 1$$

$$\delta_x = \frac{x}{s_x} - \left\lfloor \frac{x}{s_x} \right\rfloor \qquad \delta_y = \frac{y}{s_y} - \left\lfloor \frac{y}{s_y} \right\rfloor \qquad \delta_z = \frac{z}{s_z} - \left\lfloor \frac{z}{s_z} \right\rfloor$$

The compactness of the support is computationally appealing. Also, the resulting deformation field is smooth, without however being diffeomorphic in general. Two different approaches have been discussed in [Rueckert 2006] to ensure the transformation obtained by B-splines to be one-to-one and therefore diffeomorphic.

- The first one uses soft constraints. In addition to the similarity measure, a penalty term is brought the function cost to be minimized for the registration. This penalty term is activated when $\det(\mathrm{Jac}(x, y, z))$ goes below a given threshold and explodes as this determinant of the Jacobian tends to zero.
- The second one uses hard constraints. If the displacement of the control points is small enough, the transformation is ensured to be diffeomorphic. The bounds on the maximum amplitude of the displacement of the control points that guarantee the local injectivity of cubic B-splines has been established in [Choi 2000]. This leads to displacements that are however generally too small to model realistic transformations. Yet, the set of diffeomorphism together with the composition law being given a group structure, one can compose a succession of those small diffeomorphic displacements to produce a larger one.

3.3.2.3 Polyaffine

In the above-mentioned examples, the transformation parameters that were linearly combined were displacement vectors. The same reasoning can be applied to transformation matrices. To each control point is attached a local linear transformation, rigid or affine in general. Those are then fused to obtain an overall transformation locally affine or rigid. In the polyaffine framework designed by [Arsigny 2006b, Arsigny 2009], the fusion is performed using a log-Euclidean mean:

$$T(x) = \exp\left(\sum_i \log(T(p_i))B(\|x - p_i\|)\right) \tag{3.17}$$

The resulting **log-Euclidean polyaffine transformation** (LEPT) has nice properties: it is smooth and invertible, the inverse is also a LEPT, and it is affine-invariant. LEPT are used in registration notably in [Commowick 2008] (following the theoretical framework from [Arsigny 2009]) where areas of the brain have first been segmented and independently registered using affine transformations. In this context, the log-Euclidean average was also used as a regularization term for the affine matrices computed.

3.3.2.4 Block-Matching

Generalities about block-matching have been presented in Section 3.1.2. Even though this is the non-linear registration algorithm that will be used for experiments in the next chapters, no contribution is to be noted for it in this thesis thus the treatment will be reduced compared to the linear case.

One assumes that the matching step outputed for each block a linear transformation that best matches it to the moving image. Each center of the block can therefore be viewed as a control point p_i to which is associated a transformation A_i. In the method proposed in [Commowick 2012a] and lately updated in Appendix B of [Commowick 2019], it is proposed to directly estimate an update SVF from the A_i.

To do so, a simple method is to consider a sparse set of *log-vectors* U attached to the control points following $U(p_i) = \log(A_i)p_i$. A (dense) SVF u can then be computed at any point of space through a Gaussian kernel also incorporating a weighting taking into account the strength of the similarity between the blocks.

To ensure a more efficient outliers rejection, another method has been imagined in the same papers which is similar to an M-smoothing filter [Mrazek 2006]. Following this approach, a *log-transformation* is estimated at each voxel through the minimization of a cost function. At a

given voxel, this cost function penalizes both for a distance to the control points and a distance between the estimated transformation and the ones associated to the control points. The optimization is performed through gradient descent to get the update SVF. The SVF composition is done as in [Vercauteren 2008] using the BCH formula [Bossa 2008].

In the case of blocks being defined at each voxel, block matching approaches can be viewed as non-parametric methods. This is the case of the algorithm depicted in [Ardekani 2005] that happens to be one of the top performers of the evaluation conducted in [Klein 2009].

3.3.3 Non-parametric methods

The non-parametric qualifier is a bit of an abuse of language here. Actually it is more that there are so many parameters that each voxel has 3 degrees of freedom.

3.3.3.1 Demons

The demons approach can be summarized by an unconstrained update followed by a gaussian smoothing. It has been imagined in [Thirion 1998] to consider image registration as a diffusion process. By analogy to Maxwell's work in thermodynamic, **demons** are imagined at each voxel locations that push the voxels of the moving image according to the local characteristics of the images.

Working in a iterative way, a deformation u that update an existing deformation s is computed voxel by voxel. The s is then updated by a regularization of $s+u$ to provide smoothness properties. Using optical flow equations, one can estimate a deformation for each voxels through the following formula:

$$u_{k+1}(x) = \frac{I(x) - J(x + s_k(x))}{\|\nabla I(x)\|^2 + (I(x) - J(x + s_k(x)))^2} \nabla I(x) \tag{3.18}$$

The demons locally push along the intensity gradient of the reference image direction or the opposite depending upon the intensity difference of the two images. An elastic regularization through Gaussian smoothing is then applied.

Following this kind of algorithm, there is for each voxel a direct formula to compute the associated displacement leading to a high efficiency. However, the way it works may appear quite ad-hoc since it is unclear when, why and how it converges. Digging up into the theoretical understanding of the demons algorithm, [Pennec 1999] has shown it is actually closely linked to a second order gradient descent on the SSD criterion.

An adaptation of the demons approach into an energy minimization problem was proposed in [Cachier 2003]. It involves the introduction of an hidden variable c, a vector field that attracts the points of the moving images to their correspondence in the reference one while u is a smooth vector field constrained by a regularization reg leading to an energy to minimize of form:

$$E(c, s) = \underbrace{\alpha\|I - J \circ c\|^2 + \beta\|c - s\|^2}_{\text{Correspondence energy}} + \gamma reg(s) \tag{3.19}$$

This leads to an alternate optimization. The correspondence energy is minimized with respect to u. Using optical flow equation, it results in an expression for u very similar to Equation 3.18. The field c is then updated in this so-called **additive demons** following $c = s + u$. The regularization part is taken care of through Gaussian smoothing of c.

Now, even if the demons framework appears cleaner using this energy minimization some kind of discomfort remains using a geometrically unnatural additive update. To overcome that burden, it was proposed in [Vercauteren 2007, Vercauteren 2009] to update the transformation field through a more geometrically appropriate operation: the composition, thus leading to the

so-called **compositive demons** approach. The field c is updated in this configuration following $c = s \circ (\mathrm{Id} + u)$.

Once again, despite the improvements of this compositive approach compared to the additive version, one can reproach some aspects and especially the fact that it does not yield invertible transformations. In the very same [Vercauteren 2007, Vercauteren 2009], a **diffeomorphic demons** is introduced. Taking advantage of the SVF detailed in Section 2.4.3, the field c is updated following $c = s \circ \exp(u)$. This has been reformulated into a so-called **log-domain demon** in [Vercauteren 2008] exploiting logarithms in a smarter and more efficient way through notably the use of the Baker-Campbell-Hausdorff formula (see Section 2.4.1.2) and extended with a symmetric design.

One of the latest variants, the **LCC-demons** developed in [Lorenzi 2013], also presents a symmetric log-domain design but uses local correlation coefficient as similarity measure and shows implementation improvements.

The demons approach is therefore rather a generic framework than a specific algorithm. A nice tutorial about demons registration, overviewing the framework from the early Thirion's idea until the diffeomorphic version, is available in [Vercauteren 2010].

3.3.3.2 LDDMM

Formulating the registration problem under the LDDMM framework is probably the most elegant on the theoretical point of view. Indeed it proposes to compute the geodesic namely the path of minimum length along the Riemannian manifold of diffeomorphisms that links the two images. The problem takes the form of the following minimization [Beg 2005]:

$$\hat{v} = \arg\min_{v} \left(\int_0^1 \|v\|_V^2 dt + \lambda \|I \circ \phi(x, 1) - J\| \right) \tag{3.20}$$

Where v is a time-varying velocity field, $\|.\|_V$ an appropriate norm on v. The first terms accounts for the path length over the group of diffeomorphisms while the second is a SSD criterion on image intensities whose contribution is modulated by a weight λ.

The cost function in Eq 3.20 can be optimized through gradient descent. Each iteration however necessitates ordinary differential equation integration to compute the diffeomorphic path. Usually done via Runge-Kutta, this can be computationally extensive.

Many variants of the LDDMM framework are available, with various similarity measures, symmetric implementations [Avants 2008]. A noteworthy example is the ANTs software depicted in [Avants 2011] that includes the Syn algorithm that showed top results in [Klein 2009].

3.4 Conclusion

Many algorithms have been developed in order to match two images. Those rely on the optimization over various transformations sets evoked in Chapter 2. In the following, we will adopt block-matching methods for registration, which are based on local similarities, as they allow versatile implementations, able with the same core, to optimize many different types of transformations. Those were implemented by the team in Anima [Anima] for both the linear case [Commowick 2012b] and the non-linear one [Commowick 2012a] (more recent precisions in Appendix B of [Commowick 2019]). They have shown reliability and good performances through their intense use in the team. Our non-linear block matching algorithm is based on the SVF parametrization for diffeomorphisms such that transformations can easily be updated and averaged by taking advantage of the log-Euclidean framework.

We will see in the next chapter how, through operations on the transformations resulting from registration processes, one can produce an average shape of the brains of a population, i.e. an atlas.

Chapter 4

Atlasing

Contents

4.1 Generalities

An **atlas** is a generic term covering several uses.

In the sense of [Talairach 1988], it consists in a single post-mortem anatomy of the left part of the brain of a sixty years old woman dissected and photographed, symmetrized to obtain a whole brain representation. Originally conceived as a reference for stereotaxy, it is delivered together with anatomical fiducial points and stretching instructions to be used for a rough spatial normalization.

The term is also often used to refer to a single structural image of an individual together with an associated segmentation map, i.e. labeled areas delineated by an expert. It is used in this context to propagate the joint segmentations to another subject through registration [Miller 1993, Bondiau 2005]. As shown in [Heckemann 2006, Aljabar 2009], the propagation and fusion of multiple couples of anatomic images and labels maps increases the accuracy [Iglesias 2015]. This is referred as multi-atlas segmentation. A review of atlas-based segmentation is available in [Cabezas 2011].

However, the definition of interest here is the one that considers an atlas to be an **average model of the brain both in terms of shape and intensity**. It is therefore a powerful tool to understand brain variability, to compute statistics of to identify for differences on populations [Whitcher 2007] or to segment regions. An atlas is said to be **cross-sectional** when the data used for its construction are each collected at a single point in time, like a snapshot of the population. They are ideally made from a large number of subjects by combining their images through registration and transformation composition. They are willingly unbiased in relation to the subjects of which they are composed so as to best represent the population or serve as neutral reference for normalization.

An extension to those *temporally static* atlases are **longitudinal** (time dependent) **atlases** which allow in addition the comprehension of brain development or aging, to highlight changes in growth, shape, structure etc. Technically, the term longitudinal is reserved for studies that follow the same sample of individuals repeatedly over time. However, and this is the case in this manuscript, the longitudinal term is widely overused so that it often refers to any atlas

with a temporal component including multiple cross-sectional ones i.e. performed for multiple timepoints. The latter 4D models are based on a set of 3D atlases each for a desired age using e.g. weight functions that modulate the contributions of the subjects according to their age fit with that timepoint.

Focus will be made in this manuscript on the methodology underlying the atlas creation process rather than on potential clinical applications. Moreover, only methods producing image atlases will be studied in detail even though it also exists for curves and surfaces as in [Durrleman 2009]. We will detail how to use the theoretical notions developed in Chapter 2 and the image processing tools from Chapter 3 in order to produce atlases with interesting properties.

A critical issue while validating an atlasing method is the absence of ground truth. Yet, some aspects can still be evaluated. Among the ones that need to be particularly taken care of, one can consider:

- The **bias**: Many atlasing methods rely on an initial reference image; This may lead to an over-influence of the associated subject compared to the others. The bias is the representative criterion of this over-influence. However, not all biases are always a problem. Indeed a rigid bias is not important since it only affects the position and orientation. It can even be desirable if the reference image has a convenient orientation. Also some atlases are designed to be unbiased up to an affine transformation thus ignoring bias induced by global changes in size. This is typically the case when only the local inter-subject variability is under consideration and all subjects have roughly the same age. For longitudinal atlases however affine bias has to be eliminated to account for developmental growth.

- The **image quality**: Most atlasing methods contain in their midst a step consisting in an average of the subject images after they have undergone transformations to align them. This alignment not being exact and relying on the assumption that the structures are identical, it necessarily generates blur. This blur is heavily dependent upon the accuracy and the number of dof (degrees of freedom) of the registration algorithm involved in the computation of the above-mentioned transformations. Another source of blur are the resampling processes inherent to the fact that we are working with samplings on discrete grids. Those resamplings therefore have to be used sparingly; most of the well-implemented algorithms only require one for each subject. Given that, a measure of sharpness is interesting for image quality assessment.

- The **computational cost**: Atlasing methods are known for their heavy computational cost which increases with the number of subjects involved. The source of it comes mainly from registrations and operations on transformations. Those image processing tools generally needs to be run numerous times to take into account all the subjects and reduce the bias. In some methods, a single groupwise registration is required but this one is massive by itself. Yet, the creation of an atlas is not a routine procedure, so that even a high calculation cost can sometimes be tolerable.

For longitudinal atlases, one can in addition consider:

- The **temporal accuracy**: It is of great importance to assess if the 3D sub-atlases are well representative of the ages they are supposed to model. An irregular repartition of the subjects in terms of age may indeed lead to temporal errors.

One can consider the dof of an atlas as the dof of the transformations used in the registrations inherent to its creation. One of the earliest average model is the MNI-305 from [Evans 1993, Collins 1994]. It was created through a landmark registration of 250 young adults onto the Talairach atlas, then completed by 55 other subjects through affine (9 dof) registration. The low number of dof leads to a quite image (see Figure 4.1a). In the same vein was created the

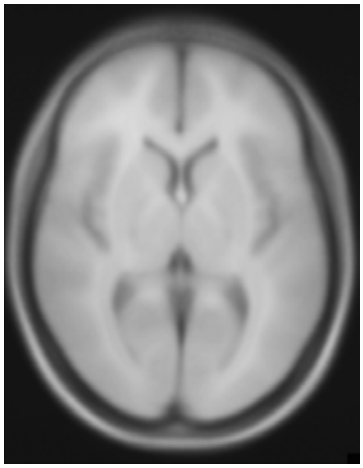

(a) affine MNI-305[a]

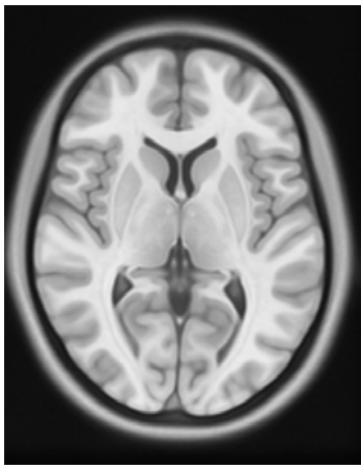

(b) non-linear ICBM-152[b]

[a] MNI-305 - [Evans 1993, Collins 1994]
https://www.mcgill.ca/bic/software/tools-data-analysis/anatomical-mri/atlases/mni-305

[b] ICBM-152 v. 2009c symmetric - [Fonov 2011]
http://www.bic.mni.mcgill.ca/ServicesAtlases/ICBM152NLin2009

Figure 4.1: Two Talairach-like brain atlases

ICBM-152 [Mazziotta 2001], also through affine registrations, using better quality images from 152 young adults. Using the same database, [Fonov 2011] dramatically increased in the number of dof through the use of non-linear registration resulting in a much more refined, sharper result (see Figure 4.1b). Both those atlases are qualified of Talairach-like in the sense that they are totally biased (voluntarily) toward it.

In [Fréchet 1948] the Euclidean notion of mean is generalized in any metric space (Ω, d) following:

$$\bar{x} = \arg\min_{x \in \Omega} \sum_i d^2(x, x_i) \tag{4.1}$$

By translating the distance between two images as the amount of deformation needed to map one to the other, i.e. the distance between the identity and the transformation from the registration of one to the other, one can reformulate the average image model problem using the Fréchet mean in the space of transformations as in [Joshi 2004].

To produce an unbiased atlas, two main families of approaches, detailed in the next sections, are commonly used:

- **Template-based** approaches require the choice of an initial reference image onto which each subjects will be registered. The bias toward this first reference is then compensated using the inverse transformations from the registration. See section 4.2 for more details.
- **Template-free** approaches on the other hand do not rely on an initial reference image thus avoiding the introduction of a bias. They can be subdivided into two categories:
  - **Pairwise** methods that require to register each subjects to all the others. This generates unbiased versions of the subjects that are then averaged.
  - **Groupwise** methods propose to directly compute an average model through a group-wise registration of all the subjects simultaneously.

Those different approaches have all in common that they first establish a set of transformations to map the images onto a common space and then average the transformed images to create

the atlas. A particular focus will be made on the template-based approach since it is the one we will be using.

Reviews of atlasing methods are parsimonious compared to the registration case. One can however mention [Dickie 2017] for a review of existing atlases where the under-representation of childhood and elderly populations is notably pointed out. For global point of views of the domain, see [Evans 2012] and [Thompson 2010].

In the following, it will be assumed that we want to compute an atlas from the set of n images $\{I_1, \dots, I_n\}$.

4.2 Template-based approach

One of the first methods developed in this group was proposed by [Guimond 2000]. It consists in first registering all the subjects onto an arbitrary chosen image (typically one from the population or a pre-existing atlas). Then, an unbiasing transformation is computed through inversion and average of the transformations outputed from registrations. Finally, a new reference image is constructed by averaging the unbiased transformed subject images. This produces an atlas that can now be taken as a new reference image. By iterating the process, it leads to atlases that become less and less biased by the initial reference image.

Recipe

Let R be an initial reference image. The main loop of the algorithm consists in the following steps (see Figure 4.2a):

1. Registrations
   i. Affine registration of the I_i onto R in order find the affine transformations A_i that best superimpose each subject to the reference, leading to the transformed images $I_{i,A} = I_i \circ A_i$.
   ii. Non-linear registration of the $I_{i,A}$ onto I in order find the residual local variations T_i, leading to the transformed images $I_{i,T} = I_i \circ A_i \circ T_i$.
2. Creation of the new reference
   In the following, take $\theta_i = T_i$ for an atlas unbiased up to an affine transformation and $\theta_i = A_i \circ T_i$ to account for both affine and local bias.
   i. Averaging of the θ_i to produce $\bar{\theta}$ the mean transformation.
   ii. Inversion of $\bar{\theta}$ to produce the unbiasing transformation $\bar{\theta}^{-1}$.
   iii. Application of $A_i \circ T_i \circ \bar{\theta}^{-1}$ to each I_i producing images $I_{i,R}$ that are all aligned.
   iv. Averaging of the $I_{i,R}$ to produce the new reference image.

Registration being an imperfect process, a bias toward the first reference image remains. However, by iterating the above-mentioned steps, taking as new reference image the average of the registered subjects corrected in shape by the unbiasing transformation, the result should be less and less biased by the first reference image and therefore converge to the *theoretical solution* (see Figure 4.2b). One can see in [Li 2018, Hernandez 2007] that, for diffeomorphisms, this method can actually be comparable to a gradient descent of the Fréchet mean criterion (Equation 4.1) in the transformation group.

In the SVF framework, one can benefit from the log-Euclidean mean on the transformations to ensure a diffeomorphic result:

$$\bar{\theta} = \exp\left(\frac{1}{n}\sum_{i=1}^{n}\log(\theta_i)\right) \tag{4.2}$$

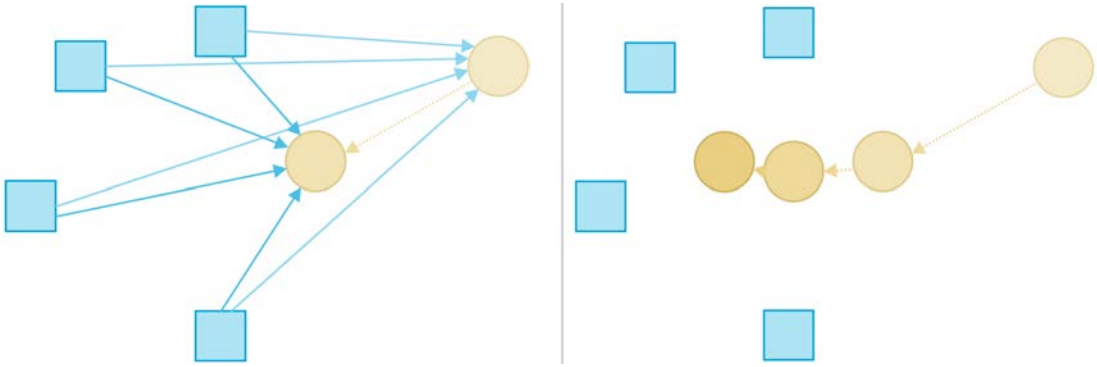

(a) Main loop (b) Effect of iterating

Figure 4.2: Overview of a template based atlasing method [Guimond 2000].

Effect of iterating

This aspect was studied in [Guimond 2000] using different measures such as the shape difference between the atlases at successive iterations or the average distance of the subjects to the atlas at current iteration. The first evaluates whether it converges and at what rate, while the second assesses whether it get closer to an average form of the subjects. Results show that the method quickly converges (stabilization already after four iterations) to an average model of the population.

Influence of the initial reference image

This facet was also studied in [Guimond 2000] through notably the measure of shape differences between resulting atlases built from different initial reference images. Result also show a quick decrease with the iterations suggesting that the method indeed corrects well for the bias. The small remaining differences are probably due to registration imprecisions.

Various implementations

The version developed in [Guimond 2000] provides a good average shape but it defines unbiased atlases up to an affine transformation, thus losing information on brain growth. Also, transformations are not guaranteed to lie in a diffeomorphic framework. In [Hernandez 2007], it is proposed to take advantage of the log-Euclidean framework to ensure diffeomorphic transformations, and to use a clever initialization reducing the bias. Unfortunately, the unfamiliarity at that time with the BCH formula in this context led to an algorithm requiring heavy logarithm calculations, making it de facto impractical for 3D images. In [Fonov 2011], diffeomorphic registration is used in the process but the Euclidean average of those may lead to non-diffeomorphic unbiasing transformations. On the other hand, in [Kuklisova Murgasova Deprez 2010, Kuklisova Murgasova Deprez a longitudinal version is presented that corrects well global size and shape (affine features) to account for brain growth but ignores local deformations, thus leading to a quite blurry result. In [Pontabry 2013] (in french), the method has been used to produce a longitudinal diffusion atlas based on a fetal population.

4.3 Template-free approaches

Those methods have the advantage to be unbiased by construction since they are not skewed initially toward a reference. A review is available in [Wu 2012].

4.3.1 Exhaustive pairwise

This approach has been developed in [Seghers 2004] and notably taken over for longitudinal extensions in [Serag 2012a]. It consists first in computing all the pairwise registrations between the subjects leading to an extensive number of $n(n-1)$ registrations (reducible to half of that using symmetric registration). Then, each subject undergoes an unbiasing transformation which is the average of all the transformations from him to the others. Finally, the atlas is constructed by averaging the resulting unbiased versions of the images. An overview of the method is shown in Figure 4.3.

Recipe

1. Registrations
   i. Affine registration of the I_i onto each I_j in order find the affine transformations A_{ij} that best superimpose each subject to another, leading to the transformed images $I_{ij,A} = I_i \circ A_{ij}$.
   ii. Non-linear registration of the $I_{ij,A}$ onto I_j in order find the residual local variations T_{ij}, leading to the transformed images $I_{ij,T} = I_i \circ A_{ij} \circ T_{ij}$.
2. Creation of the atlas
   In the following, $\theta_{ij} = A_{ij} \circ T_{ij}$.
   i. For each subject i, computation of $\bar{\theta}_i$, the average over j of the transformations θ_{ij}.
   ii. Application of $\bar{\theta}_i$ to each I_i producing images $I_{i,R}$ that are all aligned.
   iii. Averaging of the $I_{i,R}$ to produce the atlas.

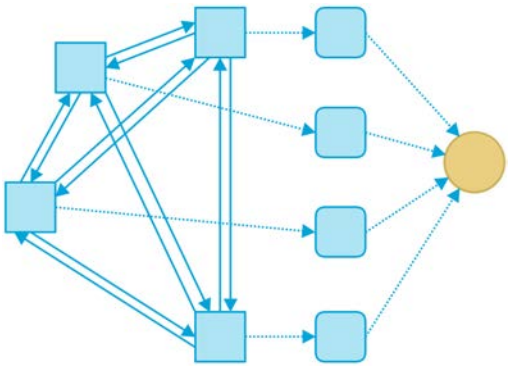

Figure 4.3: Overview of a pairwise atlasing method

This method is straightforward (by opposition to iterative) and unbiased by construction but requires a quadratic amount of registrations with respect to the number of subjects, which may be problematic in case of large datasets.

4.3.2 Groupwise

Following groupwise registration, all the images are simultaneously registered onto an hidden common space. This is done following an optimization scheme on a cost function covering two aspects:

- Ensuring the alignment through a similarity term between all the transformed images: $sim(I_1 \circ T_1, \ldots, I_n \circ T_n)$, that is to be maximized.

- Enforcing the convergence toward the centroid of the population. It can take a form similar to the Fréchet mean criterion (Equation 4.1): $\sum_i d^2(\mathrm{Id}, T_i)$, that is to be minimized as in [Lorenzen 2004, Joshi 2004]. It can also be set as a hard constraint on the sum of the transformations: $\sum_i T_i = 0$, as in [Bhatia 2004, Rohlfing 2009].

Recipe

1. Groupwise registrations

   i. Groupwise affine registration of the I_i that outputs, simultaneously for each i, affine transformations A_i and transformed images $I_{i,A}$, revealing an affine common space R_A such that $I_{i,A} = I_i \circ A_i \sim R_A$.

   ii. Groupwise non-linear registration of the $I_{i,A}$ that outputs, simultaneously fo all i, non-linear transformations T_i and transformed images $I_{i,T}$, revealing a non-linear common space R_T such that $I_{i,T} = I_i \circ A_i \circ T_i \sim R_T$.

2. Creation of the atlas by averaging of the $I_{i,T}$.

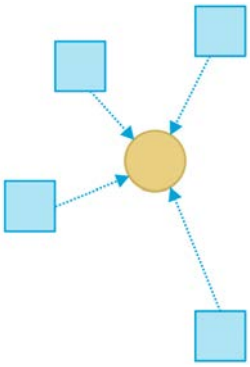

Figure 4.4: Overview of a groupwise atlasing method

This kind of approach is also straightforward and unbiased. Also, it only requires a single groupwise registration. The computation of this one, however, can be prohibitive. This method is notably implemented in the popular ANTs software following [Avants 2004, Avants 2010].

4.4 Including the temporal dimension

The above-mentioned methods are designed to well represent the centroid of a given population. However, the temporal dimension is totally ignored thus hindering assessment of anatomical development.

In case of a dataset containing a single observation of multiple subjects of different ages, the most common approach is to constitute a set of multiple cross-sectional 3D sub-atlases for chosen timepoints through kernel regression over the temporal domain. Within the construction of one of these sub-atlases, the contribution of each subjects is modulated by a kernel acting as a weight function that gives more influence to subjects closer in age to the associated timepoint.

In case of a (truly) longitudinal dataset i.e. containing several observations for each subjects taken at different times, one estimates a growth model for a given subject through intra-subject shape regression over time. Using spatio-temporal registrations on the different subject growth trajectories, a spatio-temporal atlas can be estimated as the mean scenario.

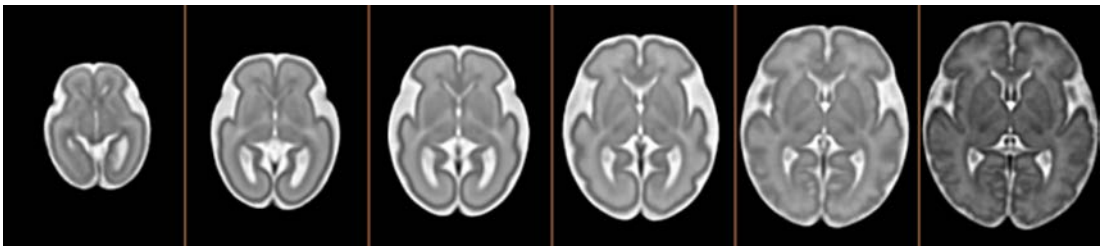

Figure 4.5: Longitudinal fetal brain atlas for six different gestational ages[c]

[c][Gholipour 2017] - http://crl.med.harvard.edu/research/fetal_brain_atlas/

4.4.1 Kernel regression

Following this method proposed notably in [Davis 2010, Ericsson 2008], a sub-atlas at time t is constructed such that the contribution of the subjects is modulated by a weight function that gives more importance to the ones closer in age to t. This weight function will intervene in the averaging processes inherent to the atlas creation.

The most common approach is to use the non-parametric regression technique known as kernel regression, developed in [Nadaraya 1964]. Following this, given a set of N observation $\{t_i, y_i\}_{i=1}^N$, one can can compute an estimator for y at a given time t using an average of the y_i weighted by a kernel K on the t_i, centered at t:

$$\hat{y}(t) = \frac{\sum_{i=1}^N K(t-t_i)y_i}{\sum_{i=1}^N K(t-t_i)} \tag{4.3}$$

Plethora of kernels are available, some on compact supports such as cosine or Epanechnikov, others on infinite supports such as logistic or Gaussian. The latter is the most commonly used, it is defined following:

$$K(u) = \frac{1}{\sigma\sqrt{2\pi}} e^{-\frac{u^2}{2\sigma^2}} \tag{4.4}$$

A Gaussian kernel regression for brain volumes over time of 308 children (between 0 and 19 years old) is shown in Figure 4.6. In this example it takes the form of a simple Euclidean average on volume values but one can imagine a reasoning in a similar vein for more complicated structures such as transformation groups through e.g. log-Euclidean means in the SVF framework. Since the support of the Gaussian kernel is infinite, a version truncated on a limited age range is often preferred, thus avoiding computations for subjects of negligible contribution. This kernel has a degree of freedom σ corresponding to the standard deviation, thus influencing the width of the kernel. One can take opportunity of this dof to adjust for uneven subject age distribution. In [Serag 2012a] it was proposed to adjust the width of the Gaussian such that an arbitrary chosen number of subjects have a weight above a given threshold. Working through an iterative procedure, the idea is to increase the width when there are too many subjects and, conversely, reduce it when there are too few. Though, this does not compensate for an asymmetric distribution around a considered timepoint. The choice is however not restricted to kernels, one can consider more flexible weight functions as soon as it associates to each subject i a weight w_i such that $w_i \geq 0$ and $\sum_i w_i = 1$.

The idea for the creation of a spatio-temporal atlas is therefore the following: for each desired timepoint t, construct a cross-sectional atlas using e.g. one of the methods detailed in Sections 4.2 and 4.3 but weighted for subjects closer in age to t to further influence the result. This temporal modulation takes different forms depending on the atlas creation strategy:

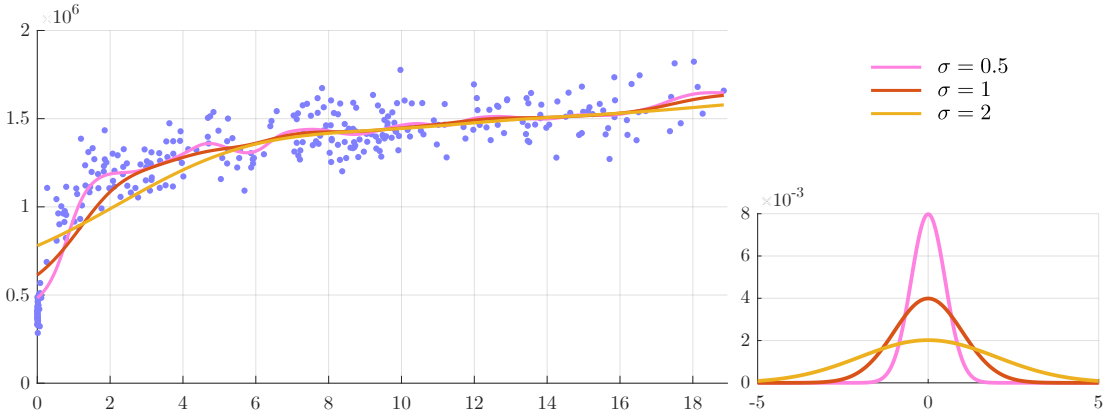

Figure 4.6: Gaussian kernel regression on brain volumes (in mm^3) as a function of the age (in years). Data from ASLpedia [ASLpedia], C-MIND [C-MIND] and the Developing Human Connectome Project (dHCP) [dHCP].

- For the template-based and the exhaustive pairwise approach, the weighting takes place at the level of the averaging that takes place on the images and the transformations.

  In [Ericsson 2008], 575 adult subjects are used to create a 4D atlas through a template-based strategy only taking into account local deformations.

  In [Schuh 2015], the exhaustive pairwise strategy is used while taking advantage of the SVF framework tools to produce a spatio-temporal atlas from 118 neonates for different timepoints between 28 and 44 gestational weeks.

  For both, regression over time was performed using a Gaussian kernel.

- For the groupwise registration, the weighting process is directly included into the cost function terms, but also at the final step when transformed images are averaged.

  In [Gholipour 2017], a fetal spatio-temporal atlas using such a technique has been built, also using a Gaussian kernel. It covers a period between 19 and 38 gestational weeks, the result is shown in 4.5.

Thus, each 3D sub-atlas is constructed through a regression process over the temporal domain both on the transformation space and the image intensities. If the spatio-temporal atlas aims at accounting for developmental growth, atlases only unbiased up to an affine transformation are not sufficient, both global size changes and local deformations between the brains have to be taken care of.

We saw that all the above-mentioned atlasing methods are ultimately a mapping of the images into a common space followed by an averaging of the transformed images. The weighting process will shift that common space closer to the ones with higher weights while also giving them more influence on the intensity of the final image.

4.4.2 Growth model

In the case of a longitudinal dataset i.e. the population has undergone observations repeatedly over time, one can extract more comprehensive developmental information.

In [Durrleman 2009, Durrleman 2013], it is proposed to estimate a regression model for the evolution of each subject. This consists in finding a diffeomorphic path transporting over time a baseline image (actually a shape in the above-mentioned papers) of a subject minimizing the sum of the distances to the other images of the same subject taken at different times. This allows notably to compare two subjects at a given time even though they is no observation at

that time. One can then perform a spatio-temporal registration of the evolution trajectories of the subjects to estimate a mean evolution scenario which is essentially a spatio-temporal atlas.

In the same vein, [Liao 2012] proposed a framework also including the estimation of an evolution model for each subject. It is followed by an iterative procedure of estimating transformations to map from the subjects to the atlas space through groupwise registration, construction of a sub-atlas for each timepoint using kernel regression and estimation of the atlas evolution model.

Those methods present the advantage of accounting not only for population information but also for subject-specific longitudinal specificities.

4.5 Conclusion

This chapter is far from an exhaustive review about atlas creation methods but was rather made as an introduction to them. In the following, it is the template-based approach inspired by [Guimond 2000] that will be mainly adopted because of its easy implementation and moderate computational cost (growing linearly with the number of images). A spatio-temporal extension is developed in Chapter 8 with a special weight function. The latter is notably used for the studies in Chapters 5 and 6. Finally, an iterative centroid approach, quite distinctive to the above-mentioned methods is introduced in Chapter 9.

Part II

Contributions in pediatric image analysis

Chapter 5

Directional brain expansion through anisotropic similarity registration

Contents

We propose in this chapter a novel method to quantify brain growth in 3 arbitrary orthogonal directions of the brain or its sub-regions through linear registration. This is achieved by introducing a 9 degrees of freedom (dof) transformation called anisotropic similarity which is an affine transformation with constrained scaling directions along arbitrarily chosen orthogonal vectors. This gives the opportunity to extract scaling factors describing brain growth along those directions by registering a database of subjects onto a common reference. This information about directional growth brings insights that are not usually available in longitudinal volumetric analysis. The interest of this method is illustrated by studying the anisotropic regional and global brain development of 308 healthy subjects betwen 0 and 19 years old. A gender comparison of those scaling factors is also performed for four age-intervals. We demonstrate through these applications the stability of the method to the chosen reference and its ability to highlight growth differences accros regions and gender.

5.1 Introduction

In pediatric image analysis, the study of brain development provides insights in the normal trend of brain evolution and enables early detection of abnormalities. Many types of morphometric measurements based on structural images have been explored and have shown their reliability as biomarkers in clinical use as established in [Dubois 2019, Giorgio 2013, Durazzo 2011,

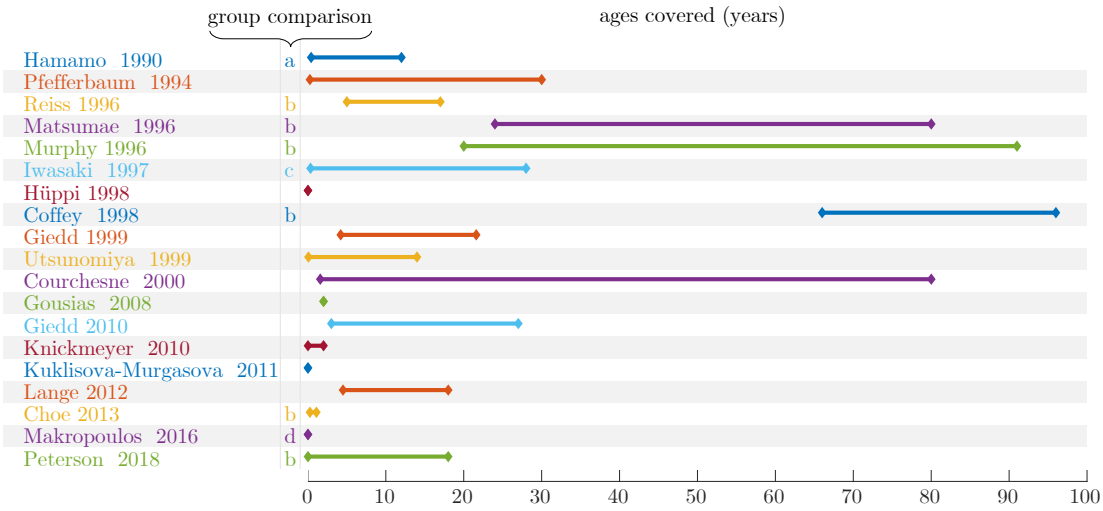

Figure 5.1: Ages covered by different brain volumetric studies, group comparison between: a - normal / mental retardation, b - male / female, c - normal / motor disturbances, d - normal / premature.

Frisoni 2010, Novak 2009, Tosun 2015]. Evaluated on a database of subjects covering a period of interest, it allows to better model the brain development and to highlight changes in growth, shape, structure, etc. Those measurements can be conducted on geometrical objects of different dimensions. Unidimensional ones such as the bicaudate ratio (minimum intercaudate distance divided by brain width along the same line) have been explored in [Aylward 1991] and [Bermel 2002] but also biparietal, bifrontal and transverse cerebellar diameters in [Nguyen The Tich 2011]. Surface-based quantities such as cortical surface area in [Winkler 2012], corpus callosum mid-sagittal area in [Giedd 2010] or cortical folding metrics as in [Lefèvre 2016] have also been studied. However, the vast majority of studies are based on 3D features through the assessment of region of interest (ROI) volumes. Volumetric measures of different regions of the brain have been considered for specific ages or various temporal ranges. A far from exhaustive list is presented in Figure 5.1. Studied regions are very heterogeneous from large areas such as the whole brain itself, cerebellum, lobes or partitions of those to smaller ones such as basal ganglia, hippocampus, thalamus sometimes even separated according to the composition of their tissues (white matter (WM), gray matter (GM), cerebro-spinal fluid (CSF)). Some group comparisons have also been performed mostly between male and female or between preterm and term newborns.

Morphometric measurements can be determined manually. However, this requires the intervention of a medical expert able to select specific landmarks or perform segmentation. These tasks are highly time consuming with a potentially large inter-expert variability. Advances in computational medical imaging allow nowadays the use of semi-automated (requiring some human intervention) or fully-automated techniques. They involve algorithms able to automatically perform operations such as registration and segmentation.

A major drawback of purely volumetric measurements is that they do not provide any information on the shape of the regions or about the anisotropy of their development. In this chapter, a new method is proposed that aims at quantifying global and regional brain growth in three arbitrary orthogonal directions of the brain (or ROI) through linear registration. To do so, a transformation called anisotropic similarity introduced in Section 2.2.4 is used. It is an affine transformation with scaling directions constrained by orthogonal vectors arbitrarily chosen. A method to estimate, in a 3 dimensional space, the optimal anisotropic similarity for the least squares problem of distances between two sets of paired points is presented in section 5.3. Those results will then be used to create a registration algorithm based on this transformation. By

registering a database of subjects onto a common basis (i.e. an atlas segmented in different ROIs) using anisotropic similarity, we have the opportunity to extract global or regional scaling ratios for all those subjects along arbitrary chosen orthogonal directions.

A direct application is, using the pipeline exposed in section 5.4, the exploration of regional scaling ratios growth charts along three fixed orthogonal directions through the ages highlighting anisotropic brain development. Resulting curves for whole brain and ROIs (lobes, basal ganglias, cerebellum...) are presented in section 5.5.2. A comparison of scaling factors from males and females is performed for four different age-intervals between 0 and 19 years old in section 5.5.3. Finally, the influence of the common reference image on the resulting scaling factors is studied in section 5.5.5.

Anisotropic similarity registration algorithm as well as other image processing tools used in this work are publicly available in Anima [Anima].

5.2 Generalities about linear registration

As seen in Section 3.2.1, in block matching registration algorithms, two steps are iterated:

1. Matching: for a set of blocks established in the reference image, homologous blocks best satisfying a similarity criterion are searched in the moving image.

2. Aggregation into a global transformation: an optimization is performed in order to find the global transformation minimizing a distance between the sets of blocks and is then applied to the moving image.

In order to perform an anisotropic similarity registration using this kind of approach, the first step (matching) is performed the same way it would be for any regular linear transformation. It outputs two sets of paired points: x and y that are the centers of the homologous blocks. The second step (aggregation onto a global transformation) however is dependent on the type of linear transformation we want to determine so an adapted version for anisotropic similarity transformation is needed.

This optimization step consists in finding, in the set of anisotropic similarity transformations, the one that best maps x onto y. Let $x = \{x_1, \dots, x_M\}$ and $y = \{y_1, \dots, y_M\}$ be two sets of M paired points coming from the matching step.

Let $x'_i = x_i - \bar{x}$ and $y'_i = y_i - \bar{y}$ be the barycentric coordinates. Since $\hat{t}$ can be directly expressed from $\hat{A}$, the problem can then be simplified as the minimization of:

$$C(A) = \sum_i \|y'_i - Ax'_i\|^2 \tag{5.1}$$

5.3 Optimal anisotropic similarity between two sets of paired points

We define a new type of affine transformation, hereafter named **anisotropic similarity**, which has constrained directions of scaling. Using the RSD decomposition depicted in Section 2.2.3.1, an affine transformation matrix can be written PSU^T where P and U are rotation matrices and S is diagonal. In case of an anisotropic similarity transformation, the matrix U is imposed to be fixed, arbitrary chosen. This type of transformation is composed of a rotation, an anisotropic scaling which is directed by another fixed rotation matrix and a translation leading to a linear part of form: $A = PSU^T$ with U fixed. The Table 2.1 can therefore be completed with the row for anisotropic similarity presented in Table 5.1.

To our knowledge, the optimization procedure in the case of anisotropic similarities has not been considered in the literature. We thus present a method to find the optimal anisotropic similarity between two sets of paired points. Similarly to the rigid case by [Horn 1987] and

Transformation	Degrees of freedom	
Anisotropic similarity	9	▷ an anisotropic scaling (3 dof): S ▷ a rotation (3 dof): P ▷ a translation (3 dof): t

Table 5.1: Anisotropic similarity transformation and its degrees of freedom

[Pennec 1996], unit quaternions are used as a representation of spatial rotations. The optimization over variable A therefore becomes an optimization over variables P and S:

$$C(P,S) = \sum_i \left\| y'_i - PSU^T x'_i \right\|^2 \tag{5.2}$$

Let $\tilde{x}_i = U^T x'_i$ and $\xi_i = S\tilde{x}_i$:

$$C(P,S) = \sum_i \| y'_i - P\xi_i \|^2 \tag{5.3}$$

As seen in Section 2.2.2.3, the rotation induced by the matrix P can be expressed using unit quaternions. Similarly to [Horn 1987] and [Pennec 1996], the problem then becomes:

$$\tilde{C}(q,S) = \sum_i ||(0,y'_i) * q - q * (0,\xi_i)||^2 \tag{5.4}$$

Where q is a unit quaternion and $*$ is the quaternion multiplication. Let p and q be quaternions, $\bar{p}$ and $\bar{q}$ their conjugated quaternions respectively. There is a representation where the quaternion product can be expressed as a matrix product (see Section 2.2.2.2). The left and right multiplication matrix L and R associated to p and q are defined such that: $L_p q = R_q p = p * q$.

Since $(0,y'_i)$ and $(0,\xi_i)$ are pure quaternions, their associated multiplications matrices are skew-symmetric. We have $(0,y'_i) * q = L_{y'_i} q$ and $-q * (0,\xi_i) = -R_{\xi_i} q = R^T_{\xi_i} q$. Thus, we obtain the following criterion (see Appendix B.2 for detailed calculations):

$$\tilde{C}(q,S) = q^T \left(-\sum_i \left(L_{y'_i} + R^T_{\xi_i} \right)^2 \right) q \tag{5.5}$$

For further computation, we denote $B_i = -\left(L_{y'_i} + R^T_{\xi_i} \right)^2$ and $B = \sum_i B_i$. A lagrangian with unit constraint $q^T q = 1$ has then to be added to ensure a unit quaternion:

$$\Lambda = q^T B q - \lambda (q^T q - 1) \tag{5.6}$$

Let $s_j = S_{jj}$. The derivatives of this new formulation can then be written as:

$$\begin{cases} \dfrac{\partial \Lambda}{\partial q} &= (B - \lambda I_4) q \\ \dfrac{\partial \Lambda}{\partial s_j} &= -q^T \left(\sum_i L_{y'_i} \dfrac{\partial R^T_{\xi_i}}{\partial s_j} \right) q + s_j \sum_i \tilde{x}^2_{ji} \end{cases} \tag{5.7}$$

Derivative with respect to q depends upon s_j and vice versa. Therefore, a direct solution to the problem of minimizing $\tilde{C}(q,S)$ is difficult to find if not impossible. However, separating the problem between S and q leads to an alternate optimization scheme, each having an analytical solution.

Rotation:

$$\frac{\partial \Lambda}{\partial q} = 0 \Leftrightarrow (B - \lambda I_4) q = 0 \tag{5.8}$$

Solving this equation amounts finding the eigen vectors of B. More precisely, the global minimum $\hat{q}$ is the one associated to the smallest eigen value of B as shown in [Horn 1987, Pennec 1996].
Scaling: (see Appendix B.3)

$$\frac{\partial \Lambda}{\partial s_j} = 0 \Leftrightarrow \hat{s}_j = \frac{1}{\sum_i \tilde{x}_{ji}^2} q^T \left(\sum_i L_{y'_i} \frac{\partial R_{\xi_i}^T}{\partial s_j} \right) q \tag{5.9}$$

Now, interestingly the matrices $L_{y'_i} \dfrac{\partial R_{\xi_i}^T}{\partial s_j}$ have a quite trivial form. They are all symmetric, only the placing and indexes change (see Appendix B.4). We finally get the following iterative alternate optimization scheme:

- For a fixed value of $\hat{S}$, estimate the new optimal rotation quaternion: $\hat{q}$ as the eigenvector with the smallest eigenvalue of B
- For a fixed value of $\hat{q}$, estimate the new optimal scaling matrix $\hat{S} = \text{Diag}(\hat{s}_1, \hat{s}_2, \hat{s}_3)$ following:

$$\hat{s}_j = \frac{1}{\sum_i \tilde{x}_{ji}^2} \hat{q}^T \left(\sum_i L_{y'_i} \frac{\partial R_{\xi_i}^T}{\partial s_j} \right) \hat{q} \tag{5.10}$$

5.4 Material and methods

In the previous section, a method to find the optimal anisotropic similarity between two sets of paired points has been depicted. This gives the opportunity to register a database of subjects onto a common reference image using this type of linear transformation to extract scaling factors along chosen orthogonal directions and to study the variation of these factors on different ROIs between populations or among normal subjects.

5.4.1 Material

308 T1-weighted images of healthy subjects between 0 and 19 years old have been used, coming from three different studies: ASLpedia [ASLpedia], C-MIND [C-MIND] and the Developing Human Connectome Project (dHCP) [dHCP]. Details on age repartition among databases and on image characteristics are given in Figure 5.2.

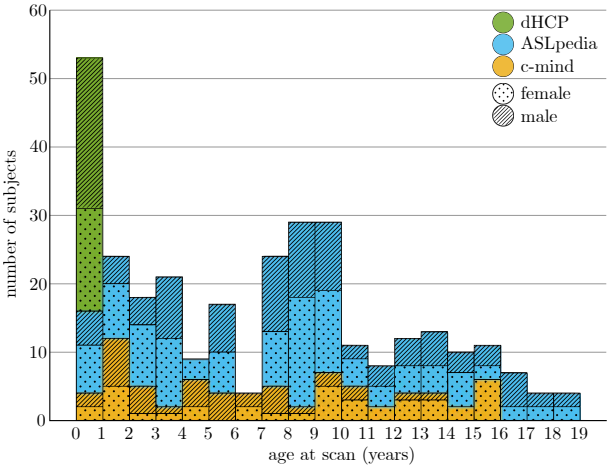

Study	dHCP	c-mind	ASLpedia
Voxel size (mm) (axial, coronal, sagittal)	0.5x0.5x0.5	1x1x1	0.5x0.5x1
Number of subjects selected	37	197	74
Age range of subjects (years)	<0.1	[0, 19]	[0, 16]

Figure 5.2: Repartition of the subjects selected from three studies over age

5.4.2 Methods

We have developed a pipeline composed of 5 steps to extract scaling factors for 3 orthogonal directions on ROIs from a database of subjects:

1. Choice and construction of the common reference image,
2. Segmentation of the common reference image into different ROIs,
3. Choice of the constrained directions of scaling for the anisotropic similarity registration,
4. Anisotropic similarity registration of a database of subjects to each ROIs of the common reference image to extract relative scaling factors,
5. Renormalization of the relative scaling factors to obtain absolute scaling factors.

The above numbers associated to the steps are also associated to the subsections numbering below and to the numbers in Figure 5.3.

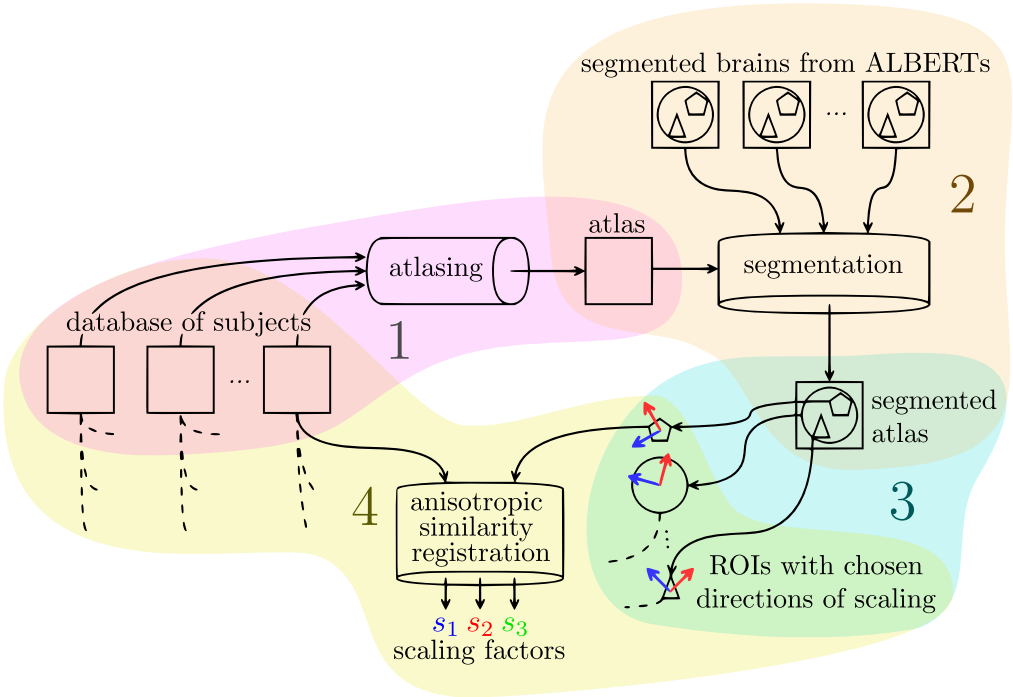

Figure 5.3: Pipeline for the extraction of scaling factors of a database of subjects using anisotropic similarity registration onto an atlas based on them as common reference image.

5.4.2.1 Creation of the common reference image

For genericity, the common reference image has been chosen to be an atlas made from all the subjects using a modified version of the atlas creation algorithm from [Guimond 2000]. Our method, developed in [Legouhy 2019] and detailed in Chapter 8 produces atlases up to a rigid transformation thus accounting for both global growth and local deformations. Also it includes mechanisms conceived to improve the robustness of the registration algorithms in case of brains of different sizes through adapted initialization and linear transformation decompositions.

5.4.2.2 Segmentation of the common reference image

The atlas has then been segmented into 21 regions of interest (ROIs): whole brain, hemispheres, frontal lobe, parietal lobe, temporal lobe, occipital lobe, basal ganglias, cerebellum, insulas, ventricles, corpus callusum and brainstem. All structures were also separated in their left and right sides. To do this segmentation, ALBERTs [ALBERTs] manual ones have been used: 20 brains segmented into 50 regions manually drawn based on MRI brain scans that we fused to obtain the wider desired regions. The T1-weighted images of those brains have been registered onto our atlas through affine then diffeomorphic registration. The outputs have then been used to transfer all the segmentations onto our atlas which have been then merged using majority voting following [Heckemann 2006]. The segmented atlas is shown in Figure 5.4. It should be noted that the 20 brains associated to ALBERTs data were only used for segmentation of the ROIs. They were not used for the creation of the common reference and, not used either as subjects registered with anisotropic similarity.

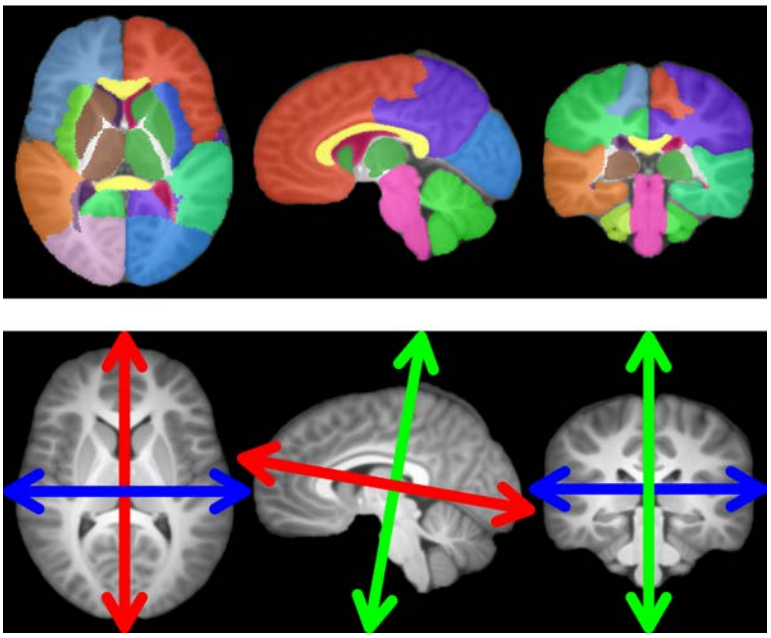

ROI	ID	color
whole brain	0	
left hemisphere	01	
right hemisphere	02	
left temporal	1	
right temporal	2	
left parietal	3	
right parietal	4	
left frontal	5	
right frontal	6	
left cerebellum	7	
right cerebellum	8	
left occipital	9	
right occipital	10	
left basal ganglia	11	
right basal ganglia	12	
left insula	13	
right insula	14	
left ventricule	15	
right ventricule	16	
corpus callossum	17	
brainstem	18	

direction	ID	color
orthogonal to the sagittal plane	1	
principal direction of voxels positions projected on sagittal plane	2	
secondary direction of voxels positions projected on sagittal plane	3	

Figure 5.4: Regions of interest (ROIs) segmented and represented on the common reference image (top), chosen directions of scaling for anisotropic similarity registration defined and represented on the common reference image (bottom).

5.4.2.3 Choice of the constrained directions of scaling

The fixed scaling directions (characterized by the column vectors of the matrix U) are chosen on the reference image such that the first direction (blue in Figure 5.4) is orthogonal to the mid-sagittal plane (determined using [Prima 2002]) for symmetry reasons. The other two di-

rections are set using principal component analysis (PCA) on the non zero voxels coordinates projected onto the mid-sagittal plane. The second direction (red in Figure 5.4) corresponds to the principal direction from the PCA while the third (green in Figure 5.4) corresponds to the secondary one. Three orthogonal directions are now chosen: one through iconic considerations and the other two based on purely geometrical features. In our application, the matrix U is the same for all ROIs of the reference image and is defined using the whole brain. However, it is possible to define a different U for each ROI independently. Chosen directions of scaling are shown in Figure 5.4.

These directions have been chosen as a proof of concept. Depending on the purpose of the study, other choice may appear more relevant (see discussion Section 5.6).

5.4.2.4 Anisotropic similarity registration

For each ROI, all subjects undergo an anisotropic similarity registration onto the reference image masked by this ROI. This registration is performed in two steps using in each case our block matching algorithm implemented in Anima [Anima]:

1. A similarity T_B from whole brain subjects onto whole brain common reference is first estimated.
2. An anisotropic similarity T_C initialized from the previous step output is then computed to bring the subjects onto the atlas masked by the current ROI.

The first transformation, a similarity, is computed indirectly during a process of affine registration using the method depicted in Section 7. Let A be the linear part of an affine transformation T_A. We consider the following SVD: $A = VDW^T$ with D diagonal positive, V and W unitary matrices. We define T_B (the nearest similarity associated to T_A) as the transformation with linear part $B = \bar{d}VW^T$ with $\bar{d}$ being the average of the singular values namely the mean of the diagonal of D, and translation part $t = \bar{y} - B\bar{x}$. We chose the initialization to be a similarity since the composition of a similarity T_B and an anisotropic similarity T_C associated to a matrix U is still an anisotropic similarity associated to the same U: $T_BT_C = (s_BR_B)(R_CS_CU^T) = (R_BR_C)(s_BS_C)U^T = RSU^T$. The whole registration process is summarized in Figure 5.5.

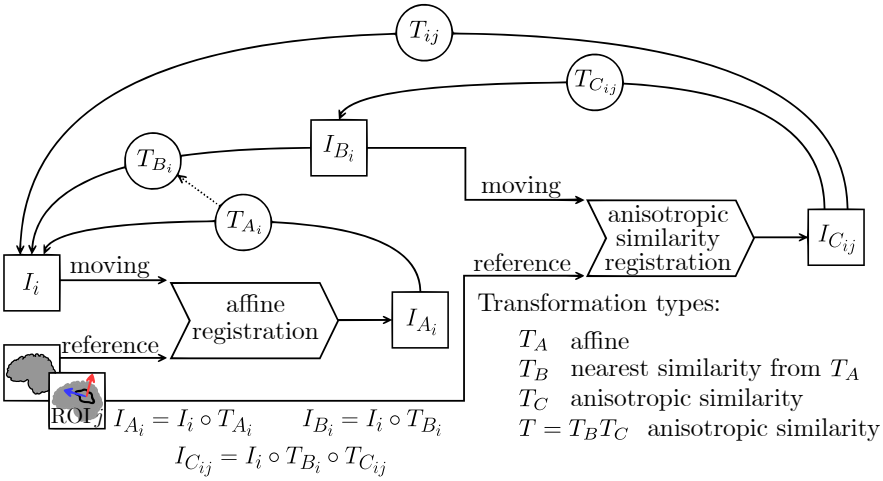

Figure 5.5: Two steps registration process: first an affine from which a nearest similarity is deduced, then an anisotropic similarity. Transformations are composed and represented with arrows from destination to start since the interpolations occurring in the resampling are done using the backward mapping. The inverse transformation is actually used on each voxel of the output images to determine the position in the input image from which a value is sampled.

5.4.2.5 Extraction of absolute scaling factors

From the output transformations of the registration step, the relative scaling parameters along the three fixed directions are extracted. Those scaling factors are relative to the reference image. We want to normalize them such that they become about equal to 1 at birth and represent, for other ages, how much a region expanded along the chosen directions since birth. To this end, the fact that all dHCP subjects are very young (less than 1 month) is exploited. The normalization step consist in dividing the relative scaling factors of all the dataset by the average of the ones associated to the dHCP subjects considered as the "root" of the brain expansion. Those new scaling factors will now be considered as absolute scaling factors. At this stage, for each subject, an absolute scaling factor has been determined for each ROI. Those absolute scaling factors are used to model the expansion of the brain toward the chosen directions.

5.5 Experiments and results

5.5.1 Model selection

Several models are traditionally used to represent growth in biostatistics such as the exponential or Weibull models. The second one has been considered by [Peterson 2018] as the best suited to model brain growth in terms of volume. Our case however is different: it can be viewed as a 3-way unidimensional approach. In our quest to find the function best suited to model growth curves for our data, we decided to consider, as a prior, that the brain expansion is stopping at some point. Therefore, we restricted the spectrum to functions that have a horizontal asymptote at infinity. The selected candidates to model directional brain growth are the following:

- Rational with polynomials of degree 1 as numerator and denominator : $y = \dfrac{ax+b}{x+c}$
- Weibull: $y = a - be^{-cx^d}$
- Gompertz: $y = ae^{-be^{-cx}}$
- Exponential: $y = a + be^{-cx}$

For each candidate, the optimal coefficients are estimated through nonlinear regression using the Levenberg-Marquardt iterative weighted least squares algorithm from [Seber 1989]. In this process, weights are chosen to compensate for local gender repartition. For each subject i, a window of width $l = 2$ years centered on the subject age is considered. Let n_f, n_m and n be the number of female, male and total subjects respectively in that window. A correction coefficient $c_f = \dfrac{n_m}{n}$ is applied if i is a female and $c_m = \dfrac{n_f}{n}$ if i is a male. Let $\{y_1, \dots, y_n\}$ be the observations (i.e. here the obtained scaling factors), $\bar{y}$ be the average of those and $\{\hat{y}_1, \dots, \hat{y}_n\}$ be the fitted values.

Based on these statistics, the chosen candidate for the modeling will be the one that best satisfies a criterion quantifying the goodness of fit. This indicator should evaluate the accuracy of the model i.e. how close the model is to the observation while discouraging overfitting. It therefore consists in a tradeoff between accuracy and parsimony. It has been shown in [Spiess 2010] that the coefficient of determination is not, at least when considered alone, an appropriate measure for the goodness of fit in the case of nonlinear model selection. A more adapted goodness of fit for nonlinear model selection is the Akaike information criterion (AIC) developed in [Akaike 1974] and [Burnham 2002]. Based on information theory, it proposes to estimate the information loss induced by each candidate model to represent an unknown process that supposedly generated the data as shown in [Burnham 2004]. This is made possible through the estimation of the Kullback-Leibler divergence related to the maximized log-likelihood. AIC is defined by: $AIC = -2p - 2\ln(\hat{L})$, where $\hat{L}$ is the maximum likelihood of the candidate

model and the first term penalizes a large number of parameters p. Therefore, the preferred model among the candidates is the one with the lower AIC. Note that AIC of a model taken alone is meaningless, it makes sense only when compared to the one of the other models. This is why it is recommended to consider it along with another statistic that quantifies the error between the model and the data like mean of squared errors (MSE): $MSE = \frac{1}{n}\sum_i (y_i - \hat{y}_i)^2$ which is the average of the residuals. A corrected version of the AIC has been developed to avoid overfitting in the case of small sample sizes: $AIC_c = AIC + \frac{2p(2p+1)}{n-p-1}$. To facilitate the interpretation that can be quite obscure using raw AIC, following [Wagenmakers 2004], it is possible to transform those values into conditional probabilities for each model called Akaike weights. Defined for each model i by $w_{i,AIC} = \frac{e^{-\frac{1}{2}(AIC_i - AIC_{min})}}{\sum_j e^{-\frac{1}{2}(AIC_j - AIC_{min})}}$, those weights represent the probability for each candidate i to be the best suited in the sense of AIC to model the data among all the candidates.

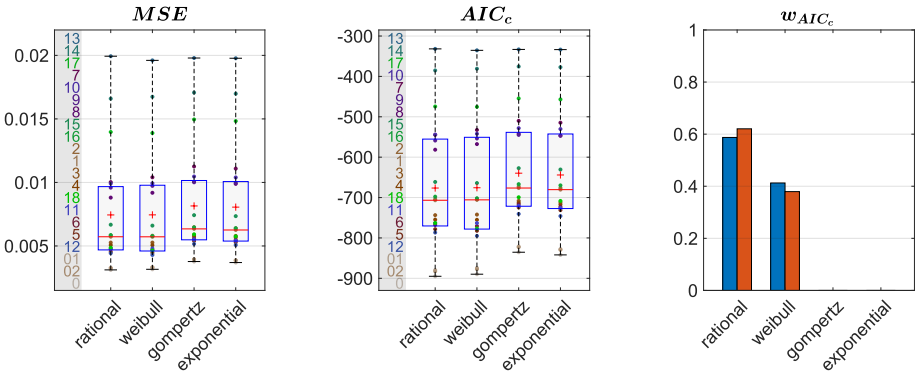

Figure 5.6: Goodness of fits for each candidate to model the ouputed scaling factors averaged in the 3 directions. Boxplots are performed along the ROIs, ROI IDs are displayed on the left. Akaike weights are computed on mean (blue) and median (red) AIC_c

All the goodness of fit depicted above as well as MSE have been evaluated for each of our candidates to model the scaling factors for each ROI. We present the results of this evaluation in Figure 5.6. The Gompertz and exponential models are largely below the other two. Even though the Weibull model behaves relatively well, the rational one shows better scores whatever the tested goodness of fit.

5.5.2 Directional growth curves

From the previous sections, scaling factors in each direction for each ROI are now modeled using a rational function with polynomials of degree 1 as numerator and denominator chosen after model selection. Results for all regions studied are presented in Figure 5.7. The method presented by [Lane 1994] is used to compute simultaneous 99% confidence intervals for fitted values. The black curve represents the average brain growth computed as the mean of the directional models (Figure 5.7).

Those curves exhibit various characteristics of the developments of those different ROIs. Firstly, the pace: some regions grow at a relatively slow pace like the frontal lobes which also to still expand after 16 years old. In the other hand, some parts of the brain show a steeper pace like the occipital lobes that show a quick growth until about 3 years old followed by an early stagnation. Secondly, the amplitude: some regions grow up to a higher asymptote than other. The cerebellum for example expands in average along the 3 directions up to 1.8 times its initial size while the parietal lobe barely reach 1.5 times its initial size. And thirdly, the main advantage of our method compared to classic volumetry, the anisotropy: some parts of

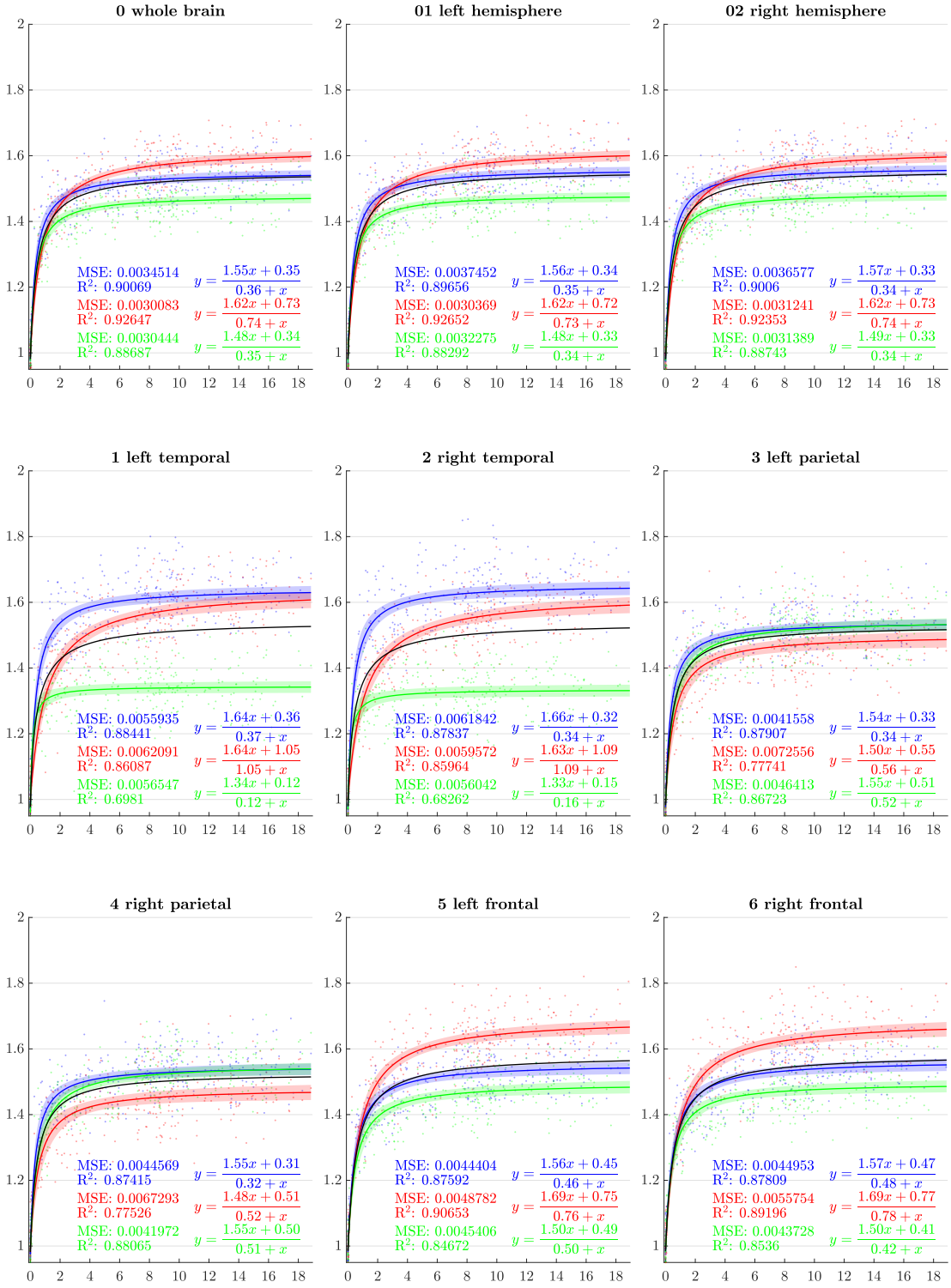
0 whole brain
MSE: 0.0034514
R²: 0.90069
y = (1.55x + 0.35)/(0.36 + x)
MSE: 0.0030083
R²: 0.92647
y = (1.62x + 0.73)/(0.74 + x)
MSE: 0.0030444
R²: 0.88687
y = (1.48x + 0.34)/(0.35 + x)
01 left hemisphere
MSE: 0.0037452
R²: 0.89656
y = (1.56x + 0.34)/(0.35 + x)
MSE: 0.0030369
R²: 0.92652
y = (1.62x + 0.72)/(0.73 + x)
MSE: 0.0032275
R²: 0.88292
y = (1.48x + 0.33)/(0.34 + x)
02 right hemisphere
MSE: 0.0036577
R²: 0.9006
y = (1.57x + 0.33)/(0.34 + x)
MSE: 0.0031241
R²: 0.92353
y = (1.62x + 0.73)/(0.74 + x)
MSE: 0.0031389
R²: 0.88743
y = (1.49x + 0.33)/(0.34 + x)
1 left temporal
MSE: 0.0055935
R²: 0.88441
y = (1.64x + 0.36)/(0.37 + x)
MSE: 0.0062091
R²: 0.86087
y = (1.64x + 1.05)/(1.05 + x)
MSE: 0.0056547
R²: 0.6981
y = (1.34x + 0.12)/(0.12 + x)
2 right temporal
MSE: 0.0061842
R²: 0.87837
y = (1.66x + 0.32)/(0.34 + x)
MSE: 0.0059572
R²: 0.85964
y = (1.63x + 1.09)/(1.09 + x)
MSE: 0.0056042
R²: 0.68262
y = (1.33x + 0.15)/(0.16 + x)
3 left parietal
MSE: 0.0041558
R²: 0.87907
y = (1.54x + 0.33)/(0.34 + x)
MSE: 0.0072556
R²: 0.77741
y = (1.50x + 0.55)/(0.56 + x)
MSE: 0.0046413
R²: 0.86723
y = (1.55x + 0.51)/(0.52 + x)
4 right parietal
MSE: 0.0044569
R²: 0.87415
y = (1.55x + 0.31)/(0.32 + x)
MSE: 0.0067293
R²: 0.77526
y = (1.48x + 0.51)/(0.52 + x)
MSE: 0.0041972
R²: 0.88065
y = (1.55x + 0.50)/(0.51 + x)
5 left frontal
MSE: 0.0044404
R²: 0.87592
y = (1.56x + 0.45)/(0.46 + x)
MSE: 0.0048782
R²: 0.90653
y = (1.69x + 0.75)/(0.76 + x)
MSE: 0.0045406
R²: 0.84672
y = (1.50x + 0.49)/(0.50 + x)
6 right frontal
MSE: 0.0044953
R²: 0.87809
y = (1.57x + 0.47)/(0.48 + x)
MSE: 0.0055754
R²: 0.89196
y = (1.69x + 0.77)/(0.78 + x)
MSE: 0.0043728
R²: 0.8536
y = (1.50x + 0.41)/(0.42 + x)

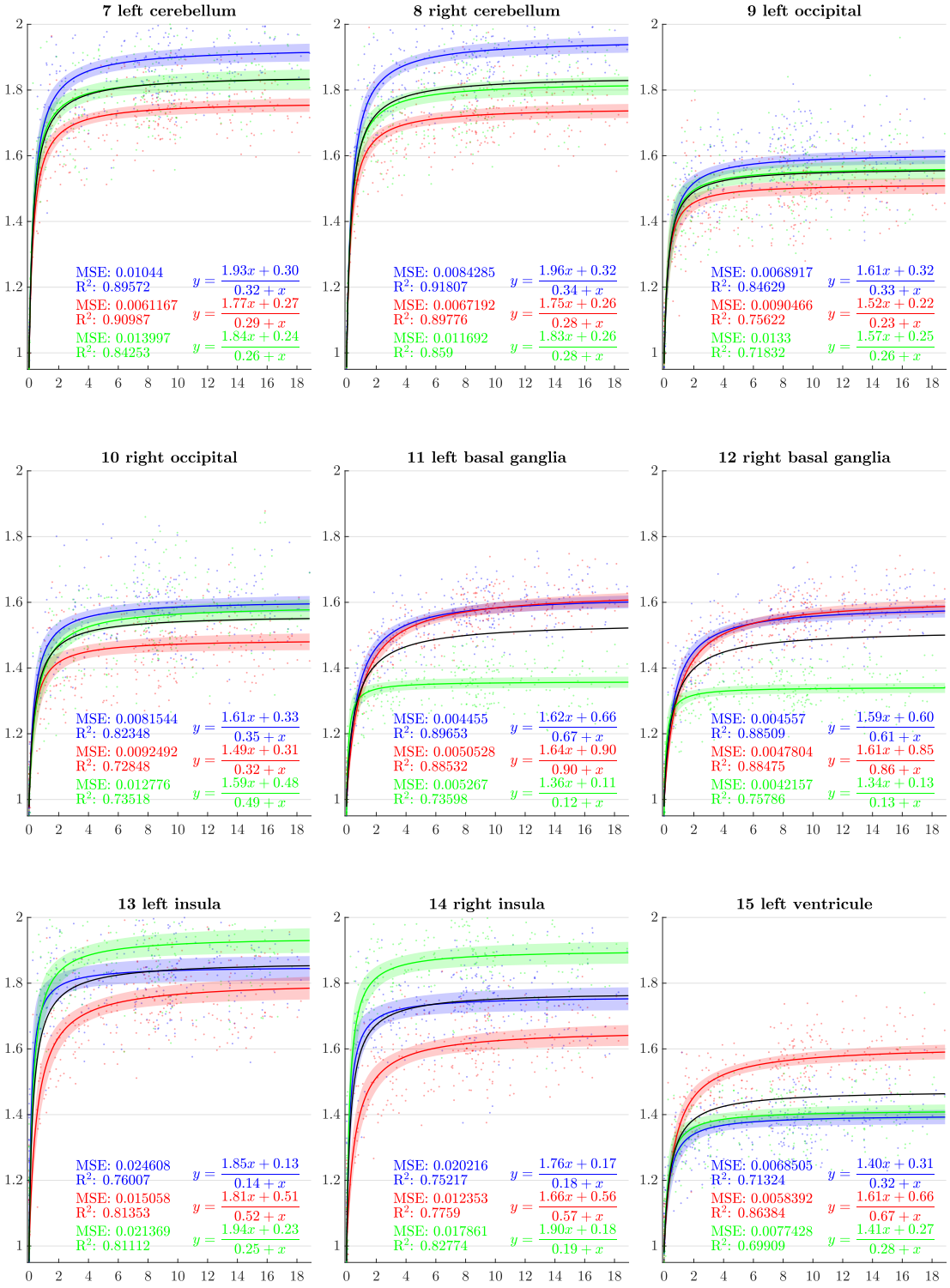
7 left cerebellum
MSE: 0.01044
R²: 0.89572
y = (1.93x + 0.30)/(0.32 + x)
MSE: 0.0061167
R²: 0.90987
y = (1.77x + 0.27)/(0.29 + x)
MSE: 0.013997
R²: 0.84253
y = (1.84x + 0.24)/(0.26 + x)
8 right cerebellum
MSE: 0.0084285
R²: 0.91807
y = (1.96x + 0.32)/(0.34 + x)
MSE: 0.0067192
R²: 0.89776
y = (1.75x + 0.26)/(0.28 + x)
MSE: 0.011692
R²: 0.859
y = (1.83x + 0.26)/(0.28 + x)
9 left occipital
MSE: 0.0068917
R²: 0.84629
y = (1.61x + 0.32)/(0.33 + x)
MSE: 0.0090466
R²: 0.75622
y = (1.52x + 0.22)/(0.23 + x)
MSE: 0.0133
R²: 0.71832
y = (1.57x + 0.25)/(0.26 + x)
10 right occipital
MSE: 0.0081544
R²: 0.82348
y = (1.61x + 0.33)/(0.35 + x)
MSE: 0.0092492
R²: 0.72848
y = (1.49x + 0.31)/(0.32 + x)
MSE: 0.012776
R²: 0.73518
y = (1.59x + 0.48)/(0.49 + x)
11 left basal ganglia
MSE: 0.004455
R²: 0.89653
y = (1.62x + 0.66)/(0.67 + x)
MSE: 0.0050528
R²: 0.88532
y = (1.64x + 0.90)/(0.90 + x)
MSE: 0.005267
R²: 0.73598
y = (1.36x + 0.11)/(0.12 + x)
12 right basal ganglia
MSE: 0.004557
R²: 0.88509
y = (1.59x + 0.60)/(0.61 + x)
MSE: 0.0047804
R²: 0.88475
y = (1.61x + 0.85)/(0.86 + x)
MSE: 0.0042157
R²: 0.75786
y = (1.34x + 0.13)/(0.13 + x)
13 left insula
MSE: 0.024608
R²: 0.76007
y = (1.85x + 0.13)/(0.14 + x)
MSE: 0.015058
R²: 0.81353
y = (1.81x + 0.51)/(0.52 + x)
MSE: 0.021369
R²: 0.81112
y = (1.94x + 0.23)/(0.25 + x)
14 right insula
MSE: 0.020216
R²: 0.75217
y = (1.76x + 0.17)/(0.18 + x)
MSE: 0.012353
R²: 0.7759
y = (1.66x + 0.56)/(0.57 + x)
MSE: 0.017861
R²: 0.82774
y = (1.90x + 0.18)/(0.19 + x)
15 left ventricule
MSE: 0.0068505
R²: 0.71324
y = (1.40x + 0.31)/(0.32 + x)
MSE: 0.0058392
R²: 0.86384
y = (1.61x + 0.66)/(0.67 + x)
MSE: 0.0077428
R²: 0.69909
y = (1.41x + 0.27)/(0.28 + x)

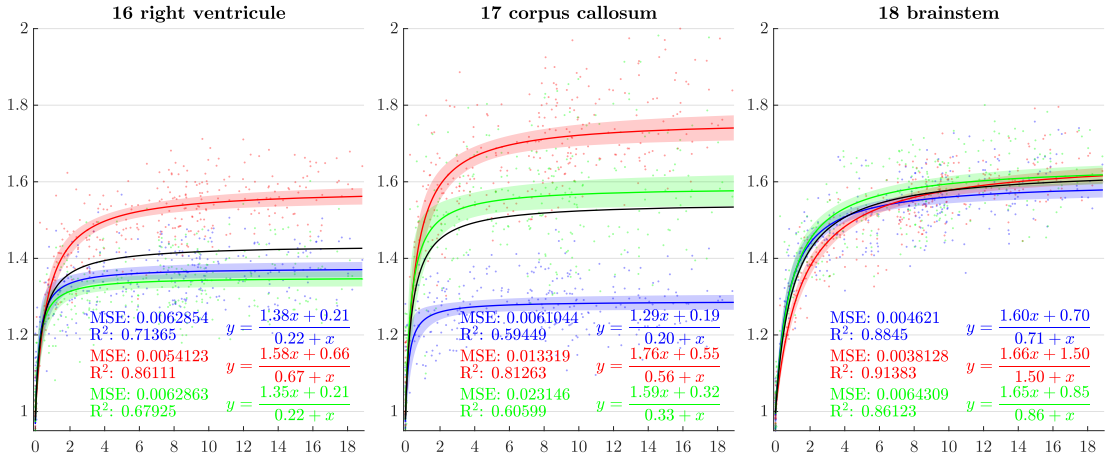

Figure 5.7: Resulting scaling factors as a function of the age in years for different ROIs, along direction 1 (blue), 2 (red), 3 (green). Fitted using rational model together with 99% confidence intervals for fitted values. Black curves represent the average models along the three directions.

the brain evolve quite isotropically such as parietal lobes while other have a very anisotropic expansion like the temporal lobes that expand way less in the third direction (green) compared to the other two.

5.5.3 Male vs female comparison

Gender, like age, is a characteristic of the subjects available in all the studies we considered. The aim of this section is to evaluate if differences in terms of scaling factor can be found between genders. We divided our data into four age-intervals based on the age of the subjects. The first one contains dHCP participants (newborns), the second one is composed of all non-newborn subjects between 0 and 6 years old, the third one between 6 and 12 and the fourth older to 12. Repartition of the subjects in terms of gender, age class and study is shown in Table 5.2.

		dHCP		$(0, 6]$		$(6, 12]$		> 12		
	dHCP		22		0		0		0	
male	c-mind	22	0	51	29	48	37	26	24	147
	ASLpedia		0		22		11		2	
	dHCP		15		0		0		0	
female	c-mind	15	0	54	43	57	43	35	21	161
	ASLpedia		0		11		14		14	
		37		105		105		61		308

Table 5.2: Repartition of the subjects in term of age class, gender and study

For each of these age-intervals, and each of the chosen scaling directions, and each ROI, we performed a test to evaluate if the scaling factors for male subjects are greater than scaling factors for female subjects. Since these data are not normally distributed in those subdivisions, we used two-tailed Wilcoxon-Man-Whitney U-tests. For each of those tests, the null hypothesis H_0 is the following: the distributions of the scaling factors between males and females are equal, while the alternative hypothesis H_1 states: the distributions of males and females are different. We performed 252 tests in total: 4 age-intervals $\times$ 21 ROIs $\times$ 3 directions whose results are shown in Figure 5.8.

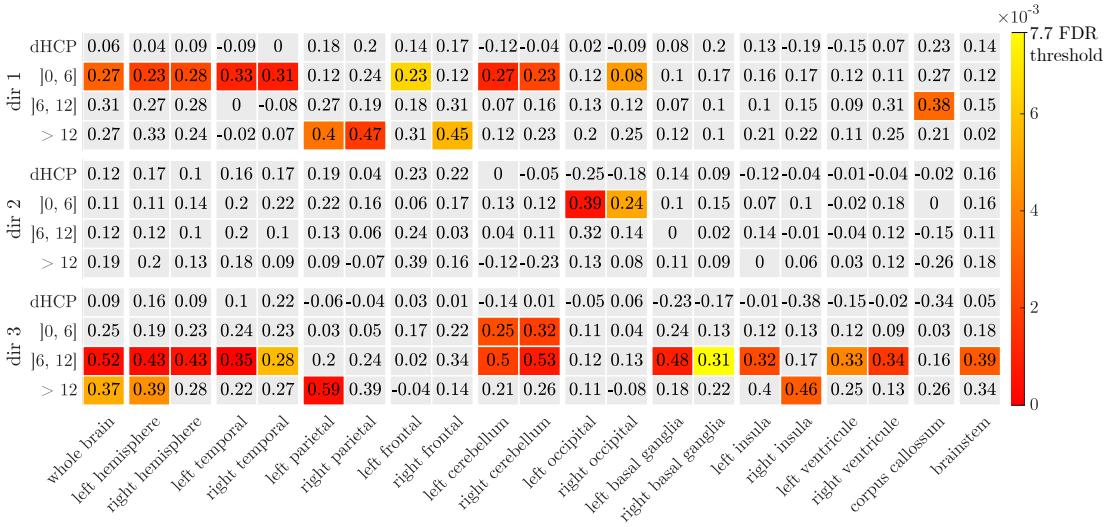

Figure 5.8: Male vs female comparison using Wilcoxon-Man-Whitney U-test and H_0: the distribution of the scaling factors of males and females are equal, H_1: the distributions of males and females are different. In color: p-values for H_0 rejection for FDR at level 5% (Benjamini and Hochberg method). Numerically: the size of the effect d for each test.

A type 1 error, or false positive, occurs when H_0 is incorrectly rejected. Since we are doing multiple comparisons, rejecting H_0 based on the risk of type 1 error $\alpha = 5\%$, may lead in our case to an expected number of false positives greater than 12. Instead of using α, we therefore adopted the false discovery rate (FDR) that controls the proportion of false positives among the tests where H_0 has been rejected. Therefore, we stated the acceptance or rejection of H_0 based on a FDR at level 5%. This has been done using Benjamini and Hochberg procedure from [Benjamini 1995] and corresponds to reject H_0 when the p-value is less than 0.0077 (Figure 5.8). FDR has been preferred to family-wise error rate (FWER), that controls the risk of at least 1 false positive among the whole family of tests, because of the over-conservatism of this last type of procedure leading to poor test power (probability of correctly rejecting H_0). Additionally, we calculated and presented in Figure 5.8, for each test, the effect size d following:

$$d = \frac{\text{med}(\{S_m\}) - \text{med}(\{S_f\})}{\sigma(\{S_m\}) + \sigma(\{S_f\})} \tag{5.11}$$

Where $\{S_m\}$ (resp. $\{S_f\}$) is the set of scaling factor of males (resp. females) used for the test. We preferred the use of median instead of mean due to the fact that we do not know the distribution of the data a priori and we performed ranksum type tests.

For all the tests that lead to a rejection of the null hypothesis, scaling factors were higher for males both in terms of means and medians. Tests show that scaling factors of males seem higher in the second age class (0-6), brainwise and mainly in temporal and cerebellum areas along the direction 1. This is also notable in the same regions between 6 and 12 years, this time along direction 3. For the older class (12-19), this phenomenon essentially appears brainwise along the direction 3 and in the parietal lobes along direction 1.

5.5.4 Multi-directional growth charts

Additionally to previous experiments (and to partially overcome direction selection problems), it is possible to repeat the process of scaling factor extraction along different directions. Due to symmetry reasons, the first direction, which is the one orthogonal to the sagittal plane, is quite relevant so we chose to keep it in all repetitions. This leaves us the freedom to rotate the

couple of remaining orthogonal directions in the perpendicular plane of the first one. Actually, a $[0, \frac{\pi}{2}]$ angle interval is enough to cover all the possibilities. We sub-sampled this interval into 20 equidistant values of angles leading to the same amount of different couples of orthogonal directions.

We then extracted scaling factors for all those directions, for all ROIs of all subjects. In order to obtain an easily interpretable visualization, we imagined a chart to display the average growth at different timepoints in every direction from a longitudinal point of view. We chose those timepoints to be every months between 0 and 1 year. For each timepoint, a weighted average of the scaling factors is computed such that the contribution of each subject is modulated according to its temporal distance to that timepoint. This has been done using an adaptive quintic weight function, flexible enough to avoid temporal error (more details in Section 8.2). We end up for each month with average scaling factors in each of the 21 sampled directions. Then smoothing splines with periodic boundary condition were used to obtain values of scaling factors along any direction. It is thenceforth possible to create a polar representation were the angular coordinates are the directions of scaling and radial coordinates are the associated scaling factors. Those multi-directional growth charts are shown in Figure 5.9. Concerning the growth speed, those charts should be read in the opposite way to the contours found on maps. Indeed, the further apart the lines are, the greater the expansion during the month.

Once again, the anisotropic development of the chosen structures of the brain is highlighted. The most noticeable is the temporal lobe case. It could have been possible to extract the scaling factors in a 3D sampling of the directions instead of restraining ourselves to the one coplanar to the sagittal plane. However, this requires a huge number of registrations and it was not clear for us how to produce an easily understandable visual representation of it.

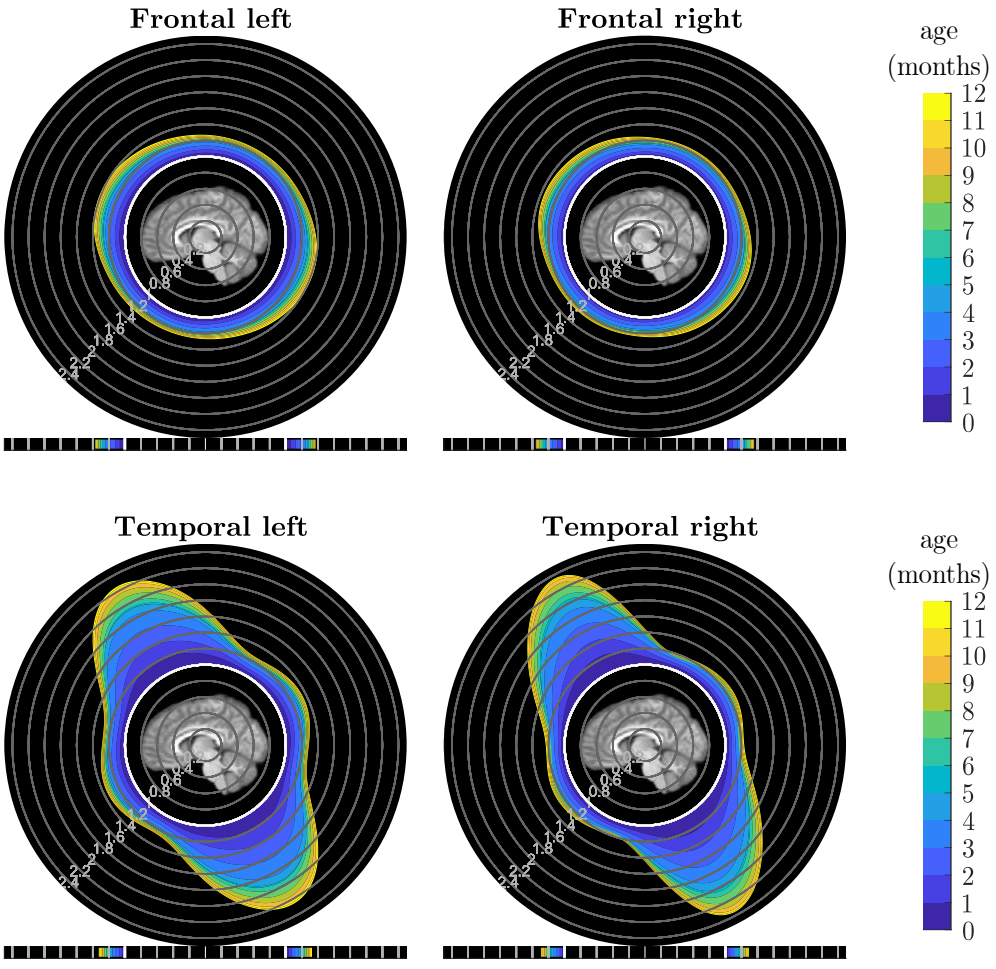

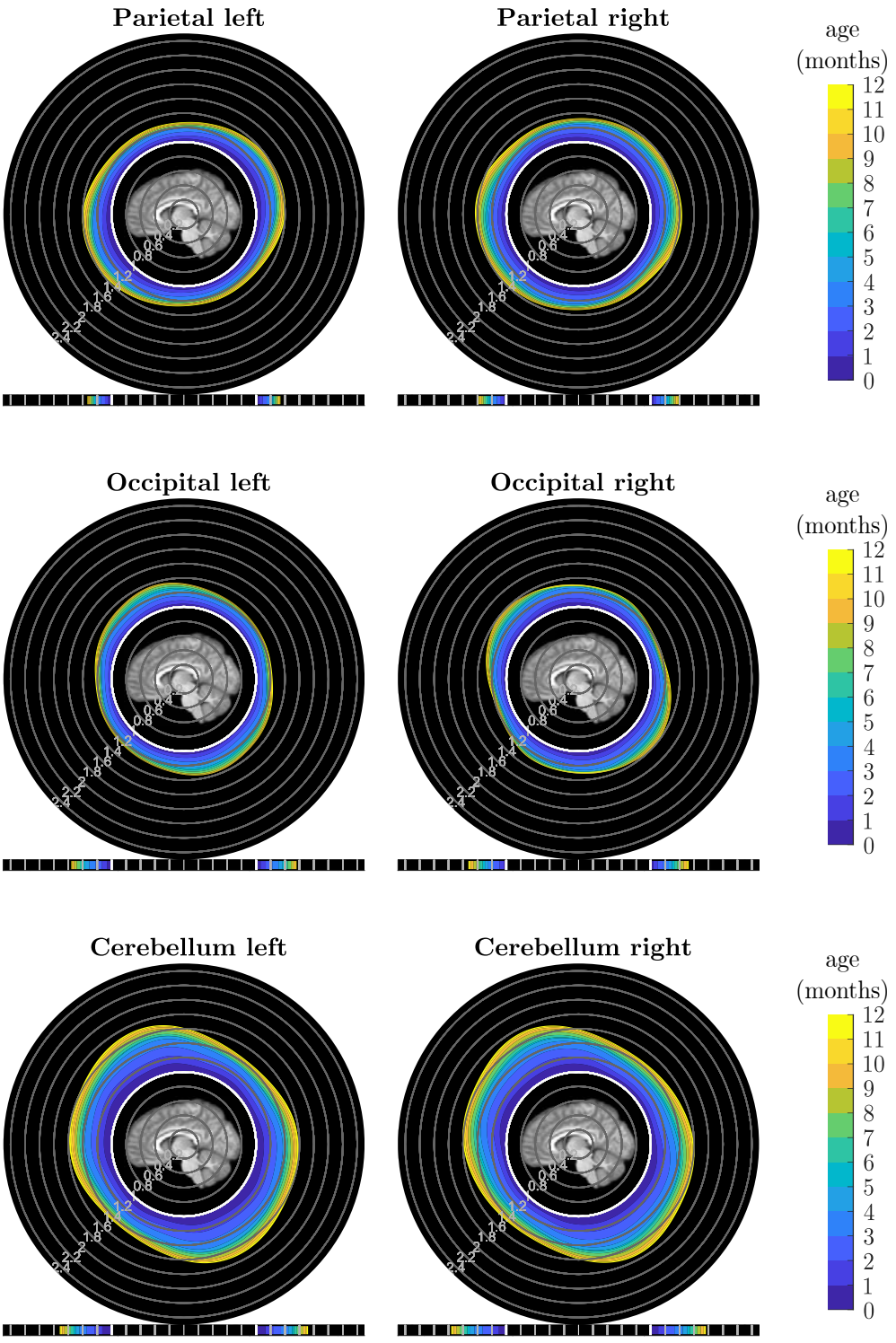

Figure 5.9: Multi-directional monthly growth charts from a sagittal point of view between 0 and 1 year. Scaling factors in every directions coplanar to the sagittal plane are displayed using a polar representation, the unit circle corresponds to birth. Scaling factors along the direction orthogonal to the sagittal plane are displayed below the polar plots.

5.5.5 Influence of the common reference

To evaluate the influence of the common reference image, the whole process described previously is reproduced using six different reference images. Those are atlases for six arbitrary chosen time-points $t_1, \ldots, t_6$ using subjects among the population depicted in Section 5.4.1. Time-points are chosen such that five of them cover the period in which the majority of the brain expansion occurs, the last is positioned later, in a stabilized area. Following [Legouhy 2019], an atlas for a time-point t_i is created using only the subjects with ages in a range around t_i (in Figure 5.10, line 4). The contributions of those subjects are then weighted using a weight function (plotted in Figure 5.10, line 6) such that subjects closer in age to t_i are given more importance. The six outputed atlases (presented Figure 5.10) are different in terms of shape and intensity, they will be used to challenge the robustness of our method to extract scaling factors.

The method developed in Section 5.4.2 is used for each of these reference images, on which directions of scaling for the anisotropic similarity registration have been established the same way. A scaling factor $s(i, j, d, k)$ is thus computed for each ROI j of each subject i based on each reference image k along each chosen direction d. To quantify the influence of the reference image on absolute scaling factors, the results, using the six reference images previously depicted, are compared through two approaches:

1. A pairwise study to evaluate whether or not reference atlases closer to each other in age are more likely to generate closer results.

2. A study of the standard deviation among results for all reference atlases to evaluate how far they are from the average results.

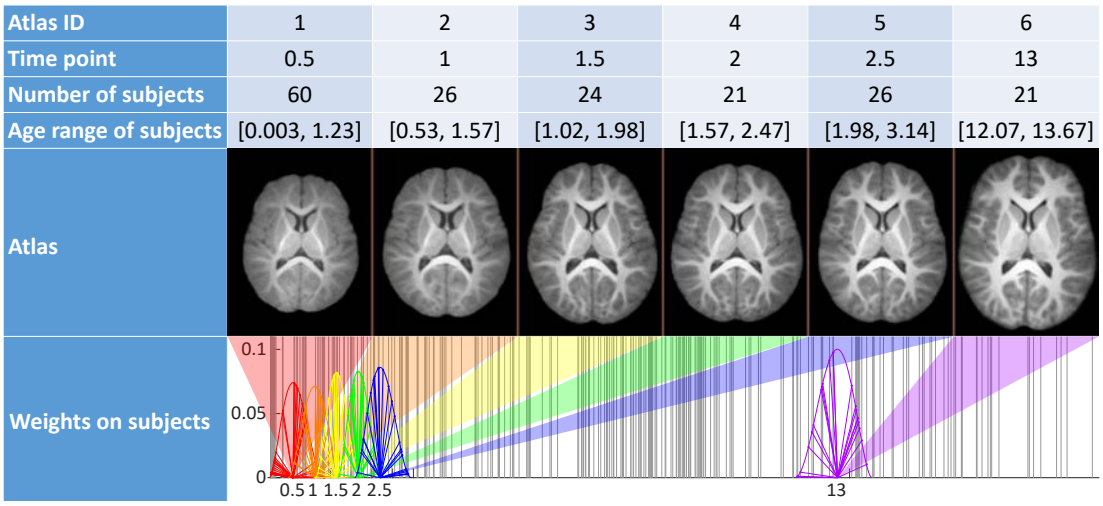

Figure 5.10: Characteristics of the 6 atlases used as reference image (time is displayed in years).

5.5.5.1 Study of pairwise distances between scaling factors by reference images in each direction for each ROI

Our aim is to determine whether or not reference images closer to each other (atlases at shorter temporal distances) are more likely to generate less important absolute differences between their results. We therefore compute the absolute difference of the resulting scaling factors between each pairwise combinations of reference images. Then, those distances are normalized by the average of corresponding scaling factors between the two atlases such that it can be seen as a

percentage of it (relative distance). The relative distance between scaling factors from reference atlases k and l is then computed as:

$$D_{k,l}(i,j,d) = 2\frac{|s(i,j,d,k) - s(i,j,d,l)|}{s(i,j,d,k) + s(i,j,d,l)} \tag{5.12}$$

After examination of all the pairwise combinations, the temporal distance between the reference images does not seem to have an impact on the distance of the scaling ratios associated to each other (Figure 5.11). The highest median of relative distance happens to be between atlases 2 and 5 for right basal ganglia, but does go above 8% of difference.

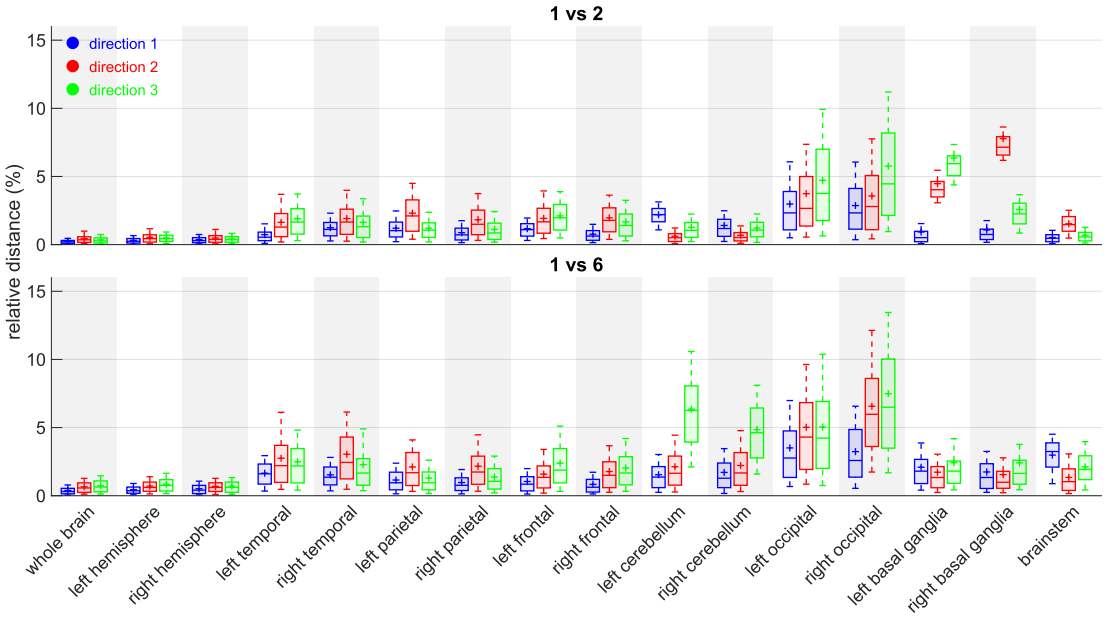

Figure 5.11: Relative distances between reference atlas 1 and 2 (top), 1 and 6 (bottom). Boxplots among subjects for each ROI j, each direction d: boxplot$(D_{k,l}(.,j,d))$.

5.5.5.2 Study of the standard deviation among reference images in each direction for each ROI

This method gives an average measure of the distances between the results for each atlas and the average results. Those distances are normalized by the average of corresponding scaling factors of all the atlases. The relative standard deviation between scaling from all reference atlases is then computed as:

$$D(i,j,d) = \frac{\sigma(s(i,j,d,.))}{\overline{s(i,j,d,.)}} \tag{5.13}$$

The graphs (Figure 5.12) suggest that the method, when applied to large regions such as whole brain and hemispheres, is really robust to reference image change. Occipital lobes and cerebellum however seem to be more vulnerable areas. Those two regions share a common border and we believe that the segmentation process is a crucial step in that case. The cerebellum position indeed varies quickly in early stages of life and our decision to use segmentations based on neonates can be a bit inadequate for this area in particular. We also think that the way we chose to define the constrained directions of scaling (especially those using purely geometrical considerations through PCA on voxel coordinates) may not be the most robust in those areas. More anatomical features could lead to even smaller influence of the reference image.

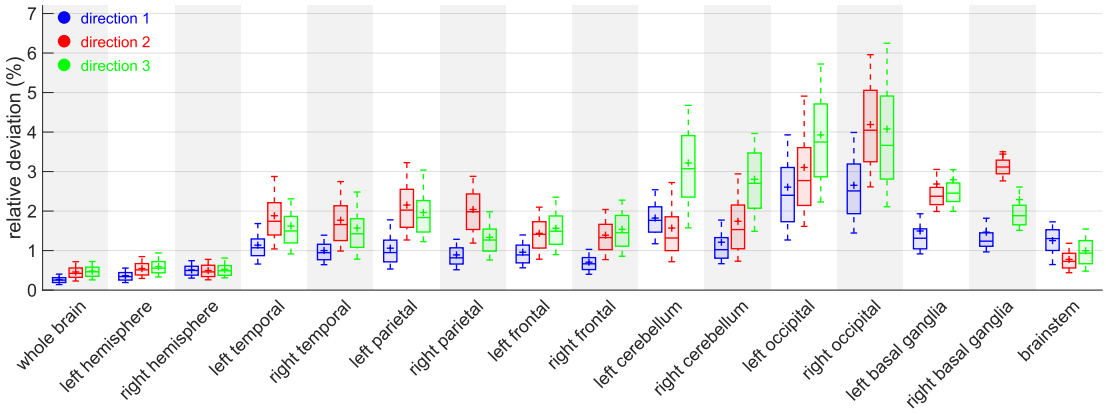

Figure 5.12: Relative standard deviation between reference atlases. Boxplots among subjects for each ROI j, each direction d: boxplot$(D(.,j,d))$.

5.6 Discussion

5.6.1 Comparison of the results to the literature

Our method aims at characterizing directional growth at the scale of a ROI through the extraction of scaling factors, which are easily interpretable measures. In most longitudinal analyses of brain development, the focus is on volumetry. This type of measurement reflects the global growth of a region but lacks characterization of directional expansion. Other approaches are based on cortical surface curvature as in [Lefèvre 2016], [Auzias 2015] or [Kim 2016] to reflect gyri and sulci widening or deepening, giving information about directional expansion at a more local scale.

Values from volumetric measurements cannot be directly compared to our scaling factors: they are three-times unidimensional whereas volume is not. Our anisotropic scaling factors should instead be seen as a complementary information to the volume data. However, there are still some aspects that we can compare:

- The pace of growth: is the growth monotonous or does it increase or decrease in speed at given ages? Are there regions that seem to evolve at a quicker pace than the others do?
- The asymptote: at what age does the growth reach a peak and begins to stagnate? Are there regions that seem to reach a higher growth asymptote than others do?

Since the anisotropy is a missing information in volumetric studies, it is appropriate to use the average models of the three directions (black curves in Figure 5.7) for the comparisons. In [Hamano 1990], [Peterson 2018], [Courchesne 2000] and [Iwasaki 1997], the pace of the whole brain volume curves is quite similar to our findings, showing a strong initial increase followed by a decline around 2 years. In [Knickmeyer 2010], it is also noticeable that, analogously to our results, the cerebellum grows by a much more important factor than the brain as a whole. In [Iwasaki 1997], basal ganglia grow by a factor comparable to the whole brain which is also consistent with our results.

5.6.2 Implementation considerations

5.6.2.1 Directions of scaling

The choice of the scaling directions, characterized by the matrix U, is crucial. These three directions can be different for each ROI, they are defined on the reference image and must be

orthogonal. The brain being a rather symmetrical organ about its mid-sagittal plane, choosing a direction orthogonal to it seems natural. Given that, there is no obvious choice for the other two. Using PCA on non-zeros voxel coordinates of the reference image (atlas of the population in our case) projected on mid-sagittal plane (since the last two directions have to be orthogonal to the first one) seemed to be quite intuitive. This corresponds to the principal sagittal directions of the average model of the population. However, it is based on purely geometric features ignoring iconic or anatomical considerations. This choice must above all be seen as a proof of concept and should not be considered as the one to be necessarily adopted. A future work could be to define, for a given purpose, a criterion of goodness for the chosen directions and, to optimize to find the directions that best satisfy this criterion. A more anatomically-oriented approach could be to ask a medical expert to point, on the reference image, the anterior commissure - posterior commissure (AC-PC) line. This has been well adopted as a standard by the clinical neuroimaging community even though it is mostly a convention for visualization and at the cost of introducing a human interaction or a preprocessing step. This method is therefore very flexible in the choice of the scaling directions and the ROIs, yet it has shown oneself robust concerning the choice of the common reference image.

5.6.2.2 ROI segmentation

Although it does not call into question the method itself, there is room for improvements in the way we segmented the ROIs. The main difficulty is to find a method that is reproducible while being adaptable to brains from subjects scanned across a wide range of ages, which induces a large variability in contrast and shape. It has been shown in [Gousias 2010] that the automatic segmentation of 1 year old subjects was more successful when using prior segmentations of 2 years old than when using prior segmentations of adults. In addition, [Aljabar 2009] showed that, in the context of multi-atlas segmentation, similarity selection of the atlases increases significantly the accuracy compared to the fusion of random sets of atlases. In the same paper, it has also been established that using an age-based selection gives similar results to similarity selection. Those results support the assertion that segmentation accuracy is improved by using age-adapted atlases. However, the concern of producing segmentations on a longitudinal database that are adapted to the maturation of each brain while being consistent among the subjects is still, to our knowledge, an open question. Our choice to use ALBERTs atlases to segment all the subjects regardless of their age was driven by a desire of consistency/reproducibility to the expense of age-adaptation since we did not find methods offering a satisfying trade-off between the two.

5.6.2.3 Normalization step

We have used a normalization step instead of the raw scaling factors relative to the reference image. Even though it is in a way more abstract, the relative scaling factors can actually be used as such. A subject with abnormalities that would show itself atypical in terms of scaling factors compared to the normal model would be so, with or without normalization. Now it is indeed more tangible for interpretation to have a concrete base like birth. In that case, scaling factors have an intuitive meaning since they quantify how much a region grows along a given direction since birth. In the event that there is no neonatal data to normalize the relative results, the following could be done:

- If a model can be fitted from the relative scaling factors, it might be possible to extrapolate values for birth and therefore use them for normalization.

- If not, relative scaling factors may be used or another base should be considered. Taking values in the growth stabilization zone may also be considered as it gives easily interpretable results as well.

That being said, neonatal MRI data are nowadays quite abundant in open access, especially structural images. The dHCP team (see Acknowledgment C) announced in September their second release with over 500 neonates. Our normalization can therefore be performed when using this data.

5.6.2.4 Image quality

Images used in the experiments are of good quality compared to what can be commonly found in clinical routine. Registration is sensitive to image quality but it is mostly the case in the context of non-linear registration where there are many degrees of freedom and very local displacements are involved. Even if the image quality can have an impact, the sparsity in terms of degrees of freedom and the global aspect of the anisotropic registration make it much more resilient about image size and quality. In addition, the bigger is the size of the ROI is, the less sensitive to image quality the result will be. The registration algorithm being based on block-matching, the ROI must be chosen such that their sizes are at least one order larger than the size of the blocks. A block being a neighborhood of voxels, the poorer the image quality, the larger the ROI must be and too narrow structures should be avoided. Finally, conducting the study at a group scale attenuates the influence of potential registrations errors induced by a poor image quality.

5.6.3 Clinical applications

We focused on the expansion of structures of a database of healthy subjects but we can also imagine using this method for patients. Intra-individual surveys are also possible, for subjects that had multiple scans through time, to monitor the evolution of a brain sub-region or any part of the body and infer the way it is going to expand.

Brain morphometric measurements have been performed on infants with deformational plagiocephaly and controls in [Collett 2012]. They found that volume analysis does not allow the distinction between cases and controls. However, their unidimensional measurements based especially on distances between landmarks were more successful. Those nevertheless necessitate point picking on all subjects and may be sensitive to human error. Considering this, it could be interesting to try, in future work, our automatic method (only the computation of directions for each ROI on the common reference is needed) on this kind of pathology. Some chosen directions could for example be colinear to the line segments that have proved to be relevant in this paper. Those measurements might be linked to developmental delays that affect infants with deformational plagiocephaly.

5.7 Conclusion

We have presented a method that allows the extraction of regional and global scaling factors along arbitrary chosen orthogonal directions. This is done through linear registration using a 9 dof transformation, anisotropic similarity, which is an affine transformation with constrained directions of scaling.

The main methodological contribution of this paper concerns the resolution of the problem of finding the optimal anisotropic similarity that best matches two sets of paired points. This result has made possible the development of a block-matching registration algorithm based on this transformation.

Given this new type of registration, our second contribution was to map a database of subjects between 0 and 19 years old using anisotropic similarity onto a common reference image on which the constrained directions of scaling of our choosing have been fixed. Registrations have been performed brainwise and ROI wise (lobes, cerebellum, basal ganglias...). For genericity

purpose, we chose this reference image to be an atlas made from the subjects. Based on symmetry and geometrical considerations, we defined the same constrained directions of scaling for all ROIs even though it is possible to choose different ones for each. As an output, we obtained for each subject, for each ROI, for each chosen direction a scaling, a scaling factor that we normalized such that it represents an expansion factor from birth.

Those scaling factors have been used to model the anisotropic development of the brain. After model selection, it has been determined that rational function with polynomials of degree 1 as numerator and denominator is the best suited among the tested candidates for that modeling. Curves representing scaling factors as a function of the age for each ROIs, each chosen direction, along with associated confidence intervals have then beeen computed on a combination of four databases.

Tests to determine the influence of gender in those scaling factors have been performed for different age-intervals. Finally, two experiments have been conducted to evaluate the influence of the aforementioned common reference image. The results have shown small relative differences depending on the choice of the reference image leading to the conclusion that the method is robust in that aspect.

Chapter 6

Application to newborn data

Contents

In this chapter are reported the main results of the study we jointly performed with Maia Proisy on quantitative ASL imaging in a specific newborn population. The study, initiated by Maia Proisy, gave rise to a journal publication in NeuroImage: Clinical [Proisy 2019].

My role in this study was mainly to adapt pre-existing processing tools designed for adults such that they can be applied for newborns. This includes robust registration for brains of different maturity, brain extraction, and atlas-based segmentation.

A newborn brain is not simply a smaller version of an adult one. In the early stages of life, the brain undergoes rapid structural and functional changes. Regions grow at an asynchronous pace and also shows local shape evolutions due to the gyrification process as shown in [Dubois 2019]. In addition, the myelination process leads to important tissue composition changes as shown in [Dubois 2014] which is translated in terms of images intensities. The massive disparities in terms of shape and intensity between infant and adult images explain why most of processing tools designed for adults often suffer flaws when used on infant data. This has been shown notably in [Muzik 2000]. An effort of adaptation of the tools is however currently being made as in [Baxter 2019].

The following is a concise version of [Proisy 2019] with an emphasis on the image processing aspects.

6.1 Introduction

Hypoxic-ischemic encephalopathy (HIE) is the leading cause of neonatal encephalopathy and occurs after perinatal asphyxia in full-term neonates, it is a major cause of perinatal mortality and morbidity. MRI plays a key role in the diagnosis and prognosis of this pathology. An early MRI (performed during the first week of life) reliably detects severe injuries and there is good agreement between early MRI and late MRI (after 1 week) [Charon 2015]. The brain perfusion model and its relationship to other biomarkers could help guide the development of therapies in order to improve management of high-risk neonates. Cerebral perfusion imaging is challenging in neonates due to physiological and technical issues [Proisy 2016]. The Arterial

Spin Labeling (ASL) MRI perfusion sequence is one of the most suitable imaging modalities owing to its non-invasive and non-irradiating nature. However, the post-processing of ASL data requires specific adaptations to this age group, in particular with respect to the automated segmentation of brain tissues and the parameters used for the quantification models of cerebral blood flow (CBF) [Varela 2015]. There are a dozen articles in the literature concerning the study of cerebral perfusion in neonates using ASL, four of which are focused on neonates with HIE [Pienaar 2012, Wintermark 2011, Massaro 2013, De Vis 2015].

The primary objective of our study was to evaluate the changes in CBF between an early MRI (at day 4 of life) and a late MRI (at day 11 of life) in infants with HIE treated with hypothermia. The secondary objectives were to compare CBF values between the different regions of interest (ROIs) and between infants with ischemic MRI lesions and those with normal MRI.

6.2 Material

6.2.1 Patients

This prospective study included all consecutive neonates with HIE admitted to the neonatal intensive care unit of our institution between April 2015 and December 2017. The criteria of national guidelines in [Saliba 2010] were used to determine eligibility for therapeutic hypothermia. All included neonates were aged of at least 36 gestational weeks with birth weight ≤ 1800 g. They had signs of perinatal asphyxia with an acute perinatal event (such as severe foetal heart rate abnormalities, cord prolapse or placental abruption) and at least one of the following criteria: APGAR score ≤ 5 at 10 min (Appearance, Pulse, Grimace, Activity, Respiration [Apgar 1953]); mechanical ventilation or intubation at 10 min after birth; metabolic acidosis, including cord, arterial, venous or capillary blood pH < 7 or base deficit ≥ 16 mmol/L or lactate ≥ 11 mmol/L within 60 min of birth. Neonates with stroke, congenital malformation or metabolic disorders were not included. Hypothermia was induced within 6 h after birth and continued for 72 h, with a target temperature of 33-34 °C. The institutional medical ethics review board approved the study and parental consent was obtained.

6.2.2 MR acquisitions

Each included neonate systematically underwent two MRI scans as follows: an early MRI performed as close as possible to day 4 of life (DOL4) and a late MRI performed as close as possible to day 11 of life (DOL11). The early MRI was performed after rewarming, at the end of hypothermia treatment. The neonates received no additional medication for the imaging study. Ventilated infants were sedated with morphine and midazolam. Spontaneously breathing infants were not sedated and were fed before the MRI scan and wrapped with a *vacuum immobilizer*.

All MRI scans were acquired using a Siemens 1.5 T Magnetom Aera scanner with a 20-channel head/neck coil. Among the sequences included in the routine protocol, the following two were used for processing:

- 3D T1-weighted (T1w): acquired in sagittal plane, TR = 2090 ms, TE = 4.9 ms, resolution $1 \times 1 \times 1$ mm^3.

- 2D axial pulsed ASL PICORE Q2TIPS: TR = 3500 ms, TE = 12 ms, TI1 = 700 ms, TI2 = 2000 ms, in-plane resolution 4×4 mm^2, slice thickness 8 mm, gap 2 mm, 9 slices, 30 label/control pairs. This lead to a total scan time of 3 min 39 s. The first volume of the ASL series was used as the M0 reference image.

6.3 Image processing

6.3.1 Anatomical data

In order to compute CBF values in chosen areas of the brain, a segmentation step has been performed on the structural T1-weighted images. For the segmentation to be done properly, it is required to work with brains only thus necessitating first a skull stripping process.

This step turned out to perform very poorly using standard tools such as fsl BET[1] or Volbrain[2] which are designed for adult data. Given that, we chose to opt for atlas-based brain extraction and segmentation which can be adapted easily to any age range given the appropriate atlas, and shows nice reproducibility properties. We used for that purpose an age-adapted set of anatomical images and segmentation maps pairs from ALBERTs [ALBERTs]. It consists in 20 neonates brain T1 and T2-weighted images with associated manual delineation of 50 regions. The cohort is composed of 15 preterm neonates scanned at term (age range: 26-35 gestational weeks), 5 term control (age range: 39-45 gestational weeks), and 36 preterm neonates scanned at birth (age range 24-36 gestational weeks).

Atlas creation

We first created an atlas from all ALBERTs T1-weighted data using the algorithm developed in [Legouhy 2019] based on [Guimond 2000], and detailed in Chapter 8. The associated segmentations were then mapped onto this common space using the transformations from the atlasing process and fused using majority voting.

Brain extraction

In order to create a whole brain mask, we merged all the labels and performed a special closing composed of a dilation (4 mm), followed by a hole filling, followed by an erosion (4 mm).

However, it was not straightforward to propagate this brain mask onto our patients. Indeed, due to massive differences in terms of field of view (FOV) between our data and those of ALBERTs, the registration algorithms failed to aptly map the atlas on our images. Indeed the FOV of our data goes below the chest while it stops at about the jaw for ALBERTs ones (see Figure 6.1 for an illustration of the difference of FOV). We thus had to find a way to crop our images to make them compatible with ALBERTs.

Hopefully, we had in our possession a pre-built atlas with exactly the same FOV as the data on this study. It was also made from newborns and included associated segmentations that have been drawn by a junior radiologist (AN) at our institution. Those however do not cover the brain, the union of all the labels only roughly representing the cerebrum. Summarizing, we therefore have two atlases shown in Figure 6.1 with complementary qualities:

- The in-house atlas, compatible with our data in terms of FOV but associated with novice segmentation of a limited amount of regions.
- The ALBERTs atlas, not adapted to our data but together with expert segmentations of a high number of regions.

In order to take advantage of both, we linked the two through a rigid registration of the biggest common segmented region which happened to be just about the cerebrum. This gave us a transformation allowing to propagate the FOV of ALBERTs to produce a cropped version of our in-house atlas. As shown in Figure 6.2, it was then possible to also propagate this FOV from the in-house atlas to all patient images of the study.

[1] https://fsl.fmrib.ox.ac.uk/fsl/fslwiki/BET
[2] https://www.volbrain.upv.es/index.php

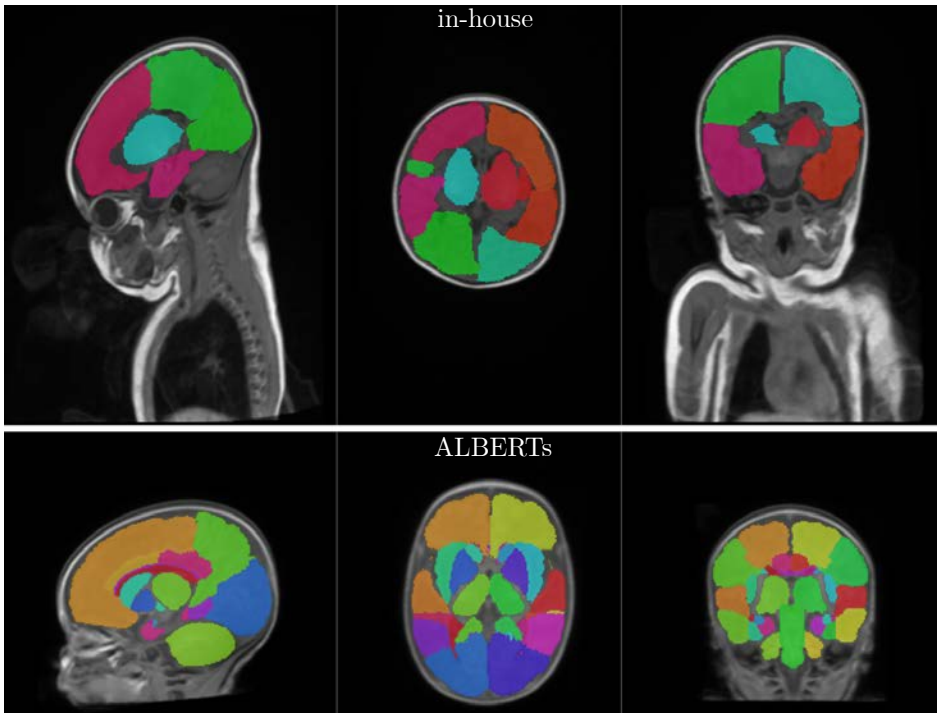

Figure 6.1: In-house and ALBERTs atlases together with the associated segmentation maps.

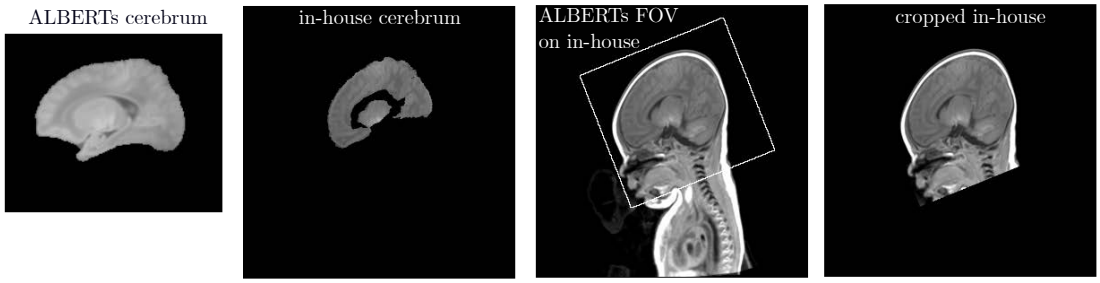

Figure 6.2: Largest common segmented part of ALBERTs atlas (first) and in-house atlas (second). The registration of the two allows to propagate the FOV of ALBERTs onto the in-house atlas (third) to create a cropped version of the in-house atlas (fourth) the linking the two atlases

From then on, it is feasible to properly map the ALBERTs atlas to our data through an affine followed by a diffeomorphic registration using block matching algorithms from [Anima]. This allows to propagate the brain mask and thus perform brain extraction on our patients.

All the registration mentioned below were then performed on brain-extracted images.

Intra-patient registration

For each patient, the DOL4 T1-weighted image was mapped onto the DOL11 one through an affine registration using Anima to recover the slight yet non-negligible changes in brain growth.

ROIs segmentation

The 50 regions delineated in ALBERTs were too refined compared to the voxel size of our ASL data so we chose to select and merge subsets of those ROIs to obtain larger ones. The resulting

regions were: frontal, parietal, temporal and occipital lobes, and the basal ganglia and thalamus (BGT) for the left and right hemispheres. A cortical gray matter (GM) ROI was additionally defined as the union of the four lobes in order observe cortical GM without BGT.

Those regions were then propagated to the patient DOL4 images using once again affine then diffeomorphic registration and carried over to the DOL11 images through the above computed intra-patient transformation.

We thus ended up at this stage with segmentations for all patient both at DOL4 and DOL11.

Tissue class segmentation

In order to obtain probability maps for tissue segmentation of gray matter (GM), white matter (WM) and cerebro-spinal fluid (CSF), we used SPM8 toolbox (Wellcome Department of Imaging Neuroscience, University College London, London, UK). Instead of using the default SPM8 template (MNI ICBM-152) tissue probability maps as an a priori for brain tissue classification, we chose instead the more age-appropriate ones from Serag's neonatal atlas [Serag atlas].

Note that we defined the gray matter a priori probability map as the sum of the [Serag atlas] atlas cortex, deep gray matter, brainstem and cerebellum maps. The quality of the segmentation was visually checked by a radiologist.

For some unclear reasons, the anatomical images needed to be first roughly aligned with the a priori maps for the SPM segmentation algorithm to work. One hypothesis is that SPM was not well able to recover for large rotations. This reorientation has been performed through rigid registration using [Anima].

6.3.2 Perfusion data

The ASL images for all patient and all time points were processed using a custom-built ASL pipeline based on SPM8[3] software and Matlab® (The MathWorks, Inc.).

Motion correction

For each patient, the native ASL series was first visually inspected in order to detect too large motion and perform manual suppression of control/label pairs where appropriate. An intra patient rigid registration was then performed to align all volumes within the ASL 4D image onto the first one.

Quantification

Leaving aside the first volume of the series, the M0, the labels and controls were pairwise subtracted to produce a series of perfusion-weighted maps. Along with the M0 map, this series undergone a multi-modal rigid registration onto the T1-weighted image using mutual information as similarity criterion. The perfusion-weighted (PW) map has then been computed through a robust average, using Huber's loss function [Huber 1964], across the repetitions.

This robust PW map was eventually converted into a quantitative ASL CBF map by applying the standard kinetic model [Buxton 1998, Wong 1998]:

$$CBF = 6000\frac{\lambda\Delta M e^{\frac{TI_2+idx_{sl}TI_{sl}}{T_{1b}}}}{2\alpha TI_1 M_{0b}} \quad [\text{mL}/100\text{ g}/\text{min}] \tag{6.1}$$

Where the factor 6000 converts the unit from mL/g/s to mL/100 g/min. The labeling efficiency α was assumed to be 98% and the blood/tissue water partition coefficient λ to be 0.9 mL/g [Alsop 2015]. δM is the PW map. $TI_1 = 700$ ms is the temporal width of the bolus. TI_2, inversion time, is the time from the initial pulse to image acquisition (2000 ms). TI_2 is adjusted

[3]SPM: https://www.fil.ion.ucl.ac.uk/spm/

for each slice to take into account the time interval TI_{sl} (47 ms) between slice acquisitions in our 2D multi-slice ASL sequences. idx_{sl} is the slice index (0 for the first slice). T_{1b} is the longitudinal relaxation time of blood that was assumed to be 1350 ms. M_{0b} is the longitudinal magnetization of blood at equilibrium and is approximated by the M0 map.

CBF map segmentation

To perform the CBF analysis on previously segmented ROIs, the label maps of each patient were resampled into the grid of the CBF maps and intersected with the gray matter probability maps thresholded at 0.7. Basic statistics on CBF were then performed for each ROI on the CBF ROIs.

6.4 Experiments and results

6.4.1 Study population

The 28 neonates included in the study were composed of 16 boys and 12 girls. All of them underwent the DOL4 early MRI. There was no DOL11 MRI for 5 neonates, due to non-availability of an ASL sequence (n=4) or death of the patient before DOL11 (n=1), giving 51 scans in total. The median age of the early MRI was day of life 3.7 (range: 3-5) and that of the late MRI was day of life 10.6 (range: 9-12). The mean gestational age at birth was 39.7 weeks (range: 36.7-41.9). Blood hematocrit values were available in 25/28 patients at DOL4 and 11/23 patients at DOL11, and the respective means were $43\% \pm 6\%$ (range: 27-58) and $38\% \pm 7\%$ (range: 26-55).

Quality check

ASL CBF maps were rated according to their image quality by MP (7 years' experience with ASL images). Images were considered as good quality when no or only minor artifacts were present, as moderate quality when moderate artifacts were present and did not prevent image interpretation, and as poor quality when marked artifacts were present or images were considered unreadable. In addition to visual evaluation of the ASL data, we also performed an automated quality check. As the PW map may present with negative values due to the inherent low resolution and SNR of ASL, the percentage of negative values was calculated in the whole brain, GM and WM.

Fourteen (27%) MRIs were excluded because of poor CBF map image quality and more than 20% negative values in GM. This left 37 MRIs: 17 DOL4 and 20 DOL11. 11 neonates had both early and late MRIs of good quality available.

MR images classification

Two experienced pediatric radiologists (VC and MP with, respectively, 7 and 9 years' experience) scored brain injury on MRI (T1, T2-weighted and DWI). Early and late MRIs were assessed independently. The reviewers were blinded to the ASL sequence, clinical details and outcome of the neonates but knew the age at the time of the MRI. Assessment of brain injury was based on a previously described simplified classification [Charon 2015] adapted from the Barkovich system [Barkovich 1998]. It distinguishes between normal and abnormal images. The differences were resolved by consensus between the two reviewers.

The conventional MRI scoring by the two experienced pediatric radiologists concluded that 8 out of 17 neonates (47%) had an abnormal DOL4 MRI and that 7 out of 20 neonates (35%) had an abnormal DOL11 MRI. For every patient, the scoring result was the same for the early and late MRI. No patients changed groups between the two time points.

6.4.2 Statistical analysis

The normality of the data distribution was checked through Shapiro-Wilk tests. As the distribution of the sample was not normal for the majority of data and because of the small sample size, non-parametric tests were used. Wilcoxon signed rank test was used to evaluate difference between DOL4 and DOL11 (paired samples), and differences between ROIs (paired samples) on DOL4 and DOL11. Wilcoxon ranksum test was used to evaluate differences between normal and abnormal MRI (independent samples) for each ROI. A p-value < 0.05 (two-tailed probability) was considered significant. The results are provided in bilateral ROIs.

Comparison of CBF values between DOL4 and DOL11, by ROI

As shown in Figure 6.3, a global decrease in CBF values occurred between DOL4 and DOL11 in all ROIs. Yet this difference was only significant for BGT ($p = 0.0049$) and temporal lobes ($p = 0.042$).

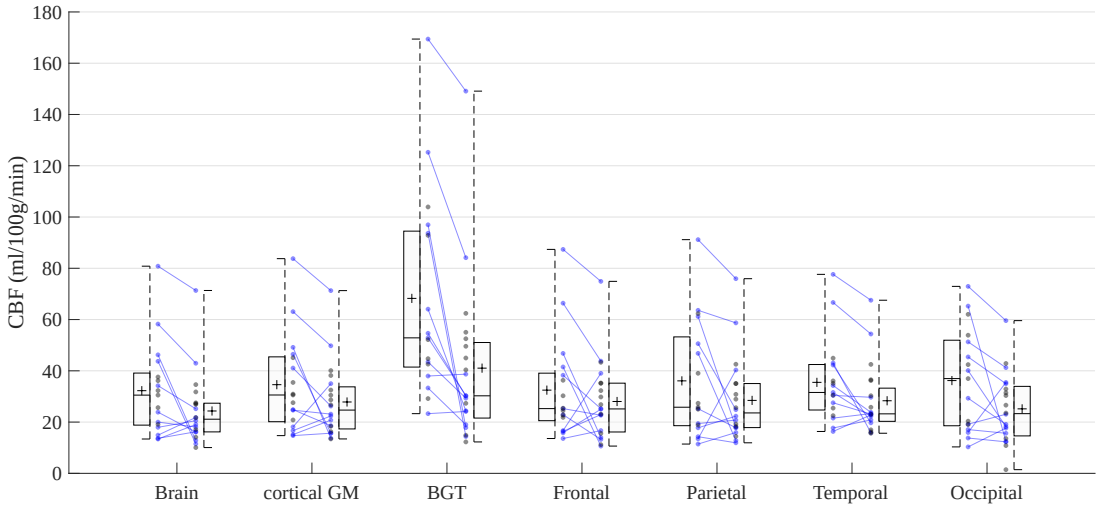

Figure 6.3: Box-and-whisker plots and mean (+ marker) for CBF by ROI on DOL4 (n=17) and DOL11 (n=20). Blue dot-and-line diagrams indicate infants with both DOL4 and DOL11 MRI (n=11).

Comparison of CBF values between ROIs, by DOL

Figure 6.3 also shows high CBF values in BGT compared to the other ROIs both at DOL4 and DOL11.

Comparison of CBF values between normal and abnormal MRI morphology, by DOL, by ROI

As shown in Figure 6.4, CBF values are globally higher for the group with abnormal MR images, for all ROIs, for both DOL4 and DOL11.

- On DOL4, those differences were significant for GM ($p = 0.0433$), BGT ($p = 0.0269$), frontal lobes ($p = 0.0209$) and parietal lobes ($p = 0.0161$).
- On DOL11, those differences were only significant for temporal lobes ($p = 0.0357$)

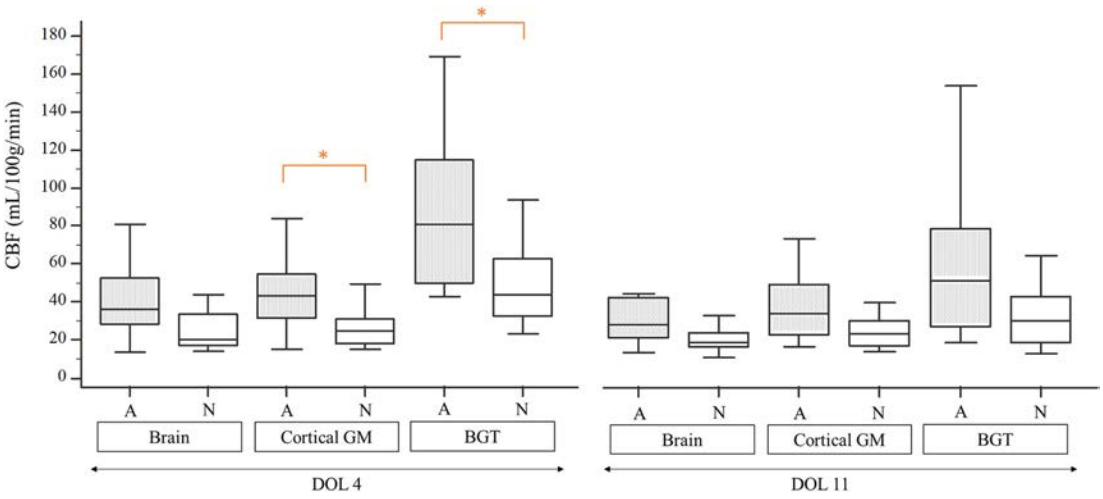

Figure 6.4: Box-and-whisker plots for CBF by ROI for patients with normal (9 on DOL4 and 13 on DOL11) and abnormal MRI (8 on DOL4 and 7 on DOL11).

6.5 Discussion

For a more complete discussion, see the one in [Proisy 2019]. We can however roughly extract some key points (clinical hypotheses and conclusions are left to Maïa Proisy's expertise).

From an implementation point of view, it appeared that ASL MRI seems to be well suited to study brain perfusion in newborns and was quite easy to operate. However, the automatic processing of those data was not straightforward. This is mainly due to the fact that most existing pipelines, for segmentation notably, are designed for adults. Since the time this study was made, progress have been made to adapt pipelines to newborn data as in [Baxter 2019] thanks notably to the emergence of the Developing Human Connectome Project [dHCP]. It seemed, at the time of the study, that the eye of a medical expert was necessary.

Regarding the results, the study exhibited higher CBF values in the BGT at DOL4, probably due to hyperperfusion of the BGT in patients with an abnormal MRI. Our results are consistent with the literature [Pienaar 2012, Wintermark 2011]. Also, some significant differences were found in DOL4 between normal and abnormal MRI groups but not at DOL11, which may suggest a normalization during the second week of life. We also found hyperperfusion in the cerebral cortex (cortical GM) on early MRI in patients with abnormal MRI, which has not been much studied in the literature. Finally, we found higher CBF values in the BGT compared to the cortical gray matter at both DOL4 and DOL11, which is consistent with literature, even in healthy neonates [Miranda 2006].

One of the main limitations of this study is the low number of patients accentuated by a 27% exclusion rate based on image quality. Those were not motivated by motion artifacts, which questions potential failures in the acquisition, notably the labeling process. Also ASL images shows very low SNR and quite massive voxel sizes leading to important partial volume effects. The choice of the quantification parameters is a matter of debate. Finally the absence of a control group may be pointed out.

Part III

Contributions in atlas creation methods

Chapter 7

Preliminary: Robust linear registration using transformation decomposition

Contents

7.1 Introduction

Dealing with brain scans coming from longitudinal studies implies differences of maturation between the subjects and therefore a large variability in terms of brains size and shape. This can be an issue for the proper functioning of image processing algorithms and more particularly for registration. Indeed, direct rigid registration can be corrupted by strong similarities on the edges of the brain. Estimating directly a rigid transformation between the images may then lead to shifted brain barycenters and misaligned mid-sagittal planes as shown later in Figure 7.1. This kind of feature is however occasionally needed especially in longitudinal atlasing where the 3D sub-atlases constituting average models of the brain at different timepoints have to be well aligned despite of their differences of maturation. In [Prima 2013], it was proposed to use the bilateral symmetry of the brain to guarantee the mid-sagittal alignment. The problem still persist though when searching in the remaining 2D-plane. We propose here a simple yet very efficient tool to improve the robustness of linear registration algorithms in this scenario. It consists in a robust rigid and similarity registration based on affine decomposition. This will be notably used implicitly in the longitudinal atlasing method developed in Section 8.

7.2 Method

To cope with robustness issues in linear registration, we propose to first estimate an affine transformation and then extract the rigid part from it through polar decomposition (PD).

Let $\hat{T}_A$ be the optimal affine transformation resulting from an affine registration. Let $\hat{A}$ and $\hat{t}$ be respectively the linear and translation parts of $\hat{T}_A$. As seen in Section 2.2.3.2, PD allows the factorization of $\hat{A}$ into $\hat{A} = \hat{Q}\hat{H}$, where $\hat{Q}$ is an orthogonal matrix and $\hat{H}$ is a positive-semidefinite symmetric matrix. $\hat{Q}$ satisfies the requirements of the linear part of a rigid transformation. Also, we have seen in Section 3.2.2.1 that, knowing an optimal linear part $\hat{Q}$ and the barycenters $\bar{x}$ and $\bar{y}$ of the two sets of homologous points, one can express

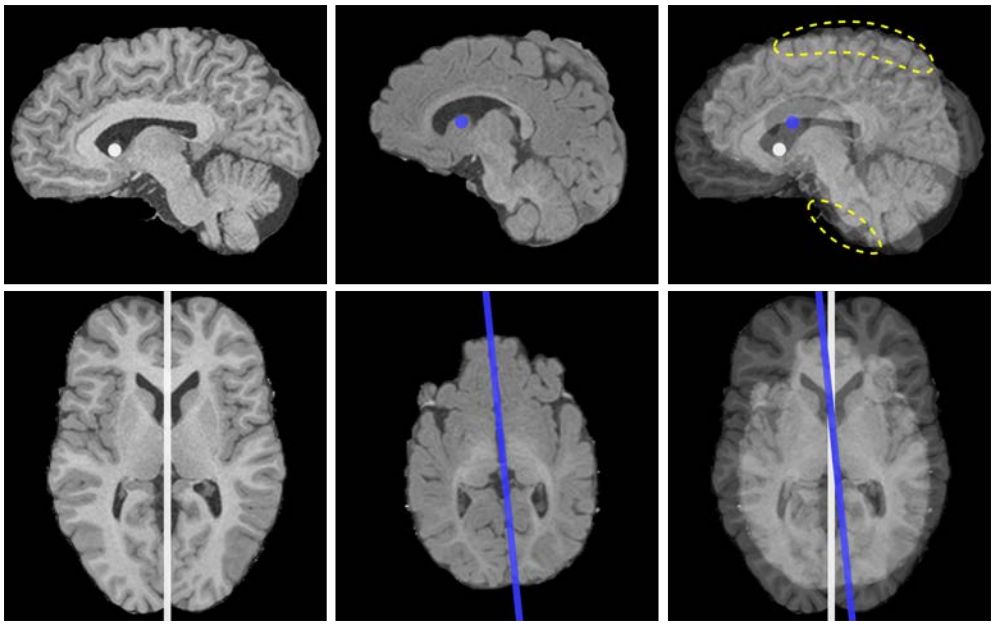

Figure 7.1: Reference image (left), transformed image after direct rigid registration (middle) and both superimposed (right).

the associated optimal translation $\hat{t}$ following $\hat{t} = \bar{y} - \hat{Q}\bar{x}$. This leads to the following rigid transformation $\hat{T}_Q$ extracted from $\hat{T}_A$ ans the two barycenters:

$$\hat{T}_Q = \begin{pmatrix} & \hat{Q} & & \bar{y} - \hat{Q}\bar{x} \\ 0 & \cdots & 0 & 1 \end{pmatrix} \tag{7.1}$$

Stripped of its rigid part, the remaining of the transformation $\hat{T}_A$ will be referred as a stretching transformation noted here $\hat{T}_H$, it embeds the scaling directions and factors, and is obtained as follows:

$$\hat{T}_H = \hat{T}_Q^{-1}\hat{T}_A = \hat{T}_Q^T\hat{T}_A = \begin{pmatrix} & \hat{H} & & \left(\mathrm{Id} - \hat{H}\right)\bar{x} \\ 0 & \cdots & 0 & 1 \end{pmatrix} \tag{7.2}$$

Remark. *An analogous reasoning can be applied to similarity registration. As seen in Section 2.2.3.1, SVD allows the factorization of $\hat{A}$, the linear part of the optimal affine transformation, into $\hat{A} = \hat{V}\hat{D}\hat{W}^T$, where $\hat{V}$ and $\hat{W}$ are orthogonal matrices and $\hat{D}$ is a diagonal positive matrix. Considering that those matrices are of dimension $n \times n$, we define the average scaling factor $\hat{d}$ through an arithmetic mean (or a geometric one since $D_{ii} > 0 \ \forall i$):*

$$\hat{d} = \frac{1}{n}\sum_{i=1}^{n} \hat{D}_{ii} \quad \left(\text{or } \hat{d} = \left(\prod_{i=1}^{n} \hat{D}_{ii}\right)^{\frac{1}{n}}\right) \tag{7.3}$$

Then, $\hat{K} = \hat{d}\hat{V}\hat{W}^T$ is a similarity matrix leading to the following similarity transformation $\hat{T}_K$ extracted from $\hat{T}_A$:

$$\hat{T}_K = \begin{pmatrix} & \hat{d}\hat{V}\hat{W}^T & & \bar{y} - \hat{d}\hat{V}\hat{W}^T\bar{x} \\ 0 & \cdots & 0 & 1 \end{pmatrix} \tag{7.4}$$

This similarity registration will only be used in the presented work as an initialization for local anisotropic similarity registration and not as an end in itself. A precise evaluation as for the rigid case is therefore not exposed.

7.3 Experiments and results

From a qualitative point of view, the proposed method shows improvements in terms of sagittal alignment and correspondence between central structures. This is exhibited in Figure 7.2 where the same images as in Figure 7.1 have been registered using this time a rigid transformation coming from affine decomposition. Orientation is globally better preserved and the small brain no longer seems to be pressed against the edge of the bigger one.

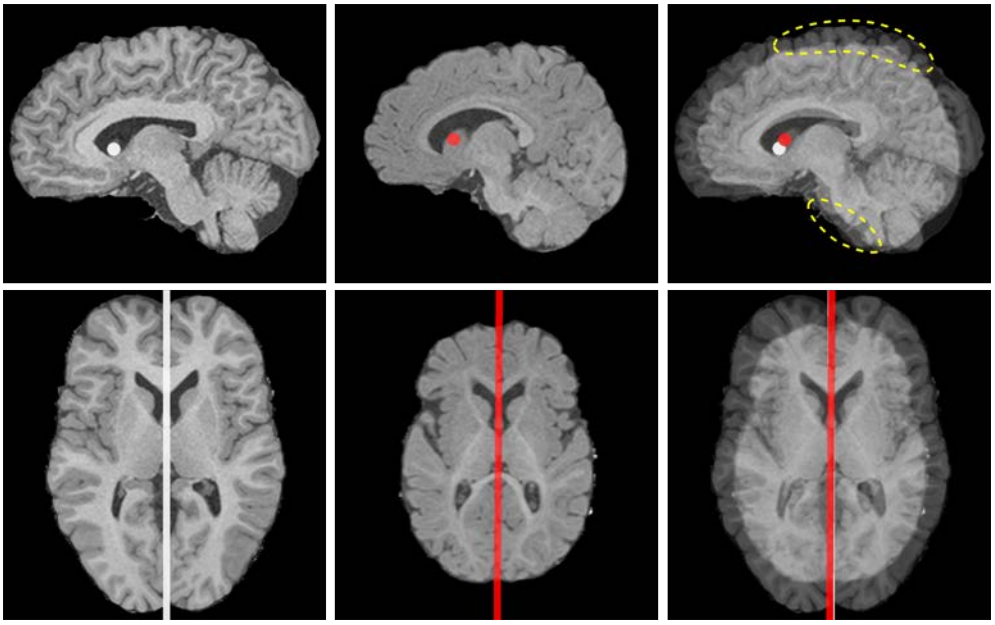

Figure 7.2: Reference image (left), transformed image after rigid registration from affine decomposition (middle) and both superimposed (right)

In order to perform a more quantitative analysis, two different experiments were conducted to evaluate the robustness of the rigid registration resulting from affine decomposition compared to a direct one using the same tools. The affine and rigid registrations are performed using the same block matching algorithm available in [Anima] with only a difference in the aggregation step to output the desired type of transformation. We used T1-weighted images from the ASLpedia study [ASLpedia]. Their voxel size is $0.5 \times 0.5 \times 1$ mm (axial, coronal, sagittal).

7.3.1 Fiducial points validation

The validation test is based on fiducial points picked according to anatomical considerations. As detailed in Table 7.1, ten subjects have been selected between 0 and 14 years old to represent different maturations of the brain and therefore a high variability in terms of size and shape.

age (years)	0.01	0.09	0.26	0.53	0.66	0.79	1.07	1.83	4.01	13.44
brain volume (mm^3)	344	599	822	914	1003	1114	1104	1231	1172	1617

Table 7.1: Age and brain volume of the subjects selected to evaluate the method.

To facilitate the point picking and improve reproducibility, all subjects were first reoriented such that the symmetry plane of the brain and the mid-sagittal slice of each image are coplanar

and the barycenter of the brain is at the center of the image. This step, performed using the method developed by [Prima 2002], induces a rigid transformation of the images.

Eleven points where then meticulously picked on each subject on various areas (corpus callosum, ventricles, brainstem, cerebellum, frontal and parietal lobes) as shown in Figure 7.3. Five are located in the mid-sagittal plane: points 1, 2, 9, 10 and 11 while the other are symmetrical pairs with respect to it: pairs of points $\{3, 4\}$, $\{5, 6\}$ and $\{7, 8\}$. The quality of the point picking was checked by an experienced radiologist (MP).

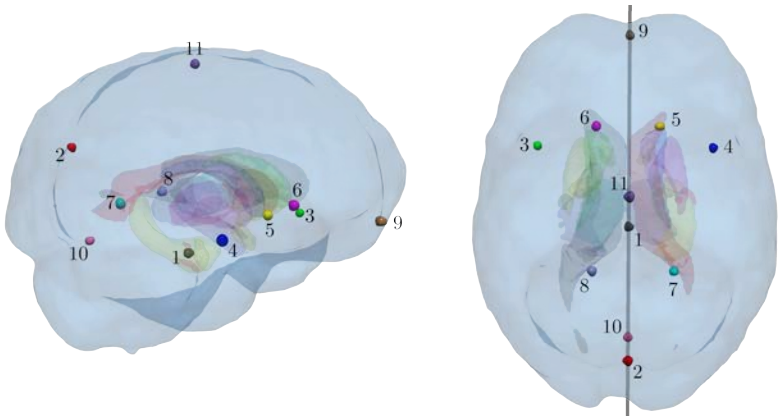

Figure 7.3: Fiducial points

The inverse of the reorientation transformations have then been applied to those points coordinates such that they match the native orientation. All subjects were registered to each other using i. direct rigid, ii. rigid from affine decomposition and iii. affine registration producing 90 resulting transformations for each. An error E_1 has then been calculated between transformed fiducial points associated to moving images P_T and those associated to reference images P_R using squared 2-norm:

$$E_1 = \|P_T - P_R\|_2^2$$

Boxplots of errors E_1 for direct rigid, rigid from PD and affine registrations are shown in Figure 7.4, the lower the better.

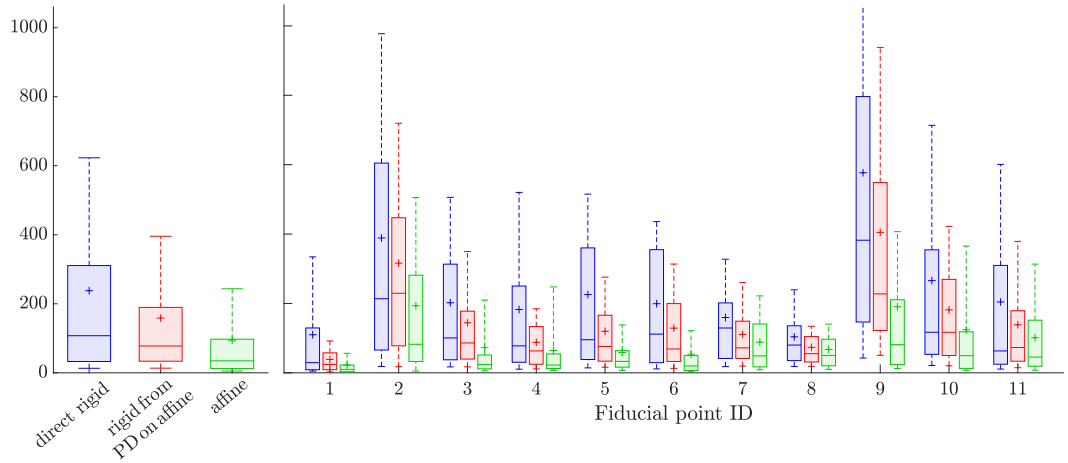

Figure 7.4: Boxplots with 1 and 9 decile whiskers of error E_1 in mm^2 for direct rigid (blue), rigid from PD on affine (red) and affine (green) registration. Globally (left) and for each fiducial points (right).

The fiducial point validation shows better results for the rigid registration from PD compared to the direct rigid one, especially for fiducial points 3-6 situated in the central-anterior part of the brain. The error is still high in the edges since changes in terms of scaling are not recovered.

7.3.2 Random transformations validation

The second validation technique evaluates the ability of the algorithm to match an image with a noisy, affine transformed version of itself. Three T1 images associated to subjects 1, 5 and 10 have been each transformed by 300 random transformations of form $A = PUdU^T SdUU^T$ where U^T is the orthogonal matrix of scaling direction computed via a PCA on the voxel coordinates, dU is a small rotation matrix deviating scaling directions (angle range: $[-\frac{\pi}{18}, \frac{\pi}{18}]$), S is an anisotropic scaling matrix (scaling range: $[0.6, 1.8]$) and P is a rotation matrix (angle range: $[-\frac{\pi}{6}, \frac{\pi}{6}]$). A Rician noise (average signal to noise ratio: 25dB) has then been added.

An error E_2 has been calculated between generated transformations T_G and estimated ones from registrations T_E using the log-Euclidean distance:

$$E_2 = \|\log(T_G) - \log(T_E)\|_F$$

where $\|.\|_F$ is the Frobenius norm. Results are shown Figure 7.5, the lower the better.

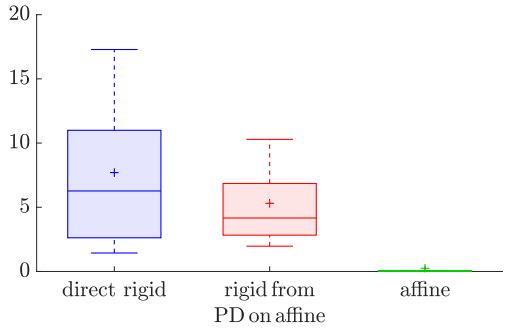

Figure 7.5: Boxplots with 1 and 9 decile whiskers of error E_2 for direct rigid (blue), rigid from PD on affine (red) and affine (green) registration.

The random transformations validation shows once again better results for the rigid registration from PD compared to the direct rigid one. This means that the output transformation from PD is closer to the initial induced affine one than the direct rigid counterpart.

7.4 Conclusion

Despite its simplicity and no traces found of it in the literature, this approach is surprisingly efficient to perform a rigid registration of two images of different sizes that preserves orientation and centering. This may seems at first glance to be a pointless concern but this simple addition to the domain of rigid registration will be of crucial help for further longitudinal studies in the following chapters.

Chapter 8

Unbiased longitudinal brain atlas creation using robust linear registration and log-Euclidean framework for diffeomorphisms

Contents

We present a new method to create a diffeomorphic longitudinal (4D) atlas composed of a set of 3D atlases each representing an average model at a given age. This is achieved by generalizing atlasing methods to produce atlases unbiased with respect to the initial reference up to a rigid transformation and ensuring diffeomorphic deformations thanks to the Baker-Campbell-Hausdorff formula and the log-Euclidean framework for diffeomorphisms. Subjects are additionally weighted using an asymmetric function to closely match specified target ages. Creating a longitudinal atlas also implies dealing with subjects with large brain differences that can lead to registration errors. This is overcome by the robust rigid registration based on polar decomposition proposed in the preceding chapter. We illustrate these techniques for the creation of a 4D pediatric atlas, showing their ability to create a temporally consistent atlas.

8.1 Introduction

Brain atlases are a crucial tool in medical imaging. They consist in an unbiased average model of the brain providing a way to compute statistics on populations, understanding brain variability but also to segment regions. Longitudinal (time dependent) atlases allow in addition the comprehension of brain development to highlight changes in growth, shape, structure etc. Those 4-D models are based on a set of 3-D atlases each for a desired timepoint using weight functions that modulate the contributions of the subjects according to their age fit with that timepoint. To produce an unbiased atlas, two different approaches are commonly used. The first one chooses a reference to register all the subjects to and iteratively unbias the atlas with respect to it [Guimond 2000]. The second common approach performs a direct groupwise registration of

all the subjects simultaneously [Rohlfing 2009]. This family of methods however often relies on a number of registrations in the order of the square of the number of subjects which can quickly be computationally expensive. Atlasing methods such as [Guimond 2000] provide a good average shape and intensity. However they define unbiased atlases up to an affine transformation, thus losing information on brain growth. On the other hand, [Kuklisova Murgasova Deprez 2011] corrects well for global size and shape (affine features) but ignores local deformations and thus leads to blurry images. [Serag 2012a] presented a technique that takes into account both global and local changes and uses a Gaussian kernel with adaptive width adjusted according to the temporal distribution of the subjects. However, the inflexibility of the Gaussian kernel does not guarantee that the age of the resulting atlas corresponds to the expected one.

We propose a longitudinal atlas creation method that is unbiased up to a rigid transformation accounting both for global and local transformations in the unbiasing step. Generalizing the procedure from [Guimond 2000] to longitudinal atlases, it only requires a number of iterations in the order of the number of subjects times the number of iterations. Additionally we extend this framework to handle diffeomorphisms using the log-Euclidean framework [Arsigny 2006a] and the Baker-Campbell-Hausdorff formula to quickly compose and average those transformations. In addition, a quintic polynomial weight function is introduced giving enough degrees of freedom to reduce temporal error of the 3D atlases while ensuring adaptivity to data distribution.

All these contributions are put together to construct a longitudinal atlas from a database of pediatric patients, illustrating the ability of our framework to obtain well defined temporal atlases in a robust manner.

8.2 Quintic polynomial weight function

Given a sample of N subjects of ages $\{\tau_1, \ldots, \tau_N\}$, to create an atlas representative of an age τ, it seems natural to give more importance to subjects closer in age to τ. This can be done by associating to each subject i a weight w_i based on its temporal difference to τ. The weights are then used in the averaging process (see section 8.3). The most common approach is to use a Gaussian kernel centered in τ with standard deviation σ. An adaptative σ can be used to harmonize the number of subjects of non-negligible weight in case of non-uniformly distributed sample ages [Serag 2012a]. Still, the inflexibility of the Gaussian kernel implies that if the τ_i are not distributed symmetrically around τ, the temporal error $E = |\tau - \sum_i w_i \tau_i|$ between τ and the computed age will be large leading to a temporally shifted atlas. We thus propose instead to use a more flexible weight function that is constraint driven and has an analytical solution. It consists in a quintic polynomial P, supported on a window $[\alpha, \alpha + \delta]$ constrained as follow:

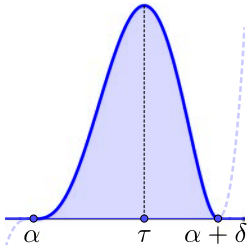

$$\begin{cases} P(\alpha) = 0 & \langle 1 \rangle \\ P(\alpha+\delta) = 0 & \langle 2 \rangle \\ P'(\alpha) = 0 & \langle 3 \rangle \\ P'(\alpha+\delta) = 0 & \langle 4 \rangle \\ P'(\tau) = 0 & \langle 5 \rangle \\ \int_\alpha^{\alpha+\delta} P(x)dx = 1 & \langle 6 \rangle \end{cases} \tag{8.1}$$

Figure 8.1: Quintic polynomial weight function

Constraints $\langle 1 \rangle$ and $\langle 2 \rangle$ implie: $P(x) = (x-\alpha)(x-(\alpha+\delta))(ax^3 + bx^2 + cx + d)$. In turn, this leads to a system of 4 equations (remaining constraints) and 4 unknowns which has an analytic

solution:

$$\begin{cases} a = \dfrac{60(2\alpha - 2\tau + \delta)}{\delta^5(\delta^2 + 5\delta(\alpha - \tau) + 5(\alpha^2 - 2\tau\alpha + \tau^2))} \\ b = \begin{cases} a\dfrac{5\tau^2 + 2\tau\alpha + \tau\delta - 7\alpha^2 - 7\alpha\delta - 2\delta^2}{4\alpha - 4\tau + 2\delta} & \text{if} \quad \alpha \neq \tau - \dfrac{\delta}{2} \\ \dfrac{30}{\delta^5} & \text{if} \quad \alpha = \tau - \dfrac{\delta}{2} \end{cases} \\ c = a(-3\alpha^2 - 3\alpha\delta - \delta^2) + b(-2\alpha - \delta) \\ d = -a\alpha^3 - b\alpha^2 - c\alpha \end{cases} \tag{8.2}$$

In addition, it is also necessary that $P(x) \geq 0, \quad \forall x \in]\alpha, \alpha+\delta[$ and $\tau \in [\alpha, \alpha+\delta]$. This condition is fulfilled for $\alpha \in [\tau - 3\delta/5, \tau - 2\delta/5]$. The flexibility of this weight function allows to optimize over α in its bounds to minimize E for a given τ. The width of the kernel δ allows to adapt to data disparities to guarantee a number of subjects used to compute the atlas. This is done using an iterative procedure similar to [Serag 2012a]. The age range is subsampled into a collection of potential ages and an ideal number of subjects n per atlas is chosen. Then, for each tentative age, if the number of subjects inside the window is less than n, δ is increased, otherwise it is reduced. Finally, smoothing is applied for a smooth transition between consecutive potential ages.

8.3 Longitudinal atlas creation method

We define a longitudinal (4D) atlas as a succession of 3D atlases each representing an average model at a given age. Those atlases are created using a generalized version of the method proposed by Guimond et al. [Guimond 2000] to provide an unbiased 3D atlas up to a rigid transformation and with variable weights. For each desired age, an initial reference is chosen among the subjects and the following steps are then iterated:

1. Registration: all the subjects are registered on the current reference image A_l.
2. Creation of the new reference A_{l+1}:
   i. Computation of $\bar{\theta}$ the weighted average of output transformations
   ii. Computation of $\bar{I}$ the weighted average of registered images
   iii. Application of $\bar{\theta}^{-1}$ to $\bar{I}$ to obtain A_{l+1}.

This creates a succession of reference images that are less and less biased by the choice of the first reference image and converges to an unbiased average model of the subjects namely an atlas. To be representative of a given time τ, it is necessary to give more importance to subjects with an age closer to τ. This is handled in the averaging processes described below.

8.3.1 Registration

At a given iteration l, each subject i is registered onto A_l in two steps using our block matching registration implemented in Anima [Anima] (see Figure 8.2).

1. An affine registration of the subject onto the current reference using [Commowick 2012b] that outputs an affine transformation a_i and a registered image $I_{i,a} = I_i \circ a_i$. The algorithm is initialized by a transformation determined using principal component analysis on the non-zero voxels of the two images as depicted in Appendix C. This makes the barycenters of the two images coincide and align and stretch their principal directions according to the corresponding eigenvalues. The output transformation is decomposed, using the method depicted in Chapter 7, into a robust rigid part r_i and a stretching part s_i.

2. A diffeomorphic registration of the registered image from the previous step onto the reference using [Commowick 2012a] that outputs a stationary velocity field (SVF) $\log(d_i)$ where d_i is the associated diffeomorphism through exponential map and a registered image $I_{i,d} = I_{i,a} \circ d_i$.

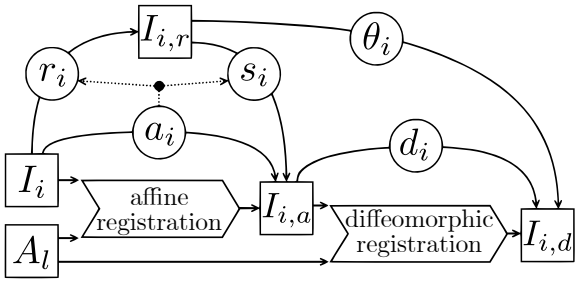

Figure 8.2: Two steps registration process of I_i on A_l: affine registration decomposed in a rigid part r_i and a stretching part s_i followed by a diffeomorphic registration (transformation d_i).

We therefore end up with a series of transformations that we can separate in two parts: a robust rigid part r_i and a deformation part $\theta_i = s_i \circ d_i$ that both takes into account global scalings and local differences. To further simplify θ_i and average them in a simple manner, we compute the SVF associated to s_i by taking its matrix logarithm and applying it to each spatial point of the image, thus obtaining a SVF $\log(s_i)$. The logarithm of the composition of s_i and d_i is then approximated through the BCH formula (see Section 2.4.3).

8.3.2 Creation of the new reference image

After the registration stage, we then compute the new average reference for the temporal point of interest from a set of SVFs $\{\log(\theta_i)\}$ with $\theta_i = s_i \circ d_i$ and a set of registered images $\{I_{i,d}\}$ with $I_{i,d} = I_i \circ r_i \circ \theta_i$. The debiasing transformation corresponding to the inverse of the log-Euclidean average of the transformations (Section 2.4.4) is computed:

$$\bar{\theta}^{-1} = \exp\left(-\sum_i w_i \log(\theta_i)\right) \tag{8.3}$$

The latter is then applied to the average of registered images: $\bar{I} = \sum_i w_i I_{i,d}$ to create A_{l+1}:

$$A_{l+1} = \bar{\theta}^{-1} \bar{I} \tag{8.4}$$

Doing so over several iterations ensures, similarly to [Guimond 2000], to obtain an unbiased atlas this time with respect to a rigid transformation. To compute the 3D atlas for a given age, the weights w_i are chosen using the weight function depicted in Section 8.2 and normalized such that they sum up to 1.

The fact that only the stretching part of the affine transformations has been taken into account leads to reference images that stay rigidly registered to the first one. This ensures the brain of the new reference image not to be outside of bounds when resampled in the geometry of the previous one. Also, given an image with a convenient orientation, taking this one as reference for all the sub-atlases allows them to also all have that very same pose.

8.4 Material, experiments and results

The proposed method has been tested on T1 images (size: $200 \times 200 \times 200$, voxel resolution: $1 \times 1 \times 1$ mm^3) from the C-MIND database [C-MIND]. 197 healthy subjects with ages ranging from less than a month to almost 19 years old have been selected after quality check.

8.4.1 Weight functions establishment

We have chosen the following parameters for the weight functions algorithm:

- Desired number of subjects per 3D atlas: $n = 25$
- Ages subsampling: 1000 equidistant timepoints between the minimum age (0.08 years old) and the maximum age (18.85 years old).
- Window size optimization: initial size of $\delta = 3$ years, then, at each iteration, the window width is updated such that the number of subjects in the window gets closer to n. Let $\delta_k(\tau)$ be the width of the window at timepoint τ and iteration k and $n_k(\tau)$ be the number of subjects in it. If $n_k(\tau) > n$, $\delta_{k+1}(\tau) = \delta_k(\tau) - 0.5 \times 0.8^k$ else, if $n_k(\tau) < n$, $\delta_{k+1}(\tau) = \delta_k(\tau) + 0.5 \times 0.8^k$, else $\delta_{k+1}(\tau) = \delta_k(\tau)$ (arbitrary choices). The smoothing step has been performed using Savitzky-Golay filter from *scipy.signal.savgol_filter*[1] with window smoothing length 101 and order 3 polynomial.

8.4.2 Temporal error evaluation

The main advantage of our weight function is the possibility of obtaining an asymmetric function to reduce temporal error through optimization over α. We thus compared our method (a) with a similar one (b) with a fixed $\alpha = T - \delta/2$ leading to symmetric weight functions around τ. The temporal errors for each method are shown in Table 8.1. Method (a) proves its ability to correct the temporal error allowing to construct well-timed atlases up to a day for almost half of the age range while it happens only for 2% using method (b).

method	median error	temporal error inferior to	
		1 day	1 week
proposed weight function (a)	0.0046	49.5 %	57.7 %
symmetric weight function (b)	0.0868	2.2 %	13.1 %

Table 8.1: Comparison of the median of the temporal errors (in years), percentage of timepoints where the error is less than 1 day and 1 week respectively for methods (a) and (b).

More information about the weight functions from methods (a) and (b) for each point of the age subsampling is available in Figure 8.3. The latter shows in addition the age distribution of the subjects but also the temporal error and the specificities of the weight function support with respect to age.

8.4.3 Pediatric atlas construction

We then conducted the creation of a pediatric atlas from the C-MIND [C-MIND] database. The parameters were set as:

- Number of main loop iterations: 8
- Age of the sub-atlases: 1, 1.5, 2, 2.5, 3, 4.5, 6.5, 11 and 16 years old. Ages for which the temporal error was less than a day.
- Reference image: Same first reference image for the construction of all 3D sub-atlases. This reference is a pre-built atlas with a convenient orientation: the mid-sagittal plane has been ensured to be vertical in axial view by using the algorithm in [Prima 2002] and the anterior commissure - posterior commissure (AC-PC) line is roughly horizontal in sagittal view.

[1] https://www.scipy.org/index.html

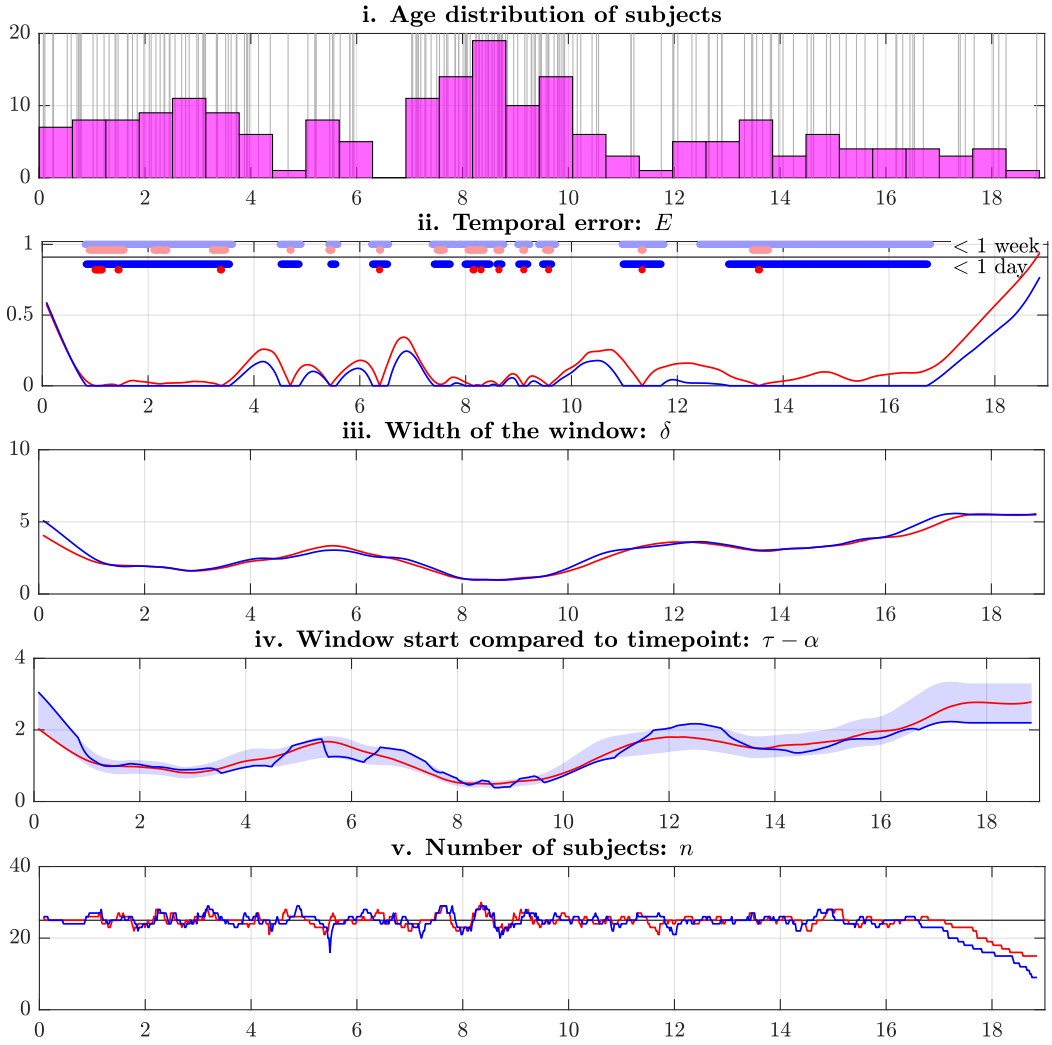

Figure 8.3: Age distribution of subjects in years (i), comparison of weight functions from methods (a) in blue and (b) in red in terms of: temporal error (ii), width of the window that supports the weight function (iii), position of the start of the window relatively to the timepoint: $\tau - \alpha$ (iv) with the interval of authorized values: $\left[\frac{2\delta}{5}, \frac{3\delta}{5}\right]$ in light blue for method (a), and number of subjects (iv).

- Order of the BCH used for transformations composition: 2

We present the computed atlases in Figure 8.4 together with the age of the subjects used for their construction together with the weights that modulate their contributions.

Visual checkup on this longitudinal atlas explicits quick general brain growth in the early stages of life until a stabilization around 5 years old except for the antero-posterior direction that continues until the older ages. Thanks to our robust rigid extraction, all temporal atlases are well centered on their barycenters and their sagittal planes are well aligned.

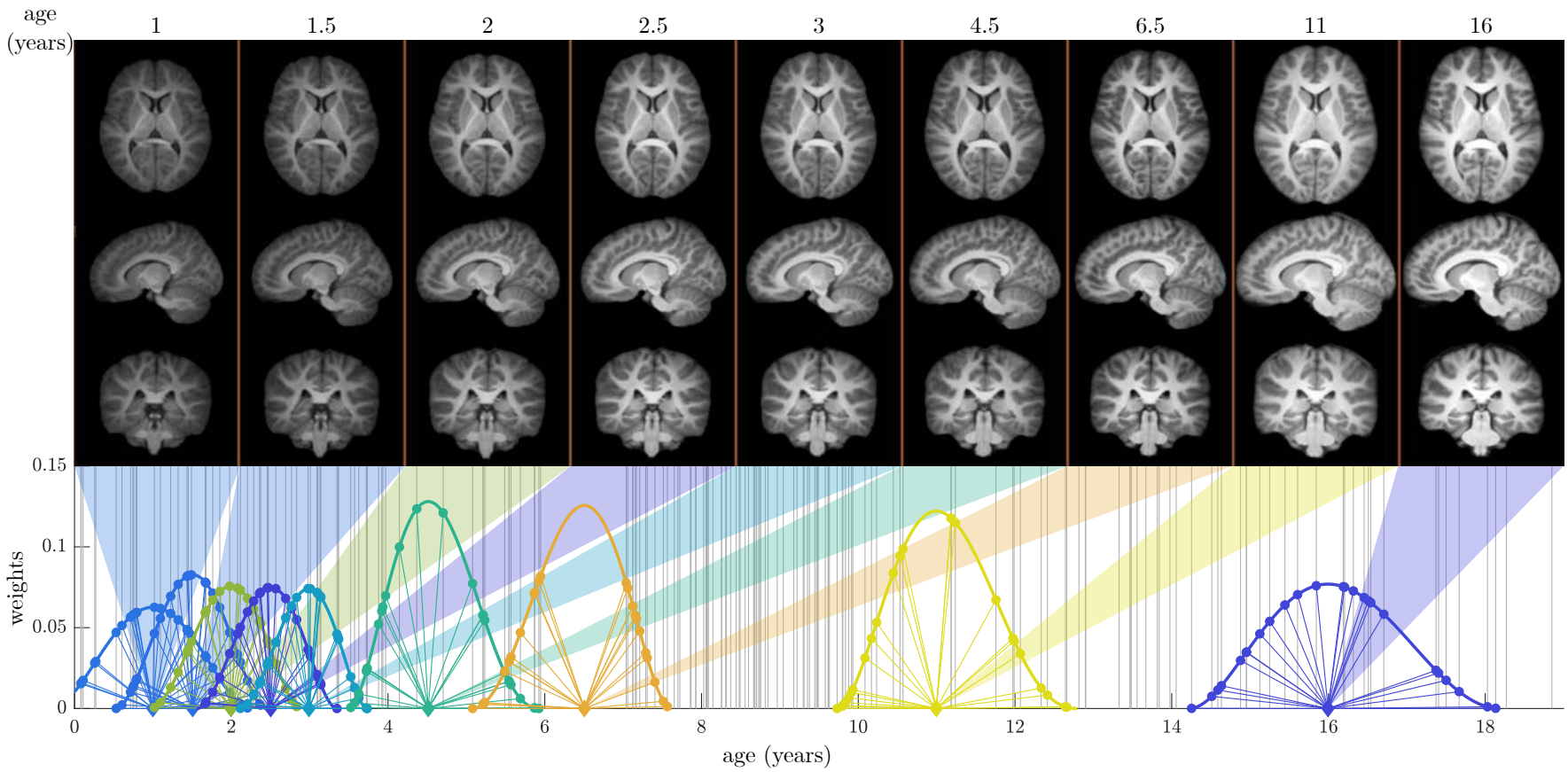

Figure 8.4: Longitudinal atlas for various ages together with the weights associated to each subjects for each sub-atlas.

8.5 Conclusion

We presented a longitudinal atlas creation method using a generalized version of the algorithm from [Guimond 2000]. It takes advantages of the log-Euclidean framework and the BCH formula to produce individual age atlases unbiased up to a rigid transformation giving the opportunity to highlight global changes and local deformations in the atlas. To be representative of a given age, we introduced a quintic polynomial weight function to modulate the influence of each subject. Through its flexibility (potential asymmetry), it ensures a large choice of ages on which the associated atlas is not temporally erroneous. Finally, by denoting N the number of subjects and L the number of iterations in the main loop of the algorithm, our method necessitates only a number of registrations equal to LN (M being in practice much smaller than N) while numerous atlas creation methods require this number to be in $\mathcal{O}(N^2)$.

Chapter 9

Iterative centroid

Contents

Online atlasing, i.e. incrementing an atlas with new images as they are acquired, is key when performing studies on databases very large or still being gathered. We propose to this end a new diffeomorphic online atlasing method without having to perform again the atlasing process from scratch. New subjects are integrated following an iterative procedure gradually shifting the centroid of the images to its final position, making it computationally cheap to update regularly an atlas as new images are acquired (only needing a number of registrations equal to the number of new subjects). We evaluate this iterative centroid approach through the analysis of the sharpness and variance of the resulting atlases, and the transformations of images, comparing their deviations from a conventional method. We demonstrate that the transformations divergence between the two approaches is small and stable and that both atlases reach equivalent levels of image quality.

9.1 Introduction

In this chapter, we focus on a different definition of an atlas where we do not for now consider the temporal dimension. An atlas is therefore an average model of the brain both in terms of shape and intensity. It is a powerful tool to understand brain variability, to compute statistics on populations [Whitcher 2007] or to segment regions [Cabezas 2011]. The interested reader may look at Chapter 4 for a presentation of some of the most common atlasing methods. Those requires a large number of heavy computations (registrations, transformation compositions...) that increases with the number of subjects (linearly or even quadratically), their computational cost can thus be prohibitive.

Historically databases used for atlas construction were small (about 50 to 100 subjects at most). However, there is a recent trend for the creation of large databases, out of which great atlases depicting the variability of the population across the life span could be inferred. Among these databases, the human connectome project (HCP [HCP], now completed) is made of around 1200 subjects of the same age range [Van Essen 2012]. Even bigger databases are currently being constituted from more subjects (up to 100,000 in the UK biobank [Miller 2016]) or across the life span (HCP lifespan) on which researchers already wish to start studies. This

causes a problem as the databases are still being gathered and thus the atlas needs to be updated. With current methods, the atlas needs to be recomputed each time new acquisitions are added which is very costly. New methods are therefore needed to allow online atlasing, i.e. the capacity of incrementing atlases with new images as they come without having to perform again the whole atlas construction, as opposed to the above-mentioned direct atlasing.

We propose a new method that considers atlasing from a different angle. Inspired by the notion of centroid for a set of points in a Euclidean space and the way it can be constructed following an iterative procedure, [Cury 2014] derived a diffeomorphic atlas construction method working on surfaces while [Noblet 2012]presented an approach for images. We propose here a generalization of this iterative centroid method for image atlasing where the centroid (atlas) is updated gradually as new images are incorporated. The online aspect of this technique has several advantages: when a new images arrives, its integration does not necessitate to restart the atlasing process from scratch. Also, it only requires one registration per new image making it computationally cheap. Benefiting from the log-Euclidean framework for diffeomorphisms from [Arsigny 2006a], the method allows the production of a diffeomorphic atlas unbiased up to a linear transformation (rigid or affine at the choosing of the user).

We first introduce the iterative centroid method and its specificities for image atlasing in Section 9.2. Then in Section 9.3, we present experiments comparing how the atlases, built using direct atlasing (here a modified version of the [Guimond 2000] method, developed in [Legouhy 2019] and detailed in Chapter 8) and with the method proposed here, differ from each other as they include more and more subjects. We demonstrate with three different metrics that the iterative centroid and direct atlases diverge only by a small amount in terms of transformations and that their intensity based features do not vary.

9.2 Method

9.2.1 Theoretical background

As exposed in Chapter 3, considering the registration of an image J onto an image I, we denote by $\tilde{J}$ the registered image and T the transformation operating on coordinates x used to resample J onto I: $I(x) \sim \tilde{J}(x) = J \circ T(x)$.

Diffeomorphisms are widely used in non-linear registration because of their interesting properties: differentiability, bijectivity and differentiability of the inverse map. In the SVF framework presented in Section 2.3.3, one can parametrize a diffeomorphic transformation T between two images by a stationary velocity field integrated over time. It generates $\gamma(t)$, a diffeomorphic path between Id and T such that $\gamma(0) = Id$ and $\gamma(1) = T$. As depicted in Section 2.4.3, for such diffeomorphisms, operations are defined as their Euclidean counterparts on the SVFs [Arsigny 2006a]. One of interest is the power of a diffeomorphism defined as $T^\alpha = \gamma(\alpha) = \exp(\alpha \log(T))$. In the following, all non-linear transformations are assumed to be diffeomorphisms parameterized with SVFs. Additionally, given 2 SVFs v and w, it is possible to approximate the logarithm of their composition while avoiding a very costly logarithm computation using the BCH formula as presented in Section 2.3.3.

9.2.2 Iterative centroid atlas construction

In a Euclidean space Ω, the centroid b_n of a set of points $\{x_1, \dots, x_n\}$ is defined as $b_n = \arg\min_{y \in \Omega} \sum_{i=1}^{n} \|y - x_i\|^2$. A direct solution is $\frac{1}{n}\sum_{i=1}^{n} x_i$ but an iterative approach is also imaginable. Starting from $b_1 = x_1$, we can use the recursion:

$$b_{k+1} = \frac{k}{k+1} b_k + \frac{1}{k+1} x_{k+1} \tag{9.1}$$

As depicted in [Cury 2014], one can extend this formulation to the Riemannian case for surfaces by using the generalization of the notion of straight line through geodesics. The updated

centroid b_{k+1}, in that case, is on the geodesic linking b_k and x_{k+1}, at $\frac{1}{k+1}$ times the distance from b_k.

We define our iterative centroid atlasing, following the same spirit, on images and diffeomorphisms parameterized by SVFs. Thereafter we assume that the registration of an image I onto an atlas A provides two transformations L and T, where L is linear and T is a diffeomorphism, so that $A \sim I \circ L \circ T$. Generalizing Equation 9.1 to a set of images $\{I_1, \dots, I_n\}$, we start from $A_1 = I_1$ and get:

$$A_{k+1} = \frac{k}{k+1} A_k \circ T_{k+1}^{-\frac{1}{k+1}} + \frac{1}{k+1} I_{k+1} \circ L_{k+1} \circ T_{k+1}^{\frac{k}{k+1}} \tag{9.2}$$

The atlasing scheme is illustrated Figure 9.1. We apply to A_k a transformation situated at $\frac{1}{k+1}$ of the distance from the identity to T_{k+1}^{-1} along the geodesic. We also apply to I_{k+1}, in addition to the linear transformation, a transformation situated at $\frac{k}{k+1}$ of the distance from the identity to T_{k+1} along the geodesic. Also, A_k is made from k images so a weight $\frac{k}{k+1}$ is affected to its intensities while I_{k+1} intensities get a weight $\frac{1}{k+1}$. At the end, those two images are transformed and weighted according to their contribution to the atlas.

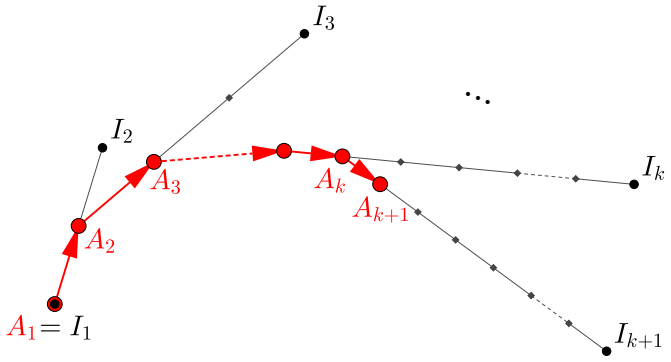

Figure 9.1: Shift of the centroid as new images are incorporated.

Unlike [Cury 2014], we are dealing with images and therefore interpolations on a voxel grid to reconstruct a new image after a transformation. This resampling step has to be avoided as much as possible to keep a maximum of details. To this end it is preferable not to use A_k (already a resampled image) when constructing A_{k+1}, but instead to operate on the initial images using transformation compositions such that each image undergoes only one resampling. This is achieved by expressing the sequence $(A_k)_{k\in\mathbb{N}}$ using only the initial images $\{I_j,\ j = 1, \dots, k\}$. Rearranging Equation 9.2, the following formulation emerges:

$$A_{k+1} = \frac{1}{k+1} \left(\sum_{j=1}^{k} \left(I_j \circ L_j \circ \Theta_{j,k} \circ T_{k+1}^{-\frac{1}{k+1}} \right) + I_{k+1} \circ L_{k+1} \circ T_{k+1}^{\frac{k}{k+1}} \right) \tag{9.3}$$

Where $\theta_{j,k}$ is the non-linear part of the transformation bringing I_j onto A_k. There are k compositions using BCH to perform at iteration k which correspond to the update of the transformations $\theta_{j,k}$ for $j \leq k$.

Initialization

One can start at iteration 1 by initiating $A_1 = I_1$ and $\theta_{1,1} = Id$. However, a very interesting point of the method is the possibility to complement an already existing atlas A_p constituted of p images as long as it can be written as $A_p = \frac{1}{p} \sum_{j=1}^{p} I_j \circ L_j \circ T_j$. To do so, we simply assign $\theta_{j,p} = T_j,\ \forall j \leq p$.

Iterative procedure

At the end of iteration k, we have, for each $j \leq k$, transformations $\theta_{j,k}$ that map images I_j onto the atlas A_k: $A_k \sim I_j \circ L_j \circ \theta_{j,k}$. To build A_{k+1} from these, we do the following:

1. we register I_{k+1} onto A_k: $A_k \sim I_{k+1} \circ L_{k+1} \circ T_{k+1}$ (1 registration)
2. For $j \leq k$, we compute the updated $\theta_{j,k+1}$ as $\theta_{j,k+1} = \theta_{j,k} \circ T_{k+1}^{-\frac{1}{k+1}}$ (k BCH)
3. We assign $\theta_{k+1,k+1} = T_{k+1}^{\frac{k}{k+1}}$
4. Finally we build $A_{k+1} = \frac{1}{k+1} \sum_{j=1}^{k+1} I_j \circ L_j \circ \theta_{j,k+1}$.

9.2.3 Unbiased atlas construction

So far, we have only assumed that the registration produced a linear and a non-linear part. Going in more details, let us now assume that this registration can be written $A \sim I \circ R \circ S \circ D$ where: $R \circ S$ is an affine transformation decomposed into a rigid part R and a stretching part S, and D is a diffeomorphism. Herebefore, by taking $L = R \circ S$ and $T = D$ i.e. L encapsulating all the linear transformations and T only local displacements, the method will lead - similarly to [Guimond 2000] - to an atlas unbiased up to an affine transformation. On the other hand, if we take $L = R$ and $T = S \circ D$ i.e. L only considering rigid motion while T encapsulating both growth and local displacements, the method will lead to an atlas unbiased up to a rigid transformation (useful typically for longitudinal studies).

9.3 Experiments and results

9.3.1 MRI database

For our experiments, we have used T1 weighted preprocessed images (brain extracted) from 100 subjects randomly chosen among the Human Connectome Project [HCP] database (for more details, see [Van Essen 2012]). The size of the images is $260 \times 311 \times 260$ with a voxel size of 0.7 mm isotropic.

9.3.2 Implementation details

9.3.2.1 Registration

Our method is agnostic to the registration used. We performed registrations in two steps using symmetric block matching algorithms from Anima [Anima].

1. An affine registration that outputs a transformation matrix B which is decomposed through polar decomposition into a rigid part R and a stretching part S as depicted in [Legouhy 2019].
2. A diffeomorphic registration that directly outputs the SVF of the diffeomorphism $\log(D)$ linking the two images. This allows to take advantage of the log-Euclidean framework without logarithm computation (see Chapter 2.4.3).

We chose to compute atlases up to a rigid transformation. Therefore, the linear transformation L is rigid: $L = R$ and the non-linear transformation is the combination of stretching and local displacements: $T = S \circ D$.

9.3.2.2 Transformation composition

Compositions of two diffeomorphisms are performed on their SVFs using order 2 BCH. To compose a linear transformation L and a SVF, we first apply $\log(L)$ to the real coordinates of an image grid to transform it into an SVF and then compose using 2^{nd} order BCH.

9.3.3 Comparison between iterative centroid and direct atlasing

In the following experiments, we evaluate the quality of the iterative centroid atlas and its divergence with respect to direct atlasing, here a method developed in [Legouhy 2019] available in Anima [Anima-Scripts] based on [Guimond 2000]. For both methods, we used the same registration and composition tools with the same parameters. Starting from an atlas built with 50 images using direct atlasing, we added one by one the 50 other images using our online atlasing. We then compared the direct atlases computed at several steps with the online ones using three metrics.

9.3.3.1 Divergence

Both methods output linear and non-linear transformations (denoted T_j for online atlasing and $\tilde{T}_j$ for direct atlasing) mapping each image onto the atlas. We first propose to evaluate the divergence between the two atlases A and $\tilde{A}$ by an image δ defined from the transformations:

$$\delta\left(A, \tilde{A}\right) = \frac{1}{n}\sum_{j=1}^{n}\sqrt{\sum_{d=1}^{3}\left(T_{j,d} - \tilde{T}_{j,d}\right)^2} \tag{9.4}$$

where d indexes the three components in space. This measure has the advantage of being agnostic to edge issues that can happen in intensities comparisons.

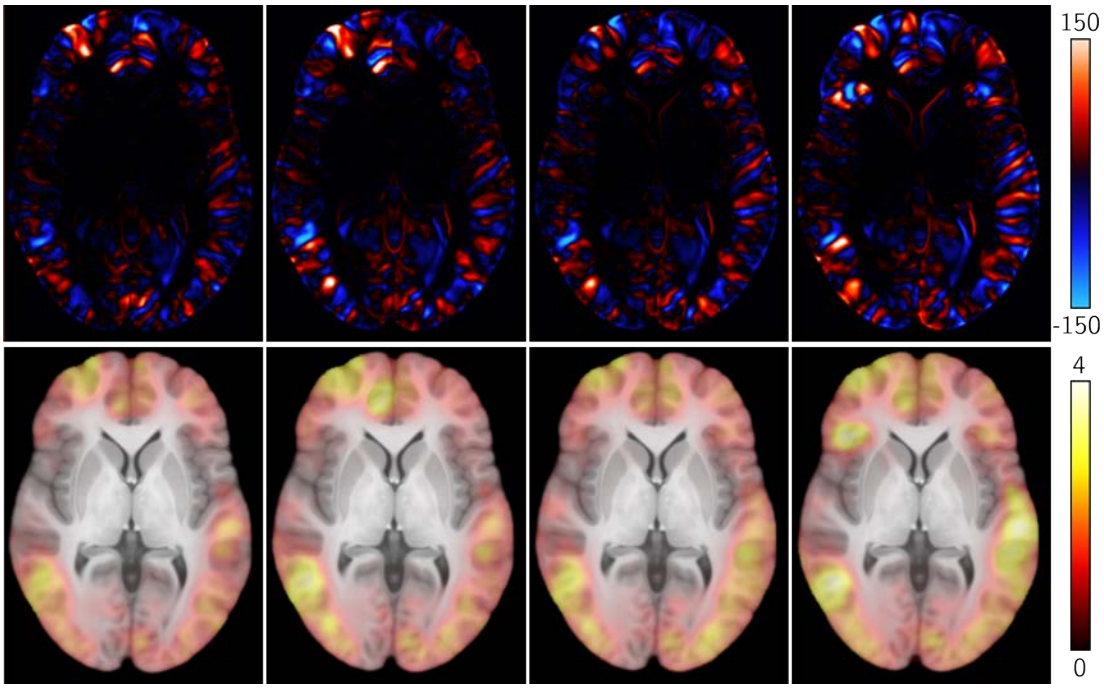

Figure 9.2: From left to right atlases with 60, 70, 80 and 100 images. Top: intensity differences between iterative centroid and direct atlases (knowing that the intensities are comprised between 0 and 1046). Bottom: atlases from iterative centroid method overlaid with divergence measure δ.

Figure 9.2 presents a qualitative view of the evolution of the differences between the direct and online atlases with respect to the number of subjects. We observe that most of the differences increase with the number of added subjects and occur in the cortical areas while central structures of the brain are spared. Figure 9.3 gives quantitative plots over the brain of the divergence measures. It suggests that the divergence tends to grow (from a median of 0.777 mm for 60 images, to 1.095 mm for 100) but at a slow pace that decreases (+0.153 mm between 60 and 70 images but only +0.025 mm between 90 and 100).

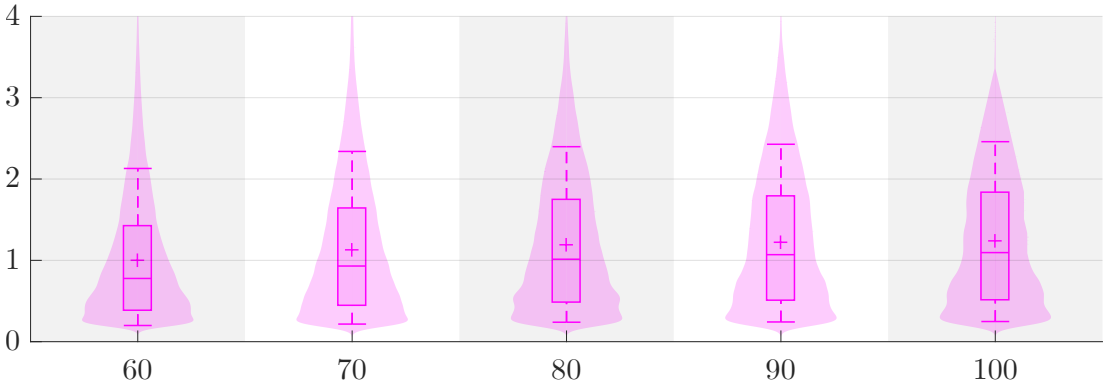

Figure 9.3: Boxplots and violin plots of the divergence δ between the atlases (restrained to the union of the masks) with 60, 70, 80, 90 and 100 images.

9.3.3.2 Iconic evaluations

The second part of the evaluation assesses the quality of the atlases based on image intensities. We evaluate first the atlas standard deviation across subject images after transformation on the atlas, the transformations being constructed differently upon the atlasing method. This measure allows to quantify how well the images are aligned after atlas construction (the lower the standard deviation, the better):

$$\mathrm{sdis}(A) = \sqrt{\frac{1}{n}\sum_{i=j}^{n} (I_j \circ L_j \circ T_j - A)^2} \tag{9.5}$$

For better interpretation, we normalized sdis by the average of the intensities of the atlases from the two methods to create sdis_n.

In addition, we propose a measure of the sharpness of the atlases. Given $N(i)$, a patch around a voxel i of an image A, we define a local measure of the sharpness at voxel i, $\mathrm{sha}(A(i))$, as the standard deviation of the patch normalized by its average:

$$\mathrm{sha}(A(i)) = \frac{\mathrm{sd}_{N(i)}(A)}{\mathrm{mean}_{N(i)}(A)} \tag{9.6}$$

In our experiments, we chose a patch of diameter 5 voxels. We present in Figure 9.4 a quantitative view over voxels inside the brain mask of these two iconic measures with respect to the number of images in the atlas. These results show that both methods output atlases that are very similar in terms of image quality. The sharpness remains equivalent for both methods independently of the number of images added. sdis_n increases only between 60 and 70 images and is then stable, but the evolution and values are the same for both atlas construction methods.

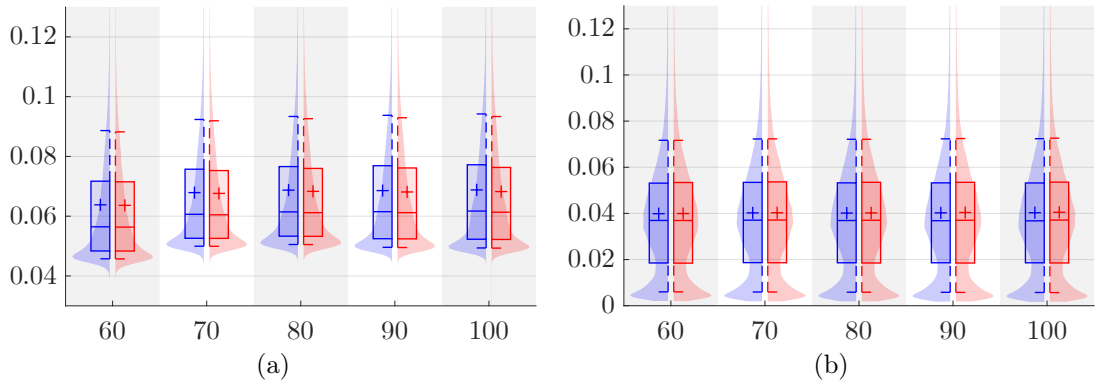

Figure 9.4: Boxplots and violin plots of inter-subjects normalized standard deviations sdis_n (a) and sharpness sha (b) for atlases (restrained to the union of the masks) with 60, 70, 80, 90 and 100 images. Blue: iterative centroid. Red: direct atlasing.

9.3.3.3 Computational cost

In both compared methods, there are two main sources of time consumption which are the non-linear registrations and the transformation compositions through BCH. As an indication, using a computer with 2×20 cores Intel Xeon Processor E5-2660 v3 2.60GHz, for images of dimension $160 \times 256 \times 190$ ($1 \times 1 \times 1$ mm), it takes about 213 seconds to compute a non-linear registration and 16 seconds to perform a transformation composition through 2^{nd} order BCH.

Let us consider we already have a pre-existing atlas made of k images. We are looking for a measure of the cost of completing this atlas with new images so that it contains a total of n images (including the k initial ones). We have compared the two options evaluated earlier to perform this task:

- **Direct method:** Whatever the previous atlas, the new one has to be built from scratch. Let p be the number of iterations of the main loop. The method requires:
  - pn non-linear registrations.
  - pn transformation compositions through BCH corresponding to the composition of the affine and the non-linear transformations from the registrations (only for an atlas up to a rigid transformation).
- **Iterative centroid method:** Using the pre-existing atlas, the method requires:
  - $n - k$ non-linear registrations.
  - $(n-k) + \sum_{i=k+1}^{n} i = \frac{1}{2}(n-k)(n+k+3)$ transformations compositions through BCH. The first part corresponds to the composition of the affine and the non-linear transformations from the registrations. The second corresponds to the update of the θ transformations (only for an atlas up to a rigid transformation).

Now we showcase two examples that give an idea of the strengths and weaknesses of both methods in terms of computational cost:

1. We already have in our possession 300 images and we want to build an atlas from it. The amount of non-linear registrations and BCH computations as well as an indicative processing time for both methods necessary to build this atlas is presented in Table 9.1.

method	direct atlasing		iterative centroid
main loop iterations	4	8	
number of non-linear registrations	1200	2400	300
number of BCH computations	1200	2400	45450
indicative processing time (hours)	76.3	152.7	219.8

Table 9.1: Number non-linear registrations, number of BCH computations and indicative processing time to create an atlas of 300 images from scratch using iterative centroid and a direct atlasing with 4 and 8 main loop iterations.

In this configuration, where a single atlas in built from scratch, direct atlasing is the best suited method.

2. We now have a pre-existing atlas made of 200 images and, acquisitions being gathered gradually, we want to update this atlas every 10 new images until we have a final amount of 300. The amount of non-linear registrations and BCH computations as well as an indicative processing time for both methods necessary to update the previous atlas is presented in Figure 9.5.

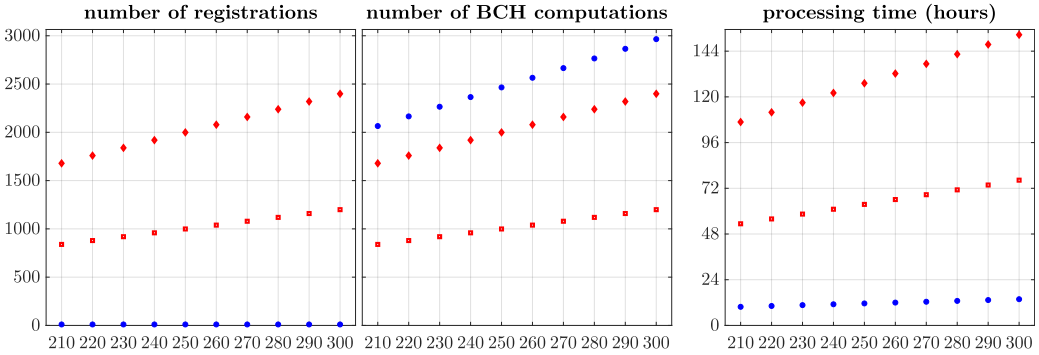

Figure 9.5: Number non-linear registrations, number of BCH computations and indicative processing time to update the atlas at each step (every 10 new images from 200 to 300) using iterative centroid (blue) and a direct atlasing (red) with 4 (■) and 8 (♦) main loop iterations. Abscissa represents the number of images of the atlas at each step.

In this configuration, where an atlas in updated gradually as new images arrive, iterative centroid is the best suited method. Indeed, updates take only from 9.77 hours at first step to 13.77 at the last (+0.44 hours at each step) for iterative centroid. In comparison, even for only 4 main loop iterations (which is not much), it takes from 53.37 hours for the first step to 76.27 hours for the last (+2.54 hours at each step) for the direct atlasing method.

To sum up, in terms of computational cost, direct atlasing shows better results when it comes to build a single atlas from scratch. On the other hand, the iterative centroid method performs better in case of an atlas being updated gradually. The more images there is in total and the shorter the steps are, the better iterative centroid behaves compared to its direct counterpart.

9.4 Conclusion

We have presented an online atlasing method that allows the incorporation of new images into an existing atlas without having to restart the atlasing process from the beginning. Based on an iterative centroid process, this approach only necessitates one registration per new image. We observed that the divergence between our method and direct atlasing using the same tools is pretty negligible, localized in cortical areas and tends to grow but at a slow and decreasing pace. Also, the obtained atlases from both approaches have shown no differences in terms of image quality. The trend being at large, growing databases, the proposed online atlasing method offers an interesting tool to update an atlas at reasonable computational cost as new images arrive. Finally, we derived a construction method up to either an affine or a rigid transformation. This makes the method especially eligible for longitudinal atlasing as a future work, simply by adapting the weight of each image in Equation 9.3.

Part IV

Conclusion

Chapter 10

Contributions

The contributions highlighted in this manuscript have lead to several international peer-reviewed journal and conferences papers. The list of publications that arose form this PhD is the following:

Journal papers

NeuroImage: Clinical 2019

Changes in brain perfusion in successive arterial spin labeling MRI scans in neonates with hypoxic-ischemic encephalopathy

Maïa Proisy[a,b,*], Isabelle Corouge[a], **Antoine Legouhy**[a], Amélie Nicolas[b], Valérie Charon[b], Nadia Mazille[c], Stéphanie Leroux[c], Bertrand Bruneau[b], Christian Barillot[a] and Jean-Christophe Ferré[a,b]

[a] *Univ Rennes, Inria, CNRS, INSERM, IRISA, Empenn ERL U-1228, F-35000 Rennes, France*
[b] *CHU Rennes, Radiology Department, F-35033 Rennes, France*
[c] *CHU Rennes, Neonatology Department, F-35033 Rennes, France*

PLOS ONE 2020

Regional brain development analysis through registration using anisotropic similarity, a constrained affine transformation

Antoine Legouhy[a,*], Olivier Commowick[a], Maïa Proisy[a,b], François Rousseau[c] and Christian Barillot[a]

[a] *Univ Rennes, Inria, CNRS, INSERM, IRISA, Empenn ERL U-1228, F-35000 Rennes, France*
[b] *CHU Rennes, Radiology Department, F-35033 Rennes, France*
[c] *IMT Atlantique, LaTIM U1101 INSERM, UBL, Brest, France*

Conference papers

ISMRM 2018
(abstract + poster)

Anisotropic similarity , a constrained affine transformation : Application to brain development analysis

Antoine Legouhy[a,*], Olivier Commowick[a], François Rousseau[b] and Christian Barillot[a]

[a] *Univ Rennes, Inria, CNRS, INSERM, IRISA, Empenn ERL U-1228, F-35000 Rennes, France*
[b] *IMT Atlantique, LaTIM U1101 INSERM, UBL, Brest, France*

ISBI 2019
(4 pages paper + oral presentation)

Unbiased longitudinal brain atlas creation using robust linear registration and log-Euclidean framework for diffeomorphisms

Antoine Legouhy[a,*], Olivier Commowick[a], François Rousseau[b] and Christian Barillot[a]

[a] *Univ Rennes, Inria, CNRS, INSERM, IRISA, Empenn ERL U-1228, F-35000 Rennes, France*
[b] *IMT Atlantique, LaTIM U1101 INSERM, UBL, Brest, France*

MICCAI 2019
(8 pages paper + poster)

Online atlasing using an iterative centroid

Antoine Legouhy[a,*], Olivier Commowick[a], François Rousseau[b] and Christian Barillot[a]

[a] *Univ Rennes, Inria, CNRS, INSERM, IRISA, Empenn ERL U-1228, F-35000 Rennes, France*
[b] *IMT Atlantique, LaTIM U1101 INSERM, UBL, Brest, France*

I summarize in the following sections these contributions.

10.1 Unbiased longitudinal brain atlas creation using robust linear registration and log-Euclidean framework for diffeomorphisms

This contribution concerns the development of an unbiased spatio-temporal atlas creation method using a template-based approach inspired by [Guimond 2000]. The topology-preserving behavior of the transformations involved is ensured through the parametrization of diffeomorphisms by stationary velocity fields (SVF), thus allowing log-Euclidean statistics and easy composition using the Baker-Campbell-Hausdorff (BCH) formula. This results in a set of 3D sub-atlases that both account for global changes and local diffeomorphic deformations. The concern of the temproal accuracy of these atlasses is also adressed by introducing a flexible quintic polynomial weight function to modulate the influence of each subject. Finally, this method is computationaly reasonable since its cost grows linearly with the number of images. The method has been experimented on a set of 197 images from the C-Mind database [C-MIND] to build a spatio-temporal atlas with timepoints between 0 and 18 years of life.

The code provision for this atlas creation pipeline is freely available in [Anima-Scripts].

10.2 Changes in brain perfusion in successive arterial spin labeling MRI scans in neonates with hypoxic-ischemic encephalopathy

This study, mainly conducted by Maïa Proisy was the occasion to produce a more applicative work at the expense of major methodological contributions. It essentially consisted in adapting pipelines in order to process a newborn population incompatible with tools designed for adult subjects. The challenge was to be able to properly perform registrations, brain extraction, segmentation and perfusion quantification on some twenty neonates suffering from hypoxic-ischemic encephalopathy, that have been scanned twice at 4 and 11 days of life. This task has

been raised through notably the creation of specific atlases allowing to link ALBERTs [ALBERTs] segmentation to ours, despite initial incompatibilities.

10.3 Online atlasing using an iterative centroid

This contribution concerns an online atlasing method that allows to update an existing atlas as new images arrive without having to restart the atlasing process from scratch. It is based on an iterative centroid process. This approach only necessitates one registration per new image. Also, it takes advantages of the log-Euclidean framework. This method has been tested on images from the HCP database [HCP] by updating an atlas of 50 subjects until it reaches 200. The result has been compared to the above-mentioned template-based method using the same tools showing only a subtle divergence tending to grow but at a slow and decreasing pace. Also, the obtained atlases from both approaches have shown no differences in terms of image quality (notably sharpness). The proposed method is well adapted to the trend of large, growing databases since a gradual update can be done a reasonable computational cost. Also, this iterative centroid approach embeds the possibility to produce atlases unbiased up to a rigid transformation, which makes it eligible, in a future work, for a spatio-temporal extension only necessitating a weighting adjustment.

The code provision for this atlas creation pipeline is freely available in Anima-Scripts].

10.4 Regional brain development analysis through registration using anisotropic similarity, a constrained affine transformation

We have finally presented a method that allows the extraction of regional and global scaling factors along arbitrary chosen orthogonal directions through linear registration. This is done through registration using a special kind of transformation: the anisotropic similarity which is an affine transformation with constrained directions of scaling. The main contribution is the introduction of this transformation set and the optimization over it to find the optimal anisotropic similarity that best matches two sets of paired points. The interest of this transformation has been illustrated through regional registrations using anisotropic similarity of 308 subjects onto a common reference image on which the constrained directions of scaling of our choosing have been fixed. Those subjects were selected from 3 different databases (dHCP [dHCP], C-MIND [C-MIND] and ASLpedia [ASLpedia]) and cover an age range from 0 to 19 years old. The extraction of their scaling factors allowed regression of those over age, and thus the modeling of the anisotropic growth of various regions of the brain. The robustness of the method with respect to the choice of the reference image has been challenged and showed a good stability. A nice interest of the method is the possibility to create informative and easily interpretable graphical representations of the regional anisotropic brain growth.

The code provision for this scaling factor extraction pipeline is freely available in [Anima-Scripts].
The anisotropic similarity registration algorithm is implemented in [Anima].

Chapter 11

Perspectives

Finally, I present in this chapter some perspectives coming from this work that I believe should be studied at a short or longer term.

11.1 Variants of the iterative centroid approach

The online aspect of the iterative centroid atlasing method developed in Chapter 9 is quite promising considering the trend of large datasets with new images being released regularly.

The presented version however does not account for the temporal dimension. Yet, the formulation does not forbid the incorporation of a weight function modulating the weight of the subjects according to their age. This spatio-temporal extension might be a bit tricky at first in order not to be entangled with the already existing weights inherent to the approach, but still pretty straightforward.

Also, we presented a version that is based on the SVF parametrization for diffeomorphisms, mainly for computational reasons. Yet, since this method is designed for the case of images that arrive gradually, it might not be that much of a burden to perform an heavy registration once in a while. Given that, one can consider a more theoretically ambitious version, as [Cury 2014] did for surfaces, through the parametrization of the diffeomorphisms following the LDDMM framework. They are also other versions of the iterative centroid algorithm proposed in [Cury 2018] that would be worth translating to images. This includes a more parallelizable hierarchical one that could achieve faster results when adding more than one image at a time.

11.2 Application of the spatio-temporal atlasing method

The food source for the creation of spatio-temporal atlases of the developing brain has recently considerably increased thanks notably to the extensions of the Human Connectom Project [Harms 2018] that are the HCP Lifespan Babies[1] (BCP) and the HCP Lifespan in Development[2] (HCP-D). The BCP aims at including 500 children between 0 and 5 years old. This is a very interesting age range as it cover most of the postnatal brain maturation. In addition, 385 of the subjects undergo a longitudinal follow up (4 to 6 repetitions). This might be the chance to experiment techniques involving the regression of individual longitudinal brain growth models in the same vein as in [Durrleman 2009].

Focus has been made, during this thesis, on developmental data but it could be interesting to apply the same methods on aging brains using e.g. the HCP Lifespan in aging[3] (HCP-A) that includes 1200+ subjects amongst which 600+ have undergone a follow-up about 24 month later.

Also we only evoked anatomical atlases but one can translate the creation process to other modalities such as diffusion [Pontabry 2013].

[1] BCP: [Howell 2019] - https://www.humanconnectome.org/study/lifespan-baby-connectome-project
[2] HCP-D: [Somerville 2018] - https://www.humanconnectome.org/study/hcp-lifespan-development
[3] HCP-A: [Bookheimer 2019] - https://www.humanconnectome.org/study/hcp-lifespan-aging

11.3 Application and upgrades of the scaling factor extraction method

11.3.1 Clinical applications

As evoked in the discussion Chapter 5, understanding the growth along chosen directions of areas of the brain may have some interesting clinical applications.

Those measurements that are performed at the scale of a ROI could be pertinent to characterize the brain deformations induced by plagiocephaly, also known as *flat head syndrome*, that is an early asymmetrical distortion of the skull. Indeed, volumetric studies are irrelevant in that case since the amount of biological material is the same for patient and control, only the disposition differs. The current assessments are the ones depicted in [Collett 2012] are somewhat ad-hoc and human dependent. One can imagine the construction of an age-adapted control atlas onto which ROIs are segmented, and three orthogonal directions are chosen for each through considerations that are yet to be defined. Then, by registering patients through anisotropic similarity registrations constrained in scaling by those directions, one can then extract reliable and automatic measurements that could be used as biomarkers.

11.3.2 Polyaffine upgrade

In the current version, the anisotropic similarity registration of the ROIs is initialized by an isotropic similarity on the whole brain. This choice has been motivated by the fact that the composition of an isotropic and an anisotropic similarity yield an anisotropic similarity, which is not the case if we replace the first one by an affine transformation. Yet this initialization may fail to even roughly align small structures. This is a critical issue for the anisotropic similarity registration of the ROI that follows.

An interesting implementation would be to take advantage of the polyaffine framework from [Arsigny 2009]. Similarly to the work in [Commowick 2008], one can imagine to directly perform a piecewise anisotropic similarity registration of all the ROIs (one transformation by ROI) with a log-Euclidean regularization in between, thus allowing them to *slide* in relation to each other. With that extra flexibility, one can expect great improvement on the way small structures are treated.

11.4 Consistent processing when dealing with developing brains acquired differently

Those are more open questions for which I have no real insight on how to approach them but that will definitely deserve looking at in the future to see their influence.

11.4.1 Intensity normalization

Anatomical MR image intensities only have a qualitative meaning. There is a massive variability due notably to scanner specificities and differences in the choice of the acquisition parameters. Furthermore, two images taken at different times of a single patient, in the same machine, show differences in terms of intensities that are not negligible. To cope with this, normalization techniques using i.e. histogram matching such as in [Nyúl 1999, Nyúl 2000] have been developed. However, a hidden hypothesis is those approaches is that the repartition of the tissue composition is roughly the same between the images, which is obviously not the case when working with brains of different maturation. Given that, it is still unclear on how to have a consistent intensity meaning across ages for spatio-temporal atlas creation, and especially when mixing data from different studies.

A solution for this might comes from incorporating, in the intensity normalization process, informations from quantitative imaging (relaxometry, diffusion...). If a spatio-temporal atlas with consistent, meaningful intensity is ever performed and covers a sufficient number of age samples, one can then use it as reference to normalize intensities for subjects of any age using usual normalization techniques.

This incapacity of the classical T1 and T2-weighted images where the intensities have a fixed meaning emphasize the importance of multichannel atlases such as the one built in [Rohlfing 2009]. Looking at the creation of such multichannel, longitudinal atlases of the developing brain will then be of great interest too.

11.4.2 Segmentation

Atlas based segmentation is very common, it has notably very good reproducibilty properties across a dataset of subjects. It is well-known that the atlases should be chosen in age adequacy with the the subjects [Muzik 2000]. One can therefore not propagate the segmentations from the same atlases to a population covering a wide age range (especially during development). On the other hand, choosing different atlases for subsamples of the population may lead to inconstancies. Very little concern is given in the literature about methods to have age adapted segmentations while those being consistent across the subjects.

An obvious solution would be for an expert to manually segment a large cohort of subjects covering a sufficient number of age samples. This would be, though, an incredibly fastidious task...

11.5 Investigations on the convergence of the BCH formula

We experienced some intriguing behaviors when dealing with order 3 or more Baker-Campbell-Hausdorff (BCH) formula. Even though the accuracy of the BCH is globally getting better as the order increases, it is getting very wrong in some very localized areas. This phenomenon is illustrated in Figure 11.1 where the approximation from BCH is compared to the true value via the following error criterion: $E = \|\exp\left(\mathrm{BCH}(u,v)\right) - \exp(u) \circ \exp(v)\|^2$, where u and v are SVFs. One can clearly see an overall improvement as the order of the BCH increases at the exception of the area designed by the white arrow where a higher error spot is present. We suspect that those issues are related to the approximations inherent to the fact that we work with discrete grids. Also it seems that those divergent spots are localized in areas where the determinant of the jacobian is especially high. This definitely deserves some investigations.

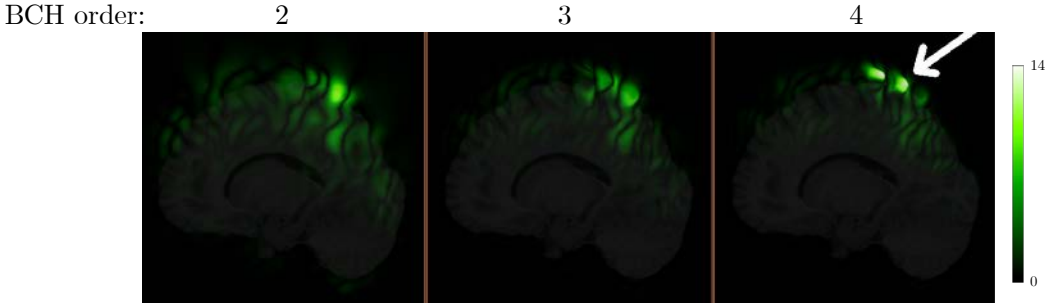

Figure 11.1: Error E in mm^2 for BCH order 2, 3 and 4

Part V

Appendix

Appendix A

Detailed calculations for axis-angle to quaternion rotation representation

---

Let $q = \begin{pmatrix} \cos\left(\frac{\theta}{2}\right) \\ \sin\left(\frac{\theta}{2}\right) u \end{pmatrix}$.

$$
\begin{aligned}
(0, v') &= q * (0, v) * q^{-1} = q * (0, v) * \bar{q} \\
&= \begin{pmatrix} \cos\left(\frac{\theta}{2}\right) \\ \sin\left(\frac{\theta}{2}\right) u \end{pmatrix} * v * \begin{pmatrix} \cos\left(\frac{\theta}{2}\right) \\ -\sin\left(\frac{\theta}{2}\right) u \end{pmatrix} \\
&= \begin{pmatrix} -\sin\left(\frac{\theta}{2}\right) u \cdot v \\ \sin\left(\frac{\theta}{2}\right) u \times v + \cos\left(\frac{\theta}{2}\right) v \end{pmatrix} * \begin{pmatrix} \cos\left(\frac{\theta}{2}\right) \\ -\sin\left(\frac{\theta}{2}\right) u \end{pmatrix} \\
&= \begin{pmatrix} -\sin\left(\frac{\theta}{2}\right)\cos\left(\frac{\theta}{2}\right) u \cdot v + \sin^2\left(\frac{\theta}{2}\right)(u \times v) \cdot u + \cos\left(\frac{\theta}{2}\right)\sin\left(\frac{\theta}{2}\right) v \cdot u \\ -\sin^2\left(\frac{\theta}{2}\right)(u \times v) \times u - \cos\left(\frac{\theta}{2}\right)\sin\left(\frac{\theta}{2}\right) v \times u + \sin\left(\frac{\theta}{2}\right)\cos\left(\frac{\theta}{2}\right) u \times v \\ \qquad + \cos^2\left(\frac{\theta}{2}\right) v + \sin^2\left(\frac{\theta}{2}\right)(u \cdot v) u \end{pmatrix} \\
&= \begin{pmatrix} 0 \\ -\frac{1-\cos(\theta)}{2}\left((u \cdot u)v - (u \cdot v)u\right) + 2\cos\left(\frac{\theta}{2}\right)\sin\left(\frac{\theta}{2}\right) u \times v \\ \qquad + \frac{1+\cos(\theta)}{2} v + \frac{1-\cos(\theta)}{2}(u \cdot v) u \end{pmatrix} \\
&= \begin{pmatrix} 0 \\ \cos(\theta)\, v + \sin(\theta)\, u \times v + (1 - \cos(\theta))\,(u \cdot v) u \end{pmatrix}
\end{aligned}
\tag{A.1}
$$

Using basic trigonometry formulas one can retrieve the Rodrigues formula where v' is the image of the vector v through a rotation of magnitude θ about the axis u .The same reasoning applies to $q = -\begin{pmatrix} \cos\left(\frac{\theta}{2}\right) \\ \sin\left(\frac{\theta}{2}\right) u \end{pmatrix}$.

Appendix B

Detailed calculations for optimizing anisotropic similarity between two sets of paired points

B.1

Let R be a rotation matrix. Then, an associated unit quaternion q is defined such as if $Rx = q * x * \bar{q}$. Thus:

$$\begin{aligned} \tilde{C}(q,S) &= \sum_i \|y'_i - q * \xi_i * \bar{q}\|^2 \\ &= \sum_i \|y'_i * q - q * \xi_i\|^2 \end{aligned} \tag{B.1}$$

B.2

If p is a vector, the associated quaternion is pure: $p_0 = 0$ which implies that L_p and R_p are skew-symmetric. Yet y'_i and ξ_i are vectors, thus:

$$\begin{aligned} \tilde{C}(q,S) &= \sum_i \|y'_i * q - q * \xi_i\|^2 \\ &= \sum_i \left\|L_{y'_i} q - R_{\xi_i} q\right\|^2 \\ &= \sum_i \left\|L_{y'_i} q + R^T_{\xi_i} q\right\|^2 \\ &= \sum_i \left(L_{y'_i} q + R^T_{\xi_i} q\right)^T \left(L_{y'_i} q + R^T_{\xi_i} q\right) \\ &= q^T \left(\sum_i \left(L_{y'_i} + R^T_{\xi_i}\right)^T \left(L_{y'_i} + R^T_{\xi_i}\right)\right) q \\ &= q^T \left(-\sum_i \left(L_{y'_i} + R^T_{\xi_i}\right)^2\right) q \end{aligned} \tag{B.2}$$

B.3

If p is a vector, the associated quaternion is pure: $p_0 = 0$ which implies that L_p and R_p are skew-symmetric and $L_p^2 = R_p^2 = -p^T p I_4$.

Yet y'_i and ξ_i are vectors, thus:

$$\begin{aligned}
\tilde{C}(q,S) &= -q^T \left(\sum_i \left(L_{y'_i} + R^T_{\xi_i} \right)^2 \right) q \\
&= -q^T \left(\sum_i \left(L^2_{y'_i} + 2L_{y'_i} R^T_{\xi_i} + {R^T_{\xi_i}}^2 \right) \right) q \\
&= -q^T \left(\sum_i \left(-{y'_i}^T y'_i I_4 + 2L_{y'_i} R^T_{\xi_i} - \xi_i^T \xi_i I_4 \right) \right) q \\
&= -q^T \left(\sum_i \left(-{y'_i}^T y'_i I_4 + 2L_{y'_i} R^T_{\xi_i} - \tilde{x}_i^T S^2 \tilde{x}_i I_4 \right) \right) q
\end{aligned} \tag{B.3}$$

Thus, by considering x_{ji} such that $x_i = (0 x_{1i} x_{2j} x_{3j})^T \in \mathbb{R}^4$, and E_{jj} the matrix with a 1 at the intersection of the j^{th} row and the column and zeros elsewhere, we have:

$$\begin{aligned}
\frac{\partial \tilde{C}}{\partial s_j} &= -q^T \left(\sum_i (2L_{y'_i} \frac{\partial R^T_{\xi_i}}{\partial s_j} - 2\tilde{x}_i^T s_j E_{jj} \tilde{x}_i) \right) q \\
&= -2q^T \left(\sum_i L_{y'_i} \frac{\partial R^T_{\xi_i}}{\partial s_j} \right) q + 2q^T \left(s_j \sum_i \tilde{x}^2_{ji} \right) q
\end{aligned} \tag{B.4}$$

Yet $\sum_i \tilde{x}^2_{ji}$ scalar and $q^T q = 1$, which leads to:

$$\begin{aligned}
\frac{\partial \tilde{C}}{\partial s_j} &= -q^T \left(\sum_i L_{y'_i} \frac{\partial R^T_{\xi_i}}{\partial s_j} \right) q + s_j \sum_i \tilde{x}^2_{ji} \\
\frac{\partial \tilde{C}}{\partial s_j} = 0 \Leftrightarrow \hat{s}_j &= \frac{1}{\sum_i \tilde{x}^2_{ji}} q^T \left(\sum_i L_{y'_i} \frac{\partial R^T_{\xi_i}}{\partial s_j} \right) q
\end{aligned} \tag{B.5}$$

B.4

$$\left\{ \begin{array}{rcl}
Q_{y'_i} \dfrac{\partial P_{\xi_i}}{\partial s_1} &=& \tilde{x}_{1i} \begin{pmatrix} y'_{1i} & 0 & -y'_{3i} & y'_{2i} \\ 0 & y'_{1i} & y'_{2i} & y'_{3i} \\ -y'_{3i} & y'_{2i} & -y'_{1i} & 0 \\ y'_{2i} & y'_{3i} & 0 & -y'_{1i} \end{pmatrix} \\
Q_{y'_i} \dfrac{\partial P_{\xi_i}}{\partial s_2} &=& \tilde{x}_{2i} \begin{pmatrix} y'_{2i} & y'_{3i} & 0 & -y'_{1i} \\ y'_{3i} & -y'_{2i} & y'_{1i} & 0 \\ 0 & y'_{1i} & y'_{2i} & y'_{3i} \\ -y'_{1i} & 0 & y'_{3i} & -y'_{2i} \end{pmatrix} \\
Q_{y'_i} \dfrac{\partial P_{\xi_i}}{\partial s_3} &=& \tilde{x}_{3i} \begin{pmatrix} y'_{3i} & -y'_{2i} & y'_{1i} & 0 \\ -y'_{2i} & -y'_{3i} & 0 & y'_{1i} \\ y'_{1i} & 0 & -y'_{3i} & y'_{2i} \\ 0 & y'_{1i} & y'_{2i} & y'_{3i} \end{pmatrix}
\end{array} \right. \tag{B.6}$$

Appendix C

Initial transformation for affine registration

Let $x = \{x_1, \dots, x_m\}$ and $y = \{y_1, \dots, y_n\}$ with $x_i, y_i \in \mathbb{R}^k$ be sets of the non-zero voxels coordinates in a $k-$dimensional space of each of the two images that are supposed to be registered. One can perform principal component analysis (PCA) on x and y:

Let $\bar{x}$ and $\bar{y}$ be the barycenters of x and y: $\bar{x} = \frac{1}{m}\sum_{i=1}^{m} x_i$ and $\bar{y} = \frac{1}{n}\sum_{i=1}^{n} y_i$

Let C_x and C_y be the covariance matrices associated to x and y:

$C_x = \frac{1}{m}\sum_{i=1}^{m}(x_i - \bar{x})(x_i - \bar{x})^T$

$C_y = \frac{1}{n}\sum_{i=1}^{n}(y_i - \bar{y})(y_i - \bar{y})^T$

Let $X_1, \dots, X_k$ be the eigen vectors of C_x and $\lambda_1, \dots, \lambda_k$ be the associated eigen values.

Let $Y_1, \dots, Y_k$ be the eigen vectors of C_y and $\mu_1, \dots, \mu_k$ be the associated eigen values.

X_i and Y_i are the vectors that orient the principal directions of x and y. λ_i and μ_i quantify the variance of x and y along those directions.

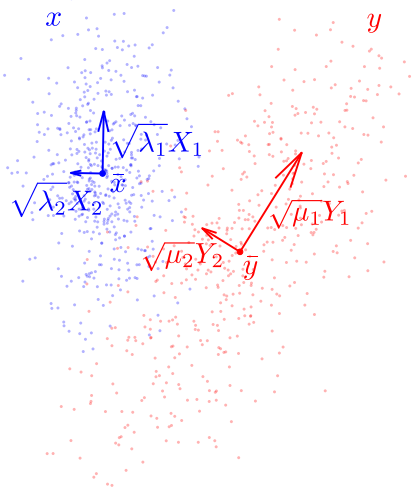

Figure C.1: Eigen vectors of the covariance matrix of x and y scaled by the square root of their eigen values, shifted to the barycenters.

Given that, an adequate initial transformation T_0 is the one that maps the two object presented Figure C.1 namely the barycenters translated by the eigen vectors of the covariance matrix x and y scaled by the square root of their eigen values and the barycenters themselves:

$$T_0 = \begin{pmatrix} \bar{y} + \sqrt{\mu_1}Y_1 & \cdots & \bar{y} + \sqrt{\mu_k}Y_k & \bar{y} \\ 1 & \cdots & 1 & 1 \end{pmatrix} \begin{pmatrix} \bar{x} + \sqrt{\lambda_1}X_1 & \cdots & \bar{x} + \sqrt{\lambda_k}X_k & \bar{x} \\ 1 & \cdots & 1 & 1 \end{pmatrix}^{-1} \tag{C.1}$$

This kind of initialization is purely geometric, it does not takes into account the intensities of the images but only whether a voxel belong to the mask or not. It allows to roughly match both brain orientation and barycenter but also to estimate a first anisotropic scaling.

Bibliography

[Akaike 1974] Hirotugu Akaike. *A new look at the statistical model identification.* IEEE Transactions on Automatic Control, vol. 19, no. 6, pages 716–723, 1974. (Cited on page 59.)

[Aljabar 2009] Paul Aljabar, R. A. Heckemann, A. Hammers, Jo V. Hajnal and Daniel Rueckert. *Multi-atlas based segmentation of brain images: Atlas selection and its effect on accuracy.* NeuroImage, vol. 46, no. 3, pages 726–738, 2009. (Cited on pages 39 and 70.)

[Alsop 2015] David C. Alsop, John A. Detre, Xavier Golay, Matthias Günther, Jeroen Hendrikse, Luis Hernandez-Garcia, Hanzhang Lu, Bradley J. Macintosh, Laura M. Parkes, Marion Smits, Matthias J.P. Van Osch, Danny J.J. Wang, Eric C. Wong and Greg Zaharchuk. *Recommended implementation of arterial spin-labeled Perfusion mri for clinical applications: A consensus of the ISMRM Perfusion Study group and the European consortium for ASL in dementia.* Magnetic Resonance in Medicine, vol. 73, no. 1, pages 102–116, 2015. (Cited on page 77.)

[Apgar 1953] Virginia Apgar. *A proposal for a new method of evaluation of the newborn infant.* Anesthesia and Analgesia, vol. 32, no. 4, pages 260–267, 1953. (Cited on page 74.)

[Arad 1995] Nur Arad and Daniel Reisfeld. *Image Warping Using Few Anchor Points and Radial Functions.* Computer Graphics Forum, vol. 14, no. 1, pages 35–46, feb 1995. (Cited on page 35.)

[Ardekani 2005] Babak A. Ardekani, Stephen Guckemus, Alvin Bachman, Matthew J. Hoptman, Michelle Wojtaszek and Jay Nierenberg. *Quantitative comparison of algorithms for inter-subject registration of 3D volumetric brain MRI scans.* Journal of Neuroscience Methods, vol. 142, no. 1, pages 67–76, mar 2005. (Cited on page 37.)

[Arsigny 2006a] Vincent Arsigny, Olivier Commowick, Xavier Pennec and Nicholas Ayache. *A Log-Euclidean Framework for Statistics on Diffeomorphisms.* MICCAI, vol. 4190, pages 924–931, 2006. (Cited on pages 20, 22, 24, 25, 90 and 98.)

[Arsigny 2006b] Vincent Arsigny, Olivier Commowick, Xavier Pennec and Nicholas Ayache. *A Log-Euclidean Polyaffine Framework for Locally Rigid or Affine Registration.* In International Workshop on Biomedical Image Registration, pages 120–127, 2006. (Cited on pages 22, 25 and 36.)

[Arsigny 2009] Vincent Arsigny, Olivier Commowick, Nicholas Ayache and Xavier Pennec. *A fast and log-euclidean polyaffine framework for locally linear registration.* Journal of Mathematical Imaging and Vision, 2009. (Cited on pages 24, 25, 36 and 114.)

[Ashburner 2007] John Ashburner. *A fast diffeomorphic image registration algorithm.* NeuroImage, vol. 38, no. 1, pages 95–113, 2007. (Cited on page 34.)

[Auzias 2015] G. Auzias, François De Guio, A. Pepe, François Rousseau, J. F. Mangin, N. Girard, J. Lefevre and Olivier Coulon. *Model-driven parameterization of fetal cortical surfaces.* Proceedings - International Symposium on Biomedical Imaging, vol. 2015-July, pages 1260–1263, 2015. (Cited on page 69.)

[Avants 2004] Brian Avants and James C. Gee. *Geodesic estimation for large deformation anatomical shape averaging and interpolation.* NeuroImage, vol. 23, no. SUPPL. 1, pages 139–150, 2004. (Cited on page 45.)

[Avants 2008] Brian Avants, C. L. Epstein, M. Grossman and J. C. Gee. *Symmetric diffeomorphic image registration with cross-correlation: Evaluating automated labeling of elderly and neurodegenerative brain.* Medical Image Analysis, vol. 12, no. 1, pages 26–41, 2008. (Cited on page 38.)

[Avants 2010] Brian B. Avants, Paul Yushkevich, John Pluta, David Minkoff, Marc Korczykowski, John Detre and James C. Gee. *The optimal template effect in hippocampus studies of diseased populations.* NeuroImage, vol. 49, no. 3, pages 2457–2466, 2010. (Cited on page 45.)

[Avants 2011] Brian Avants, Nicholas J Tustison, Jue Wu, Philip A Cook and James C Gee. *ANTS: Advanced Open-Source Tools for Normalization And Neuroanatomy.* Neuroinformatics, vol. 9, no. 4, pages 381–400, 2011. (Cited on page 38.)

[Aylward 1991] E. H. Aylward, J. Schwartz, S. Machlin and G. Pearlson. *Bicaudate ratio as a measure of caudate volume on MR images.* American Journal of Neuroradiology, vol. 12, no. 6, pages 1217–1222, 1991. (Cited on page 52.)

[Barkovich 1998] A. James Barkovich, Beatrice Latal Hajnal, Daniel Vigneron, Augusto Sola, J. Colin Partridge, Faith Allen and Donna M. Ferriero. *Prediction of neuromotor outcome in perinatal asphyxia: Evaluation of MR scoring systems.* American Journal of Neuroradiology, vol. 19, no. 1, pages 143–149, 1998. (Cited on page 78.)

[Baxter 2019] Luke Baxter, Sean Fitzgibbon, Fiona Moultrie, Sezgi Goksan, Mark Jenkinson, Stephen Smith, Jesper Andersson, Eugene Duff and Rebeccah Slater. *Optimising neonatal fMRI data analysis: Design and validation of an extended dHCP preprocessing pipeline to characterise noxious-evoked brain activity in infants.* NeuroImage, vol. 186, no. November 2018, pages 286–300, 2019. (Cited on pages 73 and 80.)

[Beg 2005] M. Faisal Beg, Michael I. Miller, Alain Trouvé and Laurent Younes. *Computing large deformation metric mappings via geodesic flows of diffeomorphisms.* International Journal of Computer Vision, vol. 61, no. 2, pages 139–157, 2005. (Cited on pages 19 and 38.)

[Benjamini 1995] Yoav Benjamini and Yosef Hochberg. *Controlling the False Discovery Rate: A Practical and Powerful Approach to Multiple Testing.* Journal of the Royal Statistical Society, vol. 57, no. 1, pages 289–300, 1995. (Cited on page 64.)

[Bermel 2002] Robert A. Bermel, Rohit Bakshi, Christopher Tjoa, Srinivas R. Puli and Lawrence Jacobs. *Bicaudate ratio as a magnetic resonance imaging marker of brain atrophy in multiple sclerosis.* Archives of Neurology, vol. 59, no. 2, pages 275–280, 2002. (Cited on page 52.)

[Bhatia 2004] K.K. Bhatia, Jo V. Hajnal, B.K. Puri, A. David Edwards and Daniel Rueckert. *Consistent groupwise non-rigid registration for atlas construction.* In IEEE International Symposium on Biomedical Imaging: Macro to Nano (IEEE Cat No. 04EX821), volume 2, pages 908–911. IEEE, 2004. (Cited on page 45.)

[Bondiau 2005] Pierre Yves Bondiau, Grégoire Malandain, Stéphane Chanalet, Pierre Yves Marcy, Jean Louis Habrand, François Fauchon, Philippe Paquis, Adel Courdi, Olivier Commowick, Isabelle Rutten and Nicholas Ayache. *Atlas-based automatic segmentation of MR images: Validation study on the brainstem in radiotherapy context.* International Journal of Radiation Oncology Biology Physics, vol. 61, no. 1, pages 289–298, 2005. (Cited on page 39.)

[Bookheimer 2019] Susan Y. Bookheimer, David H. Salat, Melissa Terpstra, Beau M. Ances, Deanna M. Barch, Randy L. Buckner, Gregory C. Burgess, Sandra W. Curtiss, Mirella Diaz-Santos, Jennifer Stine Elam, Bruce Fischl, Douglas N. Greve, Hannah A. Hagy, Michael P. Harms, Olivia M. Hatch, Trey Hedden, Cynthia Hodge, Kevin C. Japardi, Taylor P. Kuhn, Timothy K. Ly, Stephen M. Smith, Leah H. Somerville, Kâmil Ugurbil, Andre van der Kouwe, David Van Essen, Roger P. Woods and Essa Yacoub. *The Lifespan Human Connectome Project in Aging: An overview.* NeuroImage, vol. 185, no. July 2018, pages 335–348, 2019. (Cited on page 113.)

[Bookstein 1989] F.L. Bookstein. *Principal warps: thin-plate splines and the decomposition of deformations.* IEEE Transactions on Pattern Analysis and Machine Intelligence, vol. 11, no. 6, pages 567–585, jun 1989. (Cited on page 35.)

[Bookstein 1991] Fred L. Bookstein. *Thin-Plate splines and the atlas problem for biomedical images.* In Information Processing in Medical Imaging, volume 511, pages 326–342. Springer-Verlag, Berlin/Heidelberg, 1991. (Cited on page 35.)

[Bossa 2007] Matias Bossa, Monica Hernandez and Salvador Olmos. *Contributions to 3D diffeomorphic atlas estimation: Application to brain images.* Lecture Notes in Computer Science (including subseries Lecture Notes in Artificial Intelligence and Lecture Notes in Bioinformatics), vol. 4791 LNCS, no. PART 1, pages 667–674, 2007. (Cited on pages 20 and 25.)

[Bossa 2008] Matias Bossa and Salvador Olmos. *A new algorithm for the computation of the group logarithm of diffeomorphism.* Medical Image Computing and Computer-Assisted Intervention (MICCAI): International Workshop on the Mathematical Foundations of Computational Anatomy (MFCA), no. 1, pages 13 – 23, 2008. (Cited on page 37.)

[Brown 1992] Lisa Gottesfeld Brown. *A survey of image registration techniques.* ACM Computing Surveys (CSUR), vol. 24, no. 4, pages 325–376, 1992. (Cited on page 27.)

[Burnham 2002] Kenneth P. Burnham and David R. Anderson. Model selection and multimodel inference: A practical approach. 2002. (Cited on page 59.)

[Burnham 2004] Kenneth P. Burnham and David R. Anderson. *Multimodel inference: Understanding AIC and BIC in model selection.* Sociological Methods and Research, vol. 33, no. 2, pages 261–304, 2004. (Cited on page 59.)

[Buxton 1998] Richard B. Buxton, Lawrence R. Frank, Eric C. Wong, Bettina Siewert, Steven Warach and Robert R. Edelman. *A general kinetic model for quantitative perfusion imaging with arterial spin labeling.* Magnetic Resonance in Medicine, vol. 40, no. 3, pages 383–396, 1998. (Cited on page 77.)

[Cabezas 2011] Mariano Cabezas, Arnau Oliver, Xavier Lladó, Jordi Freixenet and Meritxell Bach Cuadra. *A review of atlas-based segmentation for magnetic resonance brain images.* Computer Methods and Programs in Biomedicine, vol. 104, no. 3, pages e158–e177, 2011. (Cited on pages 4, 7, 39 and 97.)

[Cachier 2003] Pascal Cachier, Eric Bardinet, Didier Dormont, Xavier Pennec and Nicholas Ayache. *Iconic feature based nonrigid registration: The PASHA algorithm.* Computer Vision and Image Understanding, vol. 89, no. 2-3, pages 272–298, 2003. (Cited on page 37.)

[Charon 2015] Valérie Charon, Maïa Proisy, Jean Christophe Ferré, Bertrand Bruneau, Catherine Tréguier, Alain Beuchée, Jennifer Chauvel and Céline Rozel. *Comparison of early and late MRI in neonatal hypoxic-ischemic encephalopathy using three assessment methods.* Pediatric Radiology, vol. 45, no. 13, pages 1988–2000, 2015. (Cited on pages 73 and 78.)

[Choe 2013] M.-s. Choe, S. Ortiz-Mantilla, N. Makris, M. Gregas, J. Bacic, D. Haehn, D. Kennedy, R. Pienaar, V. S. Caviness, A. A. Benasich and P. E. Grant. *Regional Infant Brain Development: An MRI-Based Morphometric Analysis in 3 to 13 Month Olds.* Cerebral Cortex, vol. 23, no. 9, pages 2100–2117, sep 2013. (Cited on page 52.)

[Choi 2000] Yongchoel Choi and Seungyong Lee. *Injectivity conditions of 2D and 3D uniform cubic B-spline functions.* Graphical Models, vol. 62, no. 6, pages 411–427, 2000. (Cited on page 36.)

[Christensen 1996] Gary E. Christensen, Richard D. Rabbitt and Michael I. Miller. *Deformable templates using large deformation kinematics.* IEEE Transactions on Image Processing, vol. 5, no. 10, pages 1435–1447, 1996. (Cited on page 19.)

[Coffey 1998] C.E Coffey. *Sex Differences in Brain Aging.* Arch Neurol, 1998. (Cited on page 52.)

[Collett 2012] Brent R. Collett, Elizabeth H. Aylward, Jessica Berg, Candice Davidoff, Justin Norden, Michael L. Cunningham and Matthew L. Speltz. *Brain volume and shape in infants with deformational plagiocephaly.* Child's Nervous System, vol. 28, no. 7, pages 1083–1090, 2012. (Cited on pages 71 and 114.)

[Collins 1994] D. Louis Collins, Peter Neelin, Terrence M. Peters and Alan C. Evans. *Automatic 3D Intersubject Registration of MR Volumetric Data in Standardized Talairach Space.* Journal of Computer Assisted Tomography, vol. 18, no. 2, pages 192–205, mar 1994. (Cited on pages 40 and 41.)

[Commowick 2008] Olivier Commowick, Vincent Arsigny, A. Isambert, J. Costa, F. Dhermain, F. Bidault, P. Y. Bondiau, N. Ayache and G. Malandain. *An efficient locally affine framework for the smooth registration of anatomical structures.* Medical Image Analysis, vol. 12, no. 4, pages 427–441, 2008. (Cited on pages 36 and 114.)

[Commowick 2012a] Olivier Commowick, Nicolas Wiest-Daesslé and Sylvain Prima. *Automated diffeomorphic registration of anatomical structures with rigid parts: application to dynamic cervical MRI.* 15th International Conference on Medical Image Computing and Computer Assisted Intervention, vol. 15, no. 2, pages 163–170, 2012. (Cited on pages 25, 30, 36, 38 and 92.)

[Commowick 2012b] Olivier Commowick, Nicolas Wiest-Daessle and Sylvain Prima. *Block-matching strategies for rigid registration of multimodal medical images.* In Proceedings - International Symposium on Biomedical Imaging, pages 700–703, 2012. (Cited on pages 30, 31, 38 and 91.)

[Commowick 2019] Olivier Commowick. *Compartments imaging for the characterization of brain diseases from quantitative MRI.* 2019. (Cited on pages 29, 36 and 38.)

[Courchesne 2000] Eric Courchesne, Heather J. Chisum, Jeanne Townsend, Angilene Cowles, James Covington, Brian Egaas, Mark Harwood, Stuart Hinds and Gary A. Press. *Normal Brain Development and Aging: Quantitative Analysis at in Vivo MR Imaging in Healthy Volunteers.* Radiology, vol. 216, no. 3, pages 672–682, 2000. (Cited on pages 52 and 69.)

[Cury 2014] Claire Cury, Joan Alexis Glaunès and Olivier Colliot. *Diffeomorphic Iterative Centroid Methods for Template Estimation on Large Datasets.* Geometric Theory of Information, vol. Chapter 10, pages 273–299, 2014. (Cited on pages 98, 99 and 113.)

[Cury 2018] Claire Cury, Joan A. Glaunès, Roberto Toro, Marie Chupin, Gunter Schumann, Vincent Frouin, Jean Baptiste Poline and Olivier Colliot. *Statistical shape analysis of large datasets based on diffeomorphic iterative centroids.* Frontiers in Neuroscience, vol. 12, no. NOV, pages 0–18, 2018. (Cited on page 113.)

[Davis 2010] Brad Davis, P. Thomas Fletcher, Elizabeth Bullitt and Sarang Joshi. *Population shape regression from random design data.* International Journal of Computer Vision, 2010. (Cited on pages 23, 24 and 46.)

[De Vis 2015] Jill B. De Vis, Jeroen Hendrikse, Esben T. Petersen, Linda S. de Vries, Frank van Bel, Thomas Alderliesten, Simona Negro, Floris Groenendaal and Manon J.N.L. Benders. *Arterial spin-labelling perfusion MRI and outcome in neonates with hypoxic-ischemic encephalopathy.* European Radiology, vol. 25, no. 1, pages 113–121, 2015. (Cited on page 74.)

[Declerck 1995] Jérôme Declerck, Gérard Subsol, Jean-Philippe Thirion and Nicholas Ayache. *Automatic retrieval of anatomical structures in 3D medical images.* Lecture Notes in Computer Science (including subseries Lecture Notes in Artificial Intelligence and Lecture Notes in Bioinformatics), vol. 905, pages 153–162, 1995. (Cited on page 28.)

[Dickie 2017] David Alexander Dickie, Susan D. Shenkin, Devasuda Anblagan, Juyoung Lee, Manuel Blesa Cabez, David Rodriguez, James P. Boardman, Adam Waldman, Dominic E. Job and Joanna M. Wardlaw. *Whole Brain Magnetic Resonance Image Atlases: A Systematic Review of Existing Atlases and Caveats for Use in Population Imaging.* Frontiers in Neuroinformatics, vol. 11, no. January, 2017. (Cited on page 42.)

[Dubois 2014] Jessica Dubois, G. Dehaene-Lambertz, S. Kulikova, C. Poupon, P. S. Hüppi and L. Hertz-Pannier. *The early development of brain white matter: A review of imaging studies in fetuses, newborns and infants.* Neuroscience, vol. 276, pages 48–71, 2014. (Cited on page 73.)

[Dubois 2019] Jessica Dubois, Julien Lefèvre, Hugo Angleys, François Leroy, Clara Fischer, Jessica Lebenberg, Ghislaine Dehaene-Lambertz, Cristina Borradori-Tolsa, François Lazeyras, Lucie Hertz-Pannier, Jean François Mangin, Petra S. Hüppi and David Germanaud. *The dynamics of cortical folding waves and prematurity-related deviations revealed by spatial and spectral analysis of gyrification.* NeuroImage, vol. 185, no. February 2018, pages 934–946, 2019. (Cited on pages 52 and 73.)

[Dupuis 1998] Paul Dupuis, Ulf Grenander and Michael I. Miller. *Variational problems on flows of diffeomorphisms for image matching.* Quarterly of applied mathematics, vol. LVI, no. 3, pages 587–600, 1998. (Cited on page 20.)

[Durazzo 2011] Timothy C. Durazzo, Duygu Tosun, Shannon Buckley, Stefan Gazdzinski, Anderson Mon, Susanna L. Fryer and Dieter J. Meyerhoff. *Cortical thickness, surface area, and volume of the brain reward system in alcohol dependence: Relationships to relapse and extended abstinence.* Alcoholism: Clinical and Experimental Research, vol. 35, no. 6, pages 1187–1200, jun 2011. (Cited on page 52.)

[Durrleman 2009] Stanley Durrleman, Xavier Pennec, Alain Trouvé, Guido Gerig and Nicholas Ayache. *Spatiotemporal Atlas Estimation for Developmental Delay Detection in Longitudinal Datasets.* In Bone, volume 23, pages 297–304. 2009. (Cited on pages 40, 47 and 113.)

[Durrleman 2013] Stanley Durrleman, Xavier Pennec, Alain Trouvé, José Braga, Guido Gerig and Nicholas Ayache. Toward a comprehensive framework for the spatiotemporal statistical analysis of longitudinal shape data, volume 103. 2013. (Cited on page 47.)

[Ericsson 2008] Anders Ericsson, Paul Aljabar and Daniel Rueckert. *Construction of a patient-specific atlas of the brain: Application to normal aging.* In 2008 5th IEEE International Symposium on Biomedical Imaging: From Nano to Macro, pages 480–483. IEEE, may 2008. (Cited on pages 46 and 47.)

[Evans 1993] Alan C. Evans, D.L. Collins, S.R. Mills, E.D. Brown, R.L. Kelly and T.M. Peters. *3D statistical neuroanatomical models from 305 MRI volumes.* In 1993 IEEE Conference Record Nuclear Science Symposium and Medical Imaging Conference, pages 1813–1817. IEEE, 1993. (Cited on pages 40 and 41.)

[Evans 2012] Alan C. Evans, Andrew L. Janke, D. Louis Collins and Sylvain Baillet. *Brain templates and atlases.* NeuroImage, vol. 62, no. 2, pages 911–922, 2012. (Cited on page 42.)

[Fonov 2011] Vladimir Fonov, Alan C. Evans, Kelly Botteron, C. Robert Almli, Robert C. McKinstry and D. Louis Collins. *Unbiased average age-appropriate atlases for pediatric studies.* NeuroImage, vol. 54, no. 1, pages 313–327, 2011. (Cited on pages 41 and 43.)

[Fornefett 2003] M. Fornefett, K. Rohr and H.S. Stiehl. *Elastic registration of medical images using radial basis functions with compact support.* In Proceedings. 1999 IEEE Computer Society Conference on Computer Vision and Pattern Recognition (Cat. No PR00149), pages 402–407. IEEE Comput. Soc, dec 2003. (Cited on page 35.)

[Fréchet 1948] Maurice René Fréchet. *Les éléments aléatoires de nature quelconque dans un espace distancié.* Annales de l'institut Henri Poincaré, vol. 10, no. 4, pages 215–310, 1948. (Cited on page 41.)

[Frisoni 2010] Giovanni B. Frisoni, Nick C. Fox, Clifford R. Jack, Philip Scheltens and Paul M. Thompson. *The clinical use of structural MRI in Alzheimer disease*, feb 2010. (Cited on page 52.)

[Gallier 2008] Jean Gallier. *Logarithms and Square Roots of Real Matrices.* 2008. (Cited on page 24.)

[Gholipour 2007] Ali Gholipour, Nasser Kehtarnavaz, Richard Briggs, Michael Devous and Kaundinya Gopinath. *Brain Functional Localization: A Survey of Image Registration Techniques.* IEEE Transactions on Medical Imaging, vol. 26, no. 4, pages 427–451, apr 2007. (Cited on pages 4, 7 and 29.)

[Gholipour 2017] Ali Gholipour, Caitlin K. Rollins, Clemente Velasco-Annis, Abdelhakim Ouaalam, Alireza Akhondi-Asl, Onur Afacan, Cynthia M. Ortinau, Sean Clancy, Catherine Limperopoulos, Edward Yang, Judy A. Estroff and Simon K. Warfield. *A normative spatiotemporal MRI atlas of the fetal brain for automatic segmentation and analysis of early brain growth.* Scientific Reports, vol. 7, no. 1, page 476, dec 2017. (Cited on pages 46 and 47.)

[Giedd 1999] Jay N. Giedd, Jonathan Blumenthal, Neal O. Jeffries, F. X. Castellanos, Hong Liu, Alex Zijdenbos, Tomáš Paus, Alan C. Evans and Judith L. Rapoport. *Brain development during childhood and adolescence: a longitudinal MRI study.* Nature Neuroscience, vol. 2, no. 10, pages 861–863, 1999. (Cited on page 52.)

[Giedd 2010] Jay N. Giedd and Judith L. Rapoport. *Structural MRI of Pediatric Brain Development: What Have We Learned and Where Are We Going?* Neuron, vol. 67, no. 5, pages 728–734, 2010. (Cited on page 52.)

[Giorgio 2013] Antonio Giorgio and Nicola De Stefano. *Clinical use of brain volumetry.* Journal of Magnetic Resonance Imaging, vol. 37, no. 1, pages 1–14, 2013. (Cited on page 52.)

[Gousias 2008] Ioannis S. Gousias, Daniel Rueckert, Rolf A. Heckemann, Leigh E. Dyet, James P. Boardman, A. David Edwards and Alexander Hammers. *Automatic segmentation of brain MRIs of 2-year-olds into 83 regions of interest.* NeuroImage, vol. 40, no. 2, pages 672–684, 2008. (Cited on page 52.)

[Gousias 2010] Ioannis S. Gousias, Alexander Hammers, Rolf A. Heckemann, Serena J. Counsell, Leigh E. Dyet, James P. Boardman, A. David Edwards and Daniel Rueckert. *Atlas selection strategy for automatic segmentation of pediatric brain MRIs into 83 ROIs.* 2010 IEEE International Conference on Imaging Systems and Techniques, IST 2010 - Proceedings, pages 290–293, 2010. (Cited on page 70.)

[Gousias 2012] Ioannis S. Gousias, A. David Edwards, Mary A. Rutherford, Serena J. Counsell, Jo V. Hajnal, Daniel Rueckert and Alexander Hammers. *Magnetic resonance imaging of the newborn brain: Manual segmentation of labelled atlases in term-born and preterm infants.* NeuroImage, vol. 62, no. 3, pages 1499–1509, 2012. (Cited on page 142.)

[Gousias 2013] Ioannis S. Gousias, Alexander Hammers, Serena J. Counsell, Latha Srinivasan, Mary A. Rutherford, Rolf A. Heckemann, Jo V. Hajnal, Daniel Rueckert and A. David Edwards. *Magnetic Resonance Imaging of the Newborn Brain: Automatic Segmentation of Brain Images into 50 Anatomical Regions.* PLoS ONE, vol. 8, no. 4, 2013. (Cited on page 142.)

[Grabowski 1988] Janusz Grabowski. *Free subgroups of diffeomorphism groups.* Fundamenta Mathematicae, vol. 131, no. 2, pages 103–121, 1988. (Cited on page 20.)

[Guimond 2000] Alexandre Guimond, Jean Meunier and Jean-Philippe Thirion. *Average brain models: A convergence study.* Computer vision and image understanding, vol. 77, no. 2, pages 192–210, 2000. (Cited on pages 42, 43, 48, 56, 75, 89, 90, 91, 92, 96, 98, 100, 101 and 110.)

[Hajnal 2001] Jo V. Hajnal, D. J. Hawkes and Derek L. G. Hill. Medical Image Registration. CRC Press, 2001. (Cited on page 29.)

[Hamano 1990] K. Hamano, N. Iwasaki, K. Kawashima and H. Takita. *Volumetric quantification of brain volume in children using sequential CT scans.* Neuroradiology, vol. 32, no. 4, pages 300–303, 1990. (Cited on pages 52 and 69.)

[Hamilton 1843] William R. Hamilton. *On a new Species of Imaginary Quantities connected with a theory of Quaternions.* Proceedings of the Royal Irish Academy, vol. 2, 1843. (Cited on page 15.)

[Harms 2018] Michael P. Harms, Leah H. Somerville, Beau M. Ances, Jesper Andersson, Deanna M. Barch, Matteo Bastiani, Susan Y. Bookheimer, Timothy B. Brown, Randy L. Buckner, Gregory C. Burgess, Timothy S. Coalson, Michael A. Chappell, Mirella Dapretto, Gwenaëlle Douaud, Bruce Fischl, Matthew F. Glasser, Douglas N. Greve, Cynthia Hodge, Keith W. Jamison, Saad Jbabdi, Sridhar Kandala, Xiufeng Li, Ross W. Mair, Silvia Mangia, Daniel Marcus, Daniele Mascali, Steen Moeller, Thomas E. Nichols, Emma C. Robinson, David H. Salat, Stephen M. Smith, Stamatios N. Sotiropoulos, Melissa Terpstra, Kathleen M. Thomas, M. Dylan Tisdall, Kamil Ugurbil, Andre van der Kouwe, Roger P. Woods, Lilla Zöllei, David C. Van Essen and Essa Yacoub. *Extending the Human Connectome Project across ages: Imaging protocols for the Lifespan Development and Aging projects.* NeuroImage, vol. 183, no. July, pages 972–984, 2018. (Cited on page 113.)

[Heckemann 2006] Rolf A. Heckemann, Jo V. Hajnal, Paul Aljabar, Daniel Rueckert and Alexander Hammers. *Automatic anatomical brain MRI segmentation combining label propagation and decision fusion.* NeuroImage, vol. 33, no. 1, pages 115–126, 2006. (Cited on pages 39 and 57.)

[Hernandez 2007] Monica Hernandez, Matias Bossa and Salvador Olmos. *Estimation of statistical atlases using groups of diffeomorphisms.* Technical report, 2007. (Cited on pages 42 and 43.)

[Higham 2008] Nicholas J. Higham. Functions of Matrices: Theory and Computation. Society for Industrial and Applied Mathematics, 2008. (Cited on page 24.)

[Holden 2008] Mark Holden. *A Review of Geometric Transformations for Nonrigid Body Registration.* In IEEE transactions in medical imaging, volume 27, pages 111–128, 2008. (Cited on page 34.)

[Horn 1987] Berthold K. P. Horn. *Closed-form solution of absolute orientation using unit quaternions.* Journal of the Optical Society of America A, vol. 4, no. 4, page 629, 1987. (Cited on pages 33, 53, 54 and 55.)

[Howell 2019] Brittany R. Howell, Martin A. Styner, Wei Gao, Pew Thian Yap, Li Wang, Kristine Baluyot, Essa Yacoub, Geng Chen, Taylor Potts, Andrew Salzwedel, Gang Li, John H. Gilmore, Joseph Piven, J. Keith Smith, Dinggang Shen, Kamil Ugurbil, Hongtu Zhu, Weili Lin and Jed T. Elison. *The UNC/UMN Baby Connectome Project (BCP): An overview of the study design and protocol development.* NeuroImage, vol. 185, no. October 2017, pages 891–905, 2019. (Cited on page 113.)

[Huber 1964] Peter J. Huber. *Robust Estimation of a Location Parameter.* The Annals of Mathematical Statistics, vol. 35, no. 1, pages 73–101, 1964. (Cited on page 77.)

[Huettel 2004] Scott A Huettel, Allen W Song and Gregory McCarthy. Functional magnetic resonance imaging. Sinauer Associates Sunderland, MA, 2004. (Cited on pages 3 and 7.)

[Hüppi 1998] Petra S. Hüppi, S Warfield, R Kikinis, P D Barnes, G P Zientara, F a Jolesz, M K Tsuji and J J Volpe. *Quantitative magnetic resonance imaging of brain development in premature and mature newborns.* Annals of neurology, vol. 43, no. 2, pages 224–235, 1998. (Cited on page 52.)

[Iglesias 2015] Juan Eugenio Iglesias and Mert R. Sabuncu. *Multi-atlas segmentation of biomedical images: A survey.* Medical Image Analysis, vol. 24, no. 1, pages 205–219, 2015. (Cited on page 39.)

[Iwasaki 1997] N. Iwasaki, K. Hamano, Y. Okada, Y. Horigome, J. Nakayama, T. Takeya, H. Takita and T. Nose. *Volumetric quantification of brain development using MRI.* Neuroradiology, vol. 39, no. 12, pages 841–846, 1997. (Cited on pages 52 and 69.)

[Johansen-Berg 2013] Heidi Johansen-Berg and Timothy EJ Behrens. Diffusion MRI: From Quantitative Measurement to In vivo Neuroanatomy. Academic Press, 2013. (Cited on pages 3 and 7.)

[Joshi 2004] Sarang Joshi, Brad Davis, Matthieu Jomier and Guido Gerig. *Unbiased diffeomorphic atlas construction for computational anatomy.* NeuroImage, vol. 23, pages S151–S160, 2004. (Cited on pages 41 and 45.)

[Kapellou 2006] Olga Kapellou, Serena J. Counsell, Nigel Kennea, Leigh Dyet, Nadeem Saeed, Jaroslav Stark, Elia Maalouf, Philip Duggan, Morenike Ajayi-Obe, Jo Hajnal, Joanna M. Allsop, James Boardman, Mary A. Rutherford, Frances Cowan and A. David Edwards. *Abnormal cortical development after premature birth shown by altered allometric scaling of brain growth.* PLoS Medicine, vol. 3, no. 8, pages 1382–1390, 2006. (Cited on pages 4 and 8.)

[Kim 2016] Sun Hyung Kim, Ilwoo Lyu, Vladimir Fonov, Clement Vachet, H. C. Hazlett, Rachel G. Smith, J. Piven, Stephen R. Dager, Robert C. Mckinstry, John R. Pruett, Alan C. Evans, D. Louis Collins, Kelly N. Botteron, Robert T. Schultz, G. Gerig, Martin A. Styner, C. Chappell, Stephen R. Dager, A. Estes, D. Shaw, K. Botteron, R. McKinstry, J. Constantino, J. Pruett, R. Schultz, S. Paterson, L. Zwaigenbaum, J. Ellison,

G. B. Pike, P. Kostopoulos, S. Das, H. Gu and M. Styner. *Development of cortical shape in the human brain from 6 to 24months of age via a novel measure of shape complexity.* NeuroImage, vol. 135, pages 163–176, 2016. (Cited on page 69.)

[Klein 2009] Arno Klein, Jesper Andersson, Babak A. Ardekani, John Ashburner, Brian Avants, Ming Chang Chiang, Gary E. Christensen, D. Louis Collins, James Gee, Pierre Hellier, Joo Hyun Song, Mark Jenkinson, Claude Lepage, Daniel Rueckert, Paul M. Thompson, Tom Vercauteren, Roger P. Woods, J. John Mann and Ramin V. Parsey. *Evaluation of 14 nonlinear deformation algorithms applied to human brain MRI registration.* NeuroImage, vol. 46, no. 3, pages 786–802, 2009. (Cited on pages 34, 37 and 38.)

[Knickmeyer 2010] Rebecca C Knickmeyer, Sylvain Gouttard, Chaeryon Kang, Dianne Evans, J Keith Smith, Robert M Hamer, Weili Lin, Guido Gerig and H John. *A Structural MRI Study of Human Brain Development from Birth to 2 Years.* Journal of Neuroscience, vol. 28, no. 47, pages 12176–12182, 2010. (Cited on pages 52 and 69.)

[Kuklisova Murgasova Deprez 2010] Maria Kuklisova Murgasova Deprez, Latha Srinivasan, Ioannis S Gousias, Paul Aljabar, Jo V. Hajnal, A. David Edwards and Daniel Rueckert. *Construction of a dynamic 4D probabilistic atlas for the developing brain.* In 2010 IEEE International Symposium on Biomedical Imaging: From Nano to Macro, pages 952–955. IEEE, 2010. (Cited on page 43.)

[Kuklisova Murgasova Deprez 2011] Maria Kuklisova Murgasova Deprez, Paul Aljabar, Latha Srinivasan, Serena J. Counsell, Valentina Doria, Ahmed Serag, Ioannis S. Gousias, James P. Boardman, Mary A. Rutherford, A. David Edwards, Jo V. Hajnal and Daniel Rueckert. *A dynamic 4D probabilistic atlas of the developing brain.* NeuroImage, vol. 54, no. 4, pages 2750–2763, 2011. (Cited on pages 43, 52 and 90.)

[Lane 1994] Thomas P. Lane and William H. DuMouchel. *Simultaneous Confidence Intervals in Multiple Regression.* The American Statistician, vol. 48, no. 4, pages 315–321, nov 1994. (Cited on page 60.)

[Lange 2012] Nicholas Lange. *Total and regional brain volumes in a population-based normative sample from 4 to 18 years: The NIH MRI study of normal brain development.* Cerebral Cortex, vol. 22, no. 1, pages 1–12, 2012. (Cited on page 52.)

[Lefèvre 2016] Julien Lefèvre, David Germanaud, Jessica Dubois, François Rousseau, Ines De MacEdo Santos, Hugo Angleys, Jean François Mangin, Petra S. Hüppi, Nadine Girard and François De Guio. *Are developmental trajectories of cortical folding comparable between cross-sectional datasets of fetuses and preterm newborns?* Cerebral Cortex, vol. 26, no. 7, pages 3023–3035, 2016. (Cited on pages 52 and 69.)

[Legouhy 2019] Antoine Legouhy, Olivier Commowick, François Rousseau and Christian Barillot. *Unbiased longitudinal brain atlas creation using robust linear registration and log-Euclidean framework for diffeomorphisms.* In Proceedings - International Symposium on Biomedical Imaging, pages 1038–1041. IEEE, 2019. (Cited on pages 56, 67, 75, 98, 100 and 101.)

[Li 2018] Fanzhang Li, Li Zhang and Zhao Zhang. *Lie group kernel learning.* In Lie Group Machine Learning, pages 275–318. 2018. (Cited on page 42.)

[Liao 2012] Shu Liao, Hongjun Jia, Guorong Wu, Dinggang Shen and The Alzheimer's Disease Neuroimaging Initiative. *A novel framework for longitudinal atlas construction with groupwise registration of subject image sequences.* NeuroImage, vol. 59, no. 2, pages 1275–1289, 2012. (Cited on page 48.)

[Little 1997] J.A. Little, D.L.G. Hill and D.J. Hawkes. *Deformations Incorporating Rigid Structures.* Computer Vision and Image Understanding, vol. 66, no. 2, pages 223–232, may 1997. (Cited on page 35.)

[Lorenzen 2004] Peter Lorenzen, Brad Davis, Guido Gerig, Elizabeth Bullitt Bullitt and Sarang Joshi. *Multi-class Posterior Atlas Formation via Unbiased Kullback-Leibler Template Estimation.* In Medical Image Computing and Computer-Assisted Intervention – MICCAI 2004, pages 95–102, 2004. (Cited on page 45.)

[Lorenzi 2013] Marco Lorenzi, Nicolas Ayache, G.B. Frisoni and Xavier Pennec. *LCC-Demons: A robust and accurate symmetric diffeomorphic registration algorithm.* NeuroImage, vol. 81, pages 470–483, 2013. (Cited on page 38.)

[Maes 1997] F. Maes, A. Collignon, D. Vandermeulen, G. Marchal and P. Suetens. *Multimodality image registration by maximization of mutual information.* IEEE Transactions on Medical Imaging, vol. 16, no. 2, pages 187–198, 1997. (Cited on pages 28 and 31.)

[Makropoulos 2016] Antonios Makropoulos, Paul Aljabar, Robert Wright, Britta Hüning, Nazakat Merchant, Tomoki Arichi, Nora Tusor, Jo V. Hajnal, A. David Edwards, Serena J. Counsell and Daniel Rueckert. *Regional growth and atlasing of the developing human brain.* NeuroImage, vol. 125, pages 456–478, 2016. (Cited on page 52.)

[Malandain 1993] Grégoire Malandain, Gilles Bertrand and Nicholas Ayache. *Topological segmentation of discrete surfaces.* International Journal of Computer Vision, vol. 10, no. 2, pages 183–197, 1993. (Cited on page 28.)

[Malandain 2006] Grégoire Malandain. *Les mesures de similarité pour le recalage des images médicales.* PhD thesis, 2006. (Cited on page 29.)

[Massaro 2013] A. N. Massaro, M Bouyssi-Kobar, T Chang, L G Vezina, A J du Plessis and C Limperopoulos. *Brain Perfusion in Encephalopathic Newborns after Therapeutic Hypothermia.* American Journal of Neuroradiology, vol. 34, no. 8, pages 1649–1655, aug 2013. (Cited on page 74.)

[Matsumae 1996] Mitsunori Matsumae, Ron Kikinis, István A. Mórocz, Antonio V. Lorenzo, Tamás Sándor, Marilyn S. Albert, Peter McL. Black and Ferenc A. Jolesz. *Age-related changes in intracranial compartment volumes in normal adults assessed by magnetic resonance imaging.* Journal of Neurosurgery, vol. 84, no. 6, pages 982–991, 1996. (Cited on page 52.)

[Mazziotta 2001] J. Mazziotta, A. Toga, Alan C. Evans, P. Fox, J. Lancaster, K. Zilles, R. Woods, T. Paus, G. Simpson, B. Pike, C. Holmes, D. Louis Collins, Paul M. Thompson, D. MacDonald, M. Iacoboni, T. Schormann, K. Amunts, N. Palomero-Gallagher, S. Geyer, L. Parsons, K. Narr, N. Kabani, G. L. Goualher, D. Boomsma, T. Cannon, R. Kawashima and B. Mazoyer. *A probabilistic atlas and reference system for the human brain: International Consortium for Brain Mapping (ICBM).* Philosophical Transactions of the Royal Society B: Biological Sciences, vol. 356, no. 1412, pages 1293–1322, 2001. (Cited on page 41.)

[Miller 1993] Michael I. Miller, Gary E. Christensen, Yali Amit and Ulf Grenander. *Mathematical textbook of deformable neuroanatomies.* Proceedings of the National Academy of Sciences of the United States of America, vol. 90, no. 24, pages 11944–11948, 1993. (Cited on page 39.)

[Miller 2016] Karla L. Miller, Fidel Alfaro-Almagro, Neal K. Bangerter, David L. Thomas, Essa Yacoub, Junqian Xu, Andreas J. Bartsch, Saad Jbabdi, Stamatios N. Sotiropoulos,

Jesper L.R. Andersson, Ludovica Griffanti, Gwenaëlle Douaud, Thomas W. Okell, Peter Weale, Iulius Dragonu, Steve Garratt, Sarah Hudson, Rory Collins, Mark Jenkinson, Paul M. Matthews and Stephen M. Smith. *Multimodal population brain imaging in the UK Biobank prospective epidemiological study.* Nature Neuroscience, vol. 19, no. 11, pages 1523–1536, 2016. (Cited on page 97.)

[Miranda 2006] Maria J. Miranda, Kern Olofsson and Karam Sidaros. *Noninvasive measurements of regional cerebral perfusion in preterm and term neonates by magnetic resonance arterial spin labeling.* Pediatric Research, vol. 60, no. 3, pages 359–363, 2006. (Cited on page 80.)

[Mrazek 2006] P. Mrazek, J. Weickert and A. Bruhn. *On Robust Estimation and smoothing with Spatial and Tonal Kernels.* Geometric Properties for Incomplete data, no. 51, pages 335–352, 2006. (Cited on page 36.)

[Murphy 1996] D G Murphy, C DeCarli, A R McIntosh, E Daly, M J Mentis, P Pietrini, J Szczepanik, M B Schapiro, C L Grady, B Horwitz and S I Rapoport. *Sex differences in human brain morphometry and metabolism: an in vivo quantitative magnetic resonance imaging and positron emission tomography study on the effect of aging.* Archives of general psychiatry, vol. 53, no. 7, pages 585–94, 1996. (Cited on page 52.)

[Muzik 2000] Otto Muzik, Diane C. Chugani, Csaba Juhász, Chengang Shen and Harry T. Chugani. *Statistical parametric mapping: Assessment of application in children.* NeuroImage, vol. 12, no. 5, pages 538–549, 2000. (Cited on pages 73 and 115.)

[Nadaraya 1964] E. A. Nadaraya. *On Estimating Regression.* Theory of Probability & Its Applications, vol. 9, no. 1, pages 141–142, jan 1964. (Cited on page 46.)

[Nguyen The Tich 2011] Sylvie Nguyen The Tich, Peter J. Anderson, Rod W. Hunt, Katherine J. Lee, Lex W. Doyle and Terrie E. Inder. *Neurodevelopmental and perinatal correlates of simple brain metrics in very preterm infants.* Archives of Pediatrics and Adolescent Medicine, vol. 165, no. 3, pages 216–222, 2011. (Cited on page 52.)

[Noblet 2012] Vincent Noblet, Christian Heinrich, Fabrice Heitz and Jean Paul Armspach. *An efficient incremental strategy for constrained groupwise registration based on symmetric pairwise registration.* Pattern Recognition Letters, vol. 33, no. 3, pages 283–290, 2012. (Cited on page 98.)

[Novak 2009] Klaus Novak, Thomas Czech, Daniela Prayer, Wolfgang Dietrich, Wolfgang Serles, Stephan Lehr and Christoph Baumgartner. *Individual variations in the sulcal anatomy of the basal temporal lobe and its relevance for epilepsy surgery: an anatomical study performed using magnetic resonance imaging.* Journal of Neurosurgery, vol. 96, no. 3, pages 464–473, may 2009. (Cited on page 52.)

[Nyúl 1999] László G. Nyúl and Jayaram K. Udupa. *On standardizing the MR image intensity scale.* Magnetic Resonance in Medicine, vol. 42, no. 6, pages 1072–1081, 1999. (Cited on page 114.)

[Nyúl 2000] László G. Nyúl, J.K. Udupa and Xuan Zhang. *New variants of a method of MRI scale standardization.* IEEE Transactions on Medical Imaging, vol. 19, no. 2, pages 143–150, 2000. (Cited on page 114.)

[Oliveira 2014] Francisco P.M. Oliveira and João Manuel R.S. Tavares. *Medical image registration: a review.* Computer Methods in Biomechanics and Biomedical Engineering, vol. 17, no. 2, pages 73–93, jan 2014. (Cited on pages 29 and 34.)

[Ourselin 2000] S. Ourselin, Alexis Roche, Sylvain Prima and N. Ayache. *Block Matching: A General Framework to Improve Robustness of Rigid Registration of Medical Images.* In MICCAI, pages 557–566. Springer Berlin Heidelberg, 2000. (Cited on pages 30 and 31.)

[Pelizzari 1989] Charles A. Pelizzari, George T. Y. Chen, Danny R. Spelbring, Ralph R. Weichselbaum and Chin-Tu Chen. *Accurate Three-Dimensional Registration of CT, PET, and/or MR Images of the Brain.* Journal of Computer Assisted Tomography, vol. 13, no. 1, pages 20–26, jan 1989. (Cited on page 28.)

[Pennec 1996] Xavier Pennec. *L'incertitude dans les problèmes de reconnaissance et de recalage – Applications en imagerie médicale et biologie moléculaire.* PhD thesis, Ecole Polytechnique X, 1996. (Cited on pages 32, 33, 54 and 55.)

[Pennec 1999] Xavier Pennec, Pascal Cachier and Nicholas Ayache. *Understanding the "Demon's Algorithm": 3D Non-rigid Registration by Gradient Descent.* In MICCAI, pages 597–605. 1999. (Cited on page 37.)

[Pennec 2020] Xavier Pennec and Marco Lorenzi. *Beyond Riemannian geometry: The affine connection setting for transformation groups.* In Riemannian Geometric Statistics in Medical Image Analysis, chapter 5, pages 169–229. Elsevier, 2020. (Cited on page 20.)

[Peterson 2018] Mallory Peterson, Benjamin C Warf and Steven J Schiff. *Normative human brain volume growth.* Journal of Neurosurgery: Pediatrics, vol. 21, no. May, pages 1–8, 2018. (Cited on pages 52, 59 and 69.)

[Pfefferbaum 1994] Adolf Pfefferbaum, Daniel H. Mathalon, Edith V. Sullivan, Jody M. Rawles, Robert B. Zipursky and Kelvin O. Lim. *A Quantitative Magnetic Resonance Imaging Study of Changes in Brain Morphology From Infancy to Late Adulthood.* Archives of Neurology, vol. 51, no. 9, pages 874–887, sep 1994. (Cited on page 52.)

[Pienaar 2012] Rudolph Pienaar, Michael J. Paldino, Neel Madan, Kalpathy S. Krishnamoorthy, David C. Alsop, Mathieu Dehaes and P. Ellen Grant. *A quantitative method for correlating observations of decreased apparent diffusion coefficient with elevated cerebral blood perfusion in newborns presenting cerebral ischemic insults.* NeuroImage, vol. 63, no. 3, pages 1510–1518, 2012. (Cited on pages 74 and 80.)

[Pontabry 2013] Julien Pontabry. *Construction d'atlas en IRM de diffusion : application à l'étude de la maturation cérébrale.* PhD thesis, 2013. (Cited on pages 43 and 113.)

[Powell 2009] M J D Powell. *The BOBYQA algorithm for bound constrained optimization without derivatives.* Technical report, 2009. (Cited on page 30.)

[Prima 2002] Sylvain Prima, Sébastien Ourselin and Nicholas Ayache. *Computation of the mid-sagittal plane in 3-D brain images.* IEEE Transactions on Medical Imaging, vol. 21, no. 2, pages 122–138, 2002. (Cited on pages 57, 86 and 93.)

[Prima 2013] Sylvain Prima and Olivier Commowick. *Multimodal rigid-body registration of 3D brain images using bilateral symmetry.* Proceedings of SPIE, vol. 8669, page 866911, 2013. (Cited on pages 31 and 83.)

[Proisy 2016] Maïa Proisy, S. Mitra, C. Uria-Avellana, M. Sokolska, N. J. Robertson, F. Le Jeune and J. C. Ferré. *Brain perfusion imaging in neonates: An overview.* American Journal of Neuroradiology, vol. 37, no. 10, pages 1766–1773, 2016. (Cited on page 73.)

[Proisy 2019] Maïa Proisy, Isabelle Corouge, Antoine Legouhy, Amélie Nicolas, Valérie Charon, N. Mazille, Stéphanie Leroux, Bertrand Bruneau, Christian Barillot and Jean Christophe Ferré. *Changes in brain perfusion in successive arterial spin labeling MRI scans in*

neonates with hypoxic-ischemic encephalopathy. NeuroImage: Clinical, vol. 24, no. October 2018, page 101939, 2019. (Cited on pages 73 and 80.)

[Reiss 1996] A L Reiss, M T Abrams, H S Singer, J L Ross and M B Denckla. *Brain development, gender and IQ in children. A volumetric imaging study.* Brain : a journal of neurology, vol. 119 (Pt 5, pages 1763–74, 1996. (Cited on page 52.)

[Roche 1998] Alexis Roche, Grégoire Malandain, Xavier Pennec and Nicholas Ayache. *The correlation ratio as a new similarity measure for multimodal image registration.* Lecture Notes in Computer Science (including subseries Lecture Notes in Artificial Intelligence and Lecture Notes in Bioinformatics), vol. 1496, pages 1115–1124, 1998. (Cited on pages 28 and 31.)

[Roche 2000] Alexis Roche, Grégoire Malandain and Nicholas Ayache. *Unifying maximum likelihood approaches in medical image registration.* International Journal of Imaging Systems and Technology, vol. 11, no. 1, pages 71–80, 2000. (Cited on page 28.)

[Rodrigues 1840] Olinde Rodrigues. *Des lois géométriques qui régissent les déplacements d'un système solide dans l'espace, et de la variation des coordonnées provenant de ces déplacements considérés indépendamment des causes qui peuvent les produire.* Journal de mathématiques pures et appliquées, vol. 5, pages 380–440, 1840. (Cited on page 16.)

[Rohlfing 2009] Torsten Rohlfing, Natalie M Zahr, Edith V Sullivan and Adolf Pfefferbaum. *The SRI24 multichannel atlas of normal adult human brain structure.* Human Brain Mapping, vol. 31, no. 5, pages 798–819, dec 2009. (Cited on pages 45, 90 and 115.)

[Rohlfing 2012] Torsten Rohlfing. *Image similarity and tissue overlaps as surrogates for image registration accuracy: Widely used but unreliable.* IEEE Transactions on Medical Imaging, vol. 31, no. 2, pages 153–163, 2012. (Cited on page 29.)

[Rueckert 1999] Daniel Rueckert, L.I. Sonoda, C. Hayes, D.L.G. Hill, M.O. Leach and D.J. Hawkes. *Nonrigid registration using free-form deformations: application to breast MR images.* IEEE Transactions on Medical Imaging, vol. 18, no. 8, pages 712–721, 1999. (Cited on page 35.)

[Rueckert 2006] Daniel Rueckert, Paul Aljabar, Rolf A Heckemann, Jo V. Hajnal and Alexander Hammers. *Diffeomorphic Registration Using B-Splines.* In MICCAI - Medical Image Computing and Computer Assisted Intervention, number February, pages 702–709. 2006. (Cited on page 36.)

[Ruprecht 1995] Detlef Ruprecht, Ralf Nagel and Heinrich Müller. *Spatial free-form deformation with scattered data interpolation methods.* Computers & Graphics, vol. 19, no. 1, pages 63–71, jan 1995. (Cited on page 35.)

[Saliba 2010] E. Saliba and T. Debillon. *Neuroprotection par hypothermie contrôlée dans l'encéphalopathie hypoxique-ischémique du nouveau-né à terme.* Archives de Pediatrie, vol. 17, no. SUPPL. 3, pages S67–S77, 2010. (Cited on page 74.)

[Schnabel 2001] Julia A. Schnabel, Daniel Rueckert, Marcel Quist, Jane M. Blackall, Andy D. Castellano-Smith, Thomas Hartkens, Graeme P. Penney, Walter A. Hall, Haiying Liu, Charles L. Truwit, Frans A. Gerritsen, Derek L.G. Hill and David J. Hawkes. *A generic framework for non-rigid registration based on non-uniform multi-level free-form deformations.* Lecture Notes in Computer Science (including subseries Lecture Notes in Artificial Intelligence and Lecture Notes in Bioinformatics), vol. 2208, pages 573–581, 2001. (Cited on page 35.)

[Schuh 2015] Andreas Schuh, Maria Murgasova, Antonios Makropoulos, Christian Ledig, Serena J. Counsell, Jo V. Hajnal, Paul Aljabar and Daniel Rueckert. *Construction of a 4D Brain Atlas and Growth Model Using Diffeomorphic Registration.* In STIA, pages 27–37. 2015. (Cited on page 47.)

[Seber 1989] G. A. F. Seber and C. J. Wild. Nonlinear Regression. Wiley Series in Probability and Statistics. John Wiley & Sons, Inc., Hoboken, NJ, USA, feb 1989. (Cited on page 59.)

[Seghers 2004] Dieter Seghers, Emiliano D'Agostino, Frederik Maes, Dirk Vandermeulen and Paul Suetens. *Construction of a Brain Template from MR Images Using State-of-the-Art Registration and Segmentation Techniques.* In MICCAI, volume 9, pages 696–703, 2004. (Cited on page 44.)

[Serag 2012a] Ahmed Serag, Paul Aljabar, Gareth Ball, Serena J. Counsell, James P. Boardman, Mary A. Rutherford, A. David Edwards, Jo V. Hajnal and Daniel Rueckert. *Construction of a consistent high-definition spatio-temporal atlas of the developing brain using adaptive kernel regression.* NeuroImage, vol. 59, no. 3, pages 2255–2265, 2012. (Cited on pages 44, 46, 90, 91 and 142.)

[Serag 2012b] Ahmed Serag, A. David Edwards, Jo V. Hajnal, S J Counsell, J P Boardman and Daniel Rueckert. *A multi-channel 4D probabilistic atlas of the developing brain: application to fetuses and neonates.* Annals of the British ..., vol. 2012, no. 3, pages 1–14, 2012. (Cited on page 142.)

[Somerville 2018] Leah H. Somerville, Susan Y. Bookheimer, Randy L. Buckner, Gregory C. Burgess, Sandra W. Curtiss, Mirella Dapretto, Jennifer Stine Elam, Michael S. Gaffrey, Michael P. Harms, Cynthia Hodge, Sridhar Kandala, Erik K. Kastman, Thomas E. Nichols, Bradley L. Schlaggar, Stephen M. Smith, Kathleen M. Thomas, Essa Yacoub, David C. Van Essen and Deanna M. Barch. *The Lifespan Human Connectome Project in Development: A large-scale study of brain connectivity development in 5-21 year olds.* NeuroImage, vol. 183, no. July, pages 456–468, 2018. (Cited on page 113.)

[Sotiras 2013] Aristeidis Sotiras, Christos Davatzikos and Nikos Paragios. *Deformable medical image registration: A survey.* IEEE Transactions on Medical Imaging, vol. 32, no. 7, pages 1153–1190, 2013. (Cited on page 34.)

[Spiess 2010] Andrej Nikolai Spiess and Natalie Neumeyer. *An evaluation of R2 as an inadequate measure for nonlinear models in pharmacological and biochemical research: A Monte Carlo approach.* BMC Pharmacology, vol. 10, pages 1–11, 2010. (Cited on page 59.)

[Talairach 1988] J Talairach and P Tournoux. Co-Planar Stereotactic Atlas of the Human Brain. 1988. (Cited on page 39.)

[Thirion 1996] Jean-Philippe Thirion. *New feature points based on geometric invariants for 3D image registration.* International Journal of Computer Vision, vol. 18, no. 2, pages 121–137, may 1996. (Cited on page 28.)

[Thirion 1998] Jean-philippe Thirion. *Image matching as a diffusion process : an analogy with Maxwell ' s demons.* Medical Image Analysis, vol. 2, no. 3, pages 243–260, 1998. (Cited on page 37.)

[Thompson 2010] Paul Thompson, Michael Mega, Katherine Narr, Elizabeth Sowell, Rebecca Blanton and Arthur Toga. *Brain Image Analysis and Atlas Construction.* In Handbook of Medical Imaging, Volume 2. Medical Image Processing and Analysis, pages 1061–1129. SPIE, 1000 20th Street, Bellingham, WA 98227-0010 USA, 2010. (Cited on page 42.)

[Tosun 2015] Duygu Tosun, Prabha Siddarth, Jennifer Levitt and Rochelle Caplan. *Cortical thickness and sulcal depth: insights on development and psychopathology in paediatric epilepsy.* BJPsych Open, 2015. (Cited on page 52.)

[Umeyama 1991] Shinji Umeyama. *Least-Squares Estimation of Transformation Parameters Between Two Point Patterns.* IEEE Transactions on Pattern Analysis and Machine Intelligence, vol. 13, no. 4, pages 376–380, 1991. (Cited on page 33.)

[Utsunomiya 1999] Hidetsuna Utsunomiya, Koichi Takano, Masatoshi Okazaki and Akihisa Mitsudome. *Development of the temporal lobe in infants and children: Analysis by MR-based volumetry.* American Journal of Neuroradiology, vol. 20, no. 4, pages 717–723, 1999. (Cited on page 52.)

[Van Essen 2012] D. C. Van Essen, K. Ugurbil, E. Auerbach, D. Barch, T. E.J. Behrens, R. Bucholz, A. Chang, L. Chen, M. Corbetta, S. W. Curtiss, S. Della Penna, D. Feinberg, M. F. Glasser, N. Harel, A. C. Heath, L. Larson-Prior, D. Marcus, G. Michalareas, S. Moeller, R. Oostenveld, S. E. Petersen, F. Prior, B. L. Schlaggar, S. M. Smith, A. Z. Snyder, J. Xu and E. Yacoub. *The Human Connectome Project: A data acquisition perspective.* NeuroImage, vol. 62, no. 4, pages 2222–2231, 2012. (Cited on pages 97, 100 and 142.)

[Varela 2015] Marta Varela, Esben T. Petersen, Xavier Golay and Joseph V. Hajnal. *Cerebral blood flow measurements in infants using look-locker arterial spin labeling.* Journal of Magnetic Resonance Imaging, vol. 41, no. 6, pages 1591–1600, 2015. (Cited on page 74.)

[Vercauteren 2007] Tom Vercauteren, Xavier Pennec, Aymeric Perchant and Nicholas Ayache. *Non-parametric Diffeomorphic Image Registration with the Demons Algorithm.* In Medical Image Computing and Computer Assisted Intervention, pages 319–326. Springer Berlin Heidelberg, Berlin, Heidelberg, 2007. (Cited on pages 37 and 38.)

[Vercauteren 2008] Tom Vercauteren, Xavier Pennec, Aymeric Perchant and Nicholas Ayache. *Symmetric Log-Domain Diffeomorphic Registration: A Demons-Based Approach.* In Medical Image Computing and Computer Assisted Intervention, pages 754–761. Springer Berlin Heidelberg, 2008. (Cited on pages 20, 25, 37 and 38.)

[Vercauteren 2009] Tom Vercauteren, Xavier Pennec, Aymeric Perchant and Nicholas Ayache. *Diffeomorphic demons: efficient non-parametric image registration.* NeuroImage, vol. 45, no. 1 Suppl, 2009. (Cited on pages 37 and 38.)

[Vercauteren 2010] Tom Vercauteren. *Demons: A Deformable Registration Toolbox.* MICCAI 2010 Tutorial - Intensity-based Deformable Registration, 2010. (Cited on page 38.)

[Viergever 2016] Max A. Viergever, J.B. Antoine Maintz, Stefan Klein, Keelin Murphy, Marius Staring and Josien P.W. Pluim. *A survey of medical image registration - under review.* Medical Image Analysis, vol. 33, pages 140–144, oct 2016. (Cited on page 29.)

[Wagenmakers 2004] Eric-Jan Wagenmakers and Simon Ferrel. *AIC model selection using Akaike weights.* Psychonomic Bulletin & Review, vol. 11, no. 1, pages 192–196, 2004. (Cited on page 60.)

[Wells 1996] W.M. Wells, P. Viola, H. Atsumi, S. Nakajima and R. Kikinis. *Multi-Modal Volume Registration by Maximisation of Mutual Information.* Medical Image Analysis, 1996. (Cited on pages 28 and 31.)

[Wendland 1995] Holger Wendland. *Piecewise polynomial, positive definite and compactly supported radial functions of minimal degree.* Advances in Computational Mathematics, vol. 4, no. 1, pages 389–396, dec 1995. (Cited on page 35.)

[Whitcher 2007] Brandon Whitcher, Jonathan J. Wisco, Nouchine Hadjikhani and David S. Tuch. *Statistical group comparison of diffusion tensors via multivariate hypothesis testing.* Magnetic Resonance in Medicine, vol. 57, no. 6, pages 1065–1074, 2007. (Cited on pages 4, 7, 39 and 97.)

[Winkler 2012] Anderson M. Winkler, Mert R. Sabuncu, B. T.Thomas Yeo, Bruce Fischl, Douglas N. Greve, Peter Kochunov, Thomas E. Nichols, John Blangero and David C. Glahn. *Measuring and comparing brain cortical surface area and other areal quantities.* NeuroImage, vol. 61, no. 4, pages 1428–1443, 2012. (Cited on page 52.)

[Wintermark 2011] Pia Wintermark, A. Hansen, M. C. Gregas, J. Soul, M. Labrecque, R. L. Robertson and S. K. Warfield. *Brain perfusion in asphyxiated newborns treated with therapeutic hypothermia.* American Journal of Neuroradiology, vol. 32, no. 11, pages 2023–2029, 2011. (Cited on pages 74 and 80.)

[Wong 1998] Eric C. Wong, Richard B. Buxton and Lawrence R. Frank. *Quantitative imaging of perfusion using a single subtraction (QUIPSS and QUIPSS II).* Magnetic Resonance in Medicine, vol. 39, no. 5, pages 702–708, 1998. (Cited on page 77.)

[Wu 2012] Guorong Wu, Hongjun Jia, Qian Wang, Feng Shi, Pew-Thian Yap and Dinggang Shen. *Emergence of Groupwise Registration in MR Brain Study.* In Biosignal Processing: Principles and Practices. 2012. (Cited on page 43.)

[Yang 2011] Xuan Yang, Zhong Xue, Xia Liu and Darong Xiong. *Topology preservation evaluation of compact-support radial basis functions for image registration.* Pattern Recognition Letters, vol. 32, no. 8, pages 1162–1177, 2011. (Cited on page 34.)

[Zagorchev 2006] Lyubomir Zagorchev and Ardeshir Goshtasby. *A comparative study of transformation functions for nonrigid image registration.* IEEE Transactions on Image Processing, vol. 15, no. 3, pages 529–538, 2006. (Cited on page 34.)

[Zhang 2008] Zhixiong Zhang and Xuan Yang. *Elastic image warping using a new radial basic function with compact support.* BIOSIGNALS 2008 - Proceedings of the 1st International Conference on Bio-inspired Systems and Signal Processing, vol. 1, pages 216–219, 2008. (Cited on page 35.)

Software

[Anima] **Anima:** Open source software for medical image processing from the Empenn team. https://github.com/Inria-Visages/Anima-Public - RRID:SCR_017017

[Anima-Scripts] **Anima-Scripts:** Open source scripts using Anima software for medical image processing from the Empenn team.
https://github.com/Inria-Visages/Anima-Scripts-Public - RRID:SCR_017072

[medInria] **medInria:** Free and open-source ulti-platform medical image processing and visualization software. Cutting-edge processing functionalities for your medical images such as 2D/3D/4D image visualization, image registration, diffusion MR processing and tractography. https://med.inria.fr/

MRI ressources

[aslpedia] **ASLpedia:** A retrospective ASL study on routine pediatric MRI performed at Rennes University Hospital Neuropediatric radiology Department. Unfortunately not available for sharing.

[C-MIND] **C-MIND:** Data Repository created by the C-MIND study of Normal Brain Development. This is a multisite, longitudinal study of typically developing children from ages newborn through young adulthood conducted by Cincinnati Children's Hospital Medical Center and UCLA and supported by the National Institute of Child Health and Human Development (Contract HHSN275200900018C). A listing of the participating sites and a complete listing of the study investigators can be found at: https://research.cchmc.org/c-mind.

[dHCP] **The Developing Human Connectome Project (dHCP):** Led by King's College London, Imperial College London and Oxford University, aims to make major scientific progress by creating the first 4-dimensional connectome of early life.
https://data.developingconnectome.org/

[HCP] **The Human Connectome Project (HCP):** See [Van Essen 2012] for more details. The National Institutes of Health Blueprint for Neuroscience Research is launching a 30 million project that will use cutting-edge brain imaging technologies to map the circuitry of the healthy adult human brain. By systematically collecting brain imaging data from hundreds of subjects, the Human Connectome Project (HCP) will yield insight into how brain connections underlie brain function, and will open up new lines of inquiry for human neuroscience
http://www.humanconnectomeproject.org/

[ALBERTs] **ALBERTs:** See [Gousias 2012] and [Gousias 2013] for details about segmentations. Copyright Imperial College of Science, Technology and Medicine and Ioannis S. Gousias 2013. All rights reserved. https://brain-development.org/brain-atlases/neonatal-brain-atlases/neonatal-brain-atlas-gousias/

[Serag atlas] **Serag's Neonatal Brain Atlas:** See [Serag 2012a] and [Serag 2012b] for more details. Imperial College London. https://brain-development.org/brain-atlases/neonatal-brain-atlases/neonatal-brain-atlas-serag/

List of Figures

List of Tables

DOCTORAT BRETAGNE LOIRE / MATHSTIC

UNIVERSITÉ DE RENNES 1

Titre : Méthodes pour la modélisation morphologique longitudinale du cerveau via le recalage et la création d'atlas

Mot clés : Atlas, Recalage, Développement cérébral, Morphométrie, IRM

Résumé : Comprendre le développement du cerveau implique d'étudier la relation entre l'âge comme l'une des variables explicatives et des variables expliquées, les observations de cet organe, qui peuvent prendre de nombreuses formes. L'imagerie par résonance magnétique (IRM) permet d'extraire ces observations de manière non invasive et non irradiante. Cette technique puissante permet notamment d'obtenir des informations sur l'activité fonctionnelle du cerveau ou sur ses caractéristiques de diffusivité interne. Pourtant, c'est plutôt sur les aspects purement morphologiques que porte cette thèse. L'approche suivie est celle de l'étude du cerveau en tant qu'objet mathématique, permettant ainsi l'analyse de sa forme et de sa croissance au moyen des transformations géométriques reliant ces objets. Dans la découverte de ces transformations, à travers des structures topologiquement intéressantes, repose le concept de **recalage**. Cela ouvre la porte à l'analyse statistique des formes et à la création de modèles anatomiques moyens appelés **atlas**

Title: Methods for morphological longitudinal brain modeling through atlasing and registration

Keywords: Atlasing, Registration, Brain development, Morphometry, MRI

Abstract: Understanding brain development involves studying the relationship between age as one of the explanatory variables and explained variables, observations of this organ, which can take many forms. Magnetic Resonance Imaging (MRI) gives the opportunity to extract such observations in a non-invasive and non-irradiating way. This powerful technique allows notably to gain insights about the functional activity of the brain or its internal diffusivity characteristics. Yet, it is rather on the purely morphological aspects that this thesis is focused on. The approach followed the study of the brain as a mathematical object, thus enabling the analysis of its shape and growth by the means of the geometric transformations connecting those objects. In the finding of those transformations, across structures of topological interest, lies the concept of **registration**. This opens the door to the statistical analysis of shapes and the creation of average anatomical models called **atlases**.